



UNIVERSITÀ
DEGLI STUDI
FIRENZE

**Scuola di Scienze Matematiche
Fisiche e Naturali**
**Corso di Laurea Magistrale
in Scienze Fisiche e Astrofisiche**

Towards dipolar quantum gases in a ring

Verso gas quantistici dipolari in un anello

Candidato

Niccolò Preti

Relatore

Prof. Giovanni Modugno

Anno Accademico 2021/2022

Contents

Introduction	iii
1 Theory	1
1.1 Theoretical framework for superfluids	1
1.1.1 Thomas Fermi limit	3
1.1.2 Solitons	5
1.2 Dipolar gases	6
1.2.1 Harmonic confinement of dipolar condensate	9
1.2.2 Elementary excitations of a uniform dipolar gas	10
1.3 Superfluidity	12
1.3.1 Landau criterion for superfluidity	13
1.3.2 Two fluid theory	15
1.3.3 Vortices	16
1.3.4 Superfluids under rotation	18
1.4 Supersolids under rotation	19
1.4.1 Introduction	19
1.4.2 Leggett's theory on the rotation of supersolids	20
1.5 Dynamical Polarizability	25
1.6 Imaginary time evolution	30
2 Creation of arbitrary potential patterns using a DMD	33
2.1 The Digital Micromirror Device	33
2.2 Optical Setup to study the DMD	37
2.2.1 First optical setup	37
2.2.2 Second optical setup	39
2.3 Feedback procedure	40
2.4 Simulations	44
3 Characterization of a blue light source for optical trapping of dysprosium atoms	47
3.1 Repulsive light implemented in the experiment	48
3.2 Realizing and monitoring a single mode diode laser	49
3.3 Measurement of the Dy's polarizability at around 404 nm	58
3.4 Injection locking of a diode laser	68
3.5 Calibration of the imaging magnification	71

Conclusions	75
Bibliography	77

Introduction

In the mid 90's the experimental realization of a Bose-Einstein condensate (BEC) in ultracold atoms opened the way to a series of ground-breaking discoveries [1, 2].

Among these discoveries, it was shown that quantum gases show superfluidity, which is the ability to flow without friction. The superfluid properties of quantum gases were first demonstrated for bosons, by studying the hydrodynamic flow of the BEC when stirred by a laser [3], and by observing the formation of vortices [4]. The detection of superfluidity in fermionic gases was also enabled by observing vortices [5].

The first experimental evidence of superfluidity actually came much before the realization of quantum gases. In fact, in the late 30's it was discovered that liquid ^4He becomes superfluid under the temperature of 2.17 K [6, 7]. Since both the gaseous and liquid phases were shown to have a quantum counterpart with superfluid properties, the scientific world started to think if this could be true also for the solid phase. The first theoretical discussion on supersolidity was made by Gross in 1957 [8], who thought of the idea of having a bosonic ground state that showed a spatial density modulation. In 1970, a paper by Leggett showed that the supersolid should be characterized by a lower moment of inertia with respect to a classical system, similarly to what happens with regular superfluids [9]. In 1969 Andreev and Lifschitz [10], and in 1970 Chester [11], proposed a physical mechanism to explain the presence of supersolid order in a quantum crystal. Their idea was that at sufficiently low temperatures localized defects become excitations that can move freely through the crystal. These so called "Defectons" obey Bose statistics and can thus condense, resulting in a superfluid flow in a crystalline background. Defectons were predicted to exist in crystals with very large zero-point oscillations, such as solid helium. Because of this the search for supersolidity started again with ^4He , this time solid. For more than 30 years no real evidence of helium's supersolidity was found, until in 2004 Kim and Chan published two papers [12, 13] on the probable observation of a supersolid phase in solid ^4He , made through the study of its non classical rotational inertia, as proposed by Leggett. They were able to observe a sudden drop in the oscillation period of a torsional oscillator filled with helium, when helium becomes solid. These results sparked great interest and discussions and a lot of effort was put into trying to interpret their experimental results [14]. In 2012, Kim and Chan were able to demonstrate that the reduction of the moment of inertia they saw in 2004 in solid helium was not a byproduct of the onset of supersolidity, but it was due to a change of the elastic properties of the solid [15].

In later years the concept of supersolidity was generalized from quantum crystals such as solid helium to other types of system that show superfluidity, like Bose-Einstein con-

densates. The coexistence of phase coherence, typical of superfluids, and of solid-like density modulations has been reported for example in BECs inside optical cavities. The modulation of such a system is, however, infinitely stiff since it is externally imposed, and because of this such system cannot be regarded as a true supersolid [16].

Another route to supersolidity was given by dipolar quantum gases, that can have both short range Van der Waals interactions and long ranged anisotropic magnetic interactions. A peculiar feature of dipolar gases is given by their excitation spectrum, that shows a local minimum at finite momentum, also called “Roton”. This same phenomenon was studied much earlier in liquid helium [17]. In dipolar gases the rotonic minimum can be tuned by changing the relative importance of contact and dipolar interactions via Feshbach resonances. When the roton crosses the zero value for the energy it becomes energetically favorable for the dipolar system to have a macroscopic occupation of the roton’s momentum state, thus inducing an instability in the system that can lead to the formation of an array of quantum droplets. This instability can then be stabilized by quantum fluctuations. The density modulation formed in this way is a direct consequence of the particle’s interaction properties and is not externally imposed on the system. Thanks to this technique the supersolid phase was finally observed in 2019 in a dipolar gas of dysprosium in the group lead by Giovanni Modugno in Pisa [18] and later the same year the supersolid was also observed in Innsbruck [19] and in Stuttgart [20].

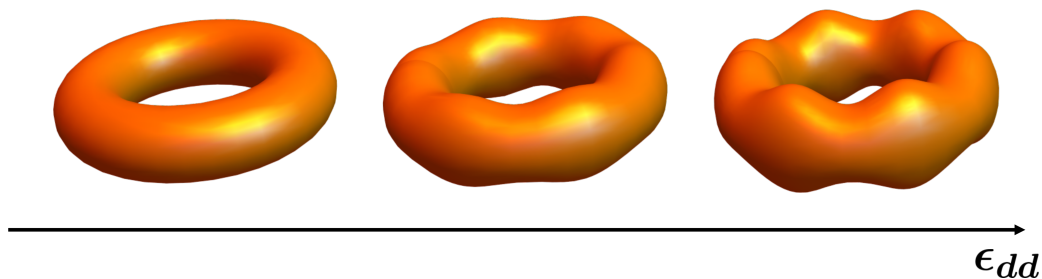
Supersolidity in dipolar gases is the result of two spontaneously broken symmetries. The first one is the $U(1)$ phase invariance leading to superfluidity, while the second one is the translational symmetry that gives rise to the density modulation in the system. Both of these symmetry breaking give rise to a different Goldstone mode [21]. After its discovery, Modugno’s group studied the non classical rotational inertia of the supersolid, showing a reduction of moment of inertia with respect to a classical system when excited in the scissors mode [22]. In this work the group also linked the moment of inertia to the Leggett’s superfluid fraction f_s of the system, wanting to show that $f_s = 1$ when the system is fully superfluid whereas $f_s < 1$ when the system undergoes the supersolid phase transition. The comparison between the experimental results for the superfluid fraction and the Leggett’s bound is rather tricky in this setup because there are actually two kind of mechanism at play in giving the experimental value of the moment of inertia of the system. A mass transport through the supersolid weak link that is a Leggett type contribution, but also another contribution to the moment of inertia comes from the single droplets oscillation. In the experiment the group was only able to get a value of superfluid fraction compatible to 1, and not lower, in the supersolid regime. A setup better suited to compare the experiment with theory would be one in which the atoms are trapped inside a ring shaped potential, as originally proposed by Leggett, because in this case the contribution of the individual droplets to the superfluid fraction would be reduced.

In the last two decades there’s been a lot of progress towards the trapping of BECs inside rings. These rings can be made either with fully magnetic potentials [23, 24], a combination of magnetic and optical potentials [25, 26] or fully optical [27, 28, 29, 30, 31]. Regarding optical rings, they can be realized employing Laguerre-Gaussian (LG) beams [27, 30], time averaged painted potentials [32, 33], or through the use of a spatial light modulator [34]. Once the superfluid is loaded inside the ring, angular momentum can be imprinted on it

by Raman coupling with LG beams [25, 27, 29, 30], stirring with an off resonance laser [33], temperature quenches [35], phase imprinting [34, 36], or even making the BEC itself move in a spiral trajectory around a blue stationary laser beam [37].

This thesis reports the work I made in the dysprosium lab that I joined in October 2022 towards the trapping of a degenerate gas in a ring potential.

Once we will have the superfluid trapped in the ring, we will be able to analyze a plethora of different phenomena, from the creation of solitons to the study of persistent currents in dipolar BECs, even seeing what happens crossing the superfluid to supersolid quantum phase transition. Regarding the supersolid, achieving one trapped in a ring will allow us to study its rotation properties and, consequently, its superfluid fraction, in a setting much closer to the one envisioned by Leggett's theory.



Sketch of the superfluid to supersolid phase transition inside a ring potential.

The thesis is organized as follows.

In the first chapter I lay the theoretical foundations of my thesis. I briefly introduce the concepts of second quantization and the Gross-Pitaevskii equation that are needed to describe degenerate quantum gases. In this context I also introduce some famous classes of solutions for the Gross-Pitaevskii equation like solitons and vortices, that are excited states of the condensate in the ring that we will be able to study once this potential will be on the atoms. These excitations are extremely interesting to study in our system since dysprosium is highly magnetic. Because of this we will be able to observe if the dipolar interaction in our system changes in any way the features of such states. It will be especially interesting to study vortices, but more in general, rotations, through the superfluid-supersolid quantum phase transition. Because of this I also introduce in this chapter Leggett's theory on rotations in a ring and a general section on dipolar gases, their excitation spectrum and how the phenomenon of supersolidity takes place. A key quantity relating the intensity of a laser to the force that this laser can imprint on atoms is called polarizability. This quantity measures the strength of the atom-light interaction and its knowledge is of utmost importance when one wants to know what kind of potentials a certain laser will be able to produce. Most of my theses work has been concentrated on finding the polarizability of dysprosium around 404 nm, that is the working wavelength of the laser we want to employ to create the repulsive ring potential. This quantity is still not known in the literature. Because of this the last part of the first chapter is dedicated

to the theoretical treatment of polarizability.

In the second chapter I describe the work I made to characterize the digital micromirror device (DMD) that we will employ as a spatial light modulator to create tailored optical potentials for our quantum gas, such as the ring potential and the phase gradient we will use to imprint angular momentum to the BEC. In this chapter I will explain the critical difficulties one encounters when trying to realize uniform potentials for bosons, and the solutions I employed to get around these problems. In the last part of this chapter I show some simulations for the ground state of the Gross-Pitaevskii equation. These simulations are made for the condensate trapped in a ring potential whose shape is the experimentally achieved one, while the potential height is fixed in the simulations to be 200 nK. Again, this number in reality will depend on the laser power and on the atom's polarizability.

In the third and final chapter I will explain the work that has been done to characterize the source of light we will employ with the DMD to make our repulsive annular potential. This source is represented by a blue diode laser working around 404 nanometers. This wavelength has been chosen for two main reasons. The first one is because it produces a repulsive potential for dysprosium. The second one is given by the fact that, because the resolution of all lenses has a lower bound given by diffraction that scales linearly with the wavelength, working with such a small wavelength will allow us to have the best possible resolution when projecting our ring potential on the atoms. This resolution is expected to be around 1.5 μm . This is extremely important in our case because, differently to what happens in fermionic systems, our degenerate gas is extremely small and the ring radius we are projecting to use to trap the atoms will be around 5 μm , with a thickness of about 2 μm that will be just bigger than the optical system's resolution. This laser we are going to use has, out of the box, a broad spectrum, and it so happens that some of its spectrum crosses a dysprosium's strong absorption transition. Because of this we cannot use the laser as is and a lot of effort has been put into reducing its emission spectrum.

Working close to resonance however has the advantage that the dynamical polarizability of dysprosium should be extremely high. In the third chapter is also reported our experimental measurements of this dynamical polarizability.

Chapter Theory 1

In this chapter I establish the theoretical background of my thesis. Firstly I introduce the concepts of second quantization and the most famous Gross-Pitaevskii equation, that are needed to describe degenerate weakly interacting quantum gases. Thanks to the Gross-Pitaevskii equation it's possible to study a plethora of excitations for the condensate. Of these, particular interest in the case of ringed condensates is devoted to solitons and vortices. The former is considered in the first section while the latter is introduced in the more general context of superfluidity, to which the third section of this chapter is devoted. In the second section I briefly describe some general concepts regarding dipolar condensates like their excitation spectrum. This topic is of fundamental importance for our work since it explains how tuning the contact interactions can lead to a second breaking of symmetry in the system and bring forth supersolidity.

In the third section I will describe the general theory of superfluidity. Landau's theory of superfluidity is developed to introduce the concepts of normal and superfluid components inside a liquid. The superfluid fraction, that is, the ratio between superfluid density and the total one, is of utmost importance when dealing with superfluids and, more importantly, supersolids.

In section four I show what changes when one considers rotations in supersolids. In this regard, Leggett's theory on rotations is presented, where its famous upper bound on the superfluid fraction is derived.

In the fifth section I describe the theory regarding coherent atom-light interaction. This part relates to the the third chapter were the formulas derived here are used for comparison with our experimental results.

In the last section of this chapter I briefly describe the concept of imaginary time evolution, that is the framework used to make the simulations that will be showed in the second chapter.

1.1 Theoretical framework for superfluids

A quantum many-body system can be treated theoretically in what is called "Second quantization". In this framework we define the bosonic field operator $\Psi(\mathbf{r})$, that is the operator that creates a boson in position \mathbf{r} , such that $\Psi(\mathbf{r})|0\rangle = |\mathbf{r}\rangle$ where $|0\rangle$ represents the vacuum of particles. The bosonic field operators follow the classical commutation relation $[\Psi(\mathbf{r}), \Psi^\dagger(\mathbf{r}')] = \delta(\mathbf{r} - \mathbf{r}')$.

The hamiltonian for a system of N interacting bosons can be written in second quantization

as:

$$\begin{aligned} \mathcal{H} = & \int d\mathbf{r} \Psi^\dagger(\mathbf{r}, t) \left(-\frac{\hbar^2}{2m} \nabla^2 + V_{ext}(\mathbf{r}, t) \right) \Psi(\mathbf{r}, t) + \\ & + \frac{1}{2} \iint d\mathbf{r} d\mathbf{r}' \Psi^\dagger(\mathbf{r}, t) \Psi^\dagger(\mathbf{r}', t) V(\mathbf{r} - \mathbf{r}') \Psi(\mathbf{r}', t) \Psi(\mathbf{r}, t) \end{aligned} \quad (1.1)$$

where $V_{ext}(\mathbf{r})$ represents a trapping potential for the bosons and is generally taken to be harmonic, while $V(\mathbf{r} - \mathbf{r}')$ represents the interaction potential between two bosons.

Let's consider the field operator $\Psi(\mathbf{r}, t)$ at time t , that can be written in the Heisenberg representation as:

$$\Psi(\mathbf{r}, t) = e^{i\mathcal{H}t} \Psi(\mathbf{r}) e^{-i\mathcal{H}t}. \quad (1.2)$$

We can write the equation of motion for this field as:

$$i\hbar\partial_t \Psi(\mathbf{r}, t) = [\Psi(\mathbf{r}, t), \mathcal{H}]. \quad (1.3)$$

By evaluating explicitly this commutator we get the following equation of motion for Ψ :

$$i\hbar\partial_t \Psi(\mathbf{r}, t) = \left[-\frac{\hbar^2}{2m} \nabla^2 + V_{ext}(\mathbf{r}, t) + \int \Psi^\dagger(\mathbf{r}', t) V(\mathbf{r}' - \mathbf{r}) \Psi(\mathbf{r}', t) d\mathbf{r}' \right] \Psi(\mathbf{r}, t). \quad (1.4)$$

We can now introduce the Bogoliubov approximation for the field operator, that we write as a classical term describing the expectation value of Ψ on the ground state of the theory

$$\Psi(\mathbf{r}, t) = \langle \text{GS} | \Psi(\mathbf{r}, t) | \text{GS} \rangle \quad (1.5)$$

to which we add a quantum fluctuation term

$$\Psi(\mathbf{r}, t) = \Psi(\mathbf{r}, t) + \delta\Psi(\mathbf{r}, t) \quad (1.6)$$

where the quantum fluctuation term is supposed to be small with respect to the classical term

$$\int d\mathbf{r} \langle \delta\Psi^\dagger \delta\Psi \rangle \ll \int d\mathbf{r} \Psi^*(\mathbf{r}, t) \Psi(\mathbf{r}, t). \quad (1.7)$$

To first approximation we can then neglect the quantum fluctuation term and arrive to the famous Gross-Pitaevskii equation (GPE)

$$i\hbar\partial_t \Psi(\mathbf{r}, t) = \left(-\frac{\hbar^2}{2m} \nabla^2 + V_{ext}(\mathbf{r}, t) + V_{int}(\mathbf{r}) \right) \Psi(\mathbf{r}, t) \quad (1.8)$$

where

$$V_{int}(\mathbf{r}) = \int d\mathbf{r}' \Psi^*(\mathbf{r}') V(\mathbf{r} - \mathbf{r}') \Psi(\mathbf{r}') \quad (1.9)$$

and, if we consider only contact interactions, we have that $V = g\delta(\mathbf{r} - \mathbf{r}')$ where $g = 4\pi\hbar^2 a_s/m$ and a_s represents the s -wave scattering length. In this limit we have that $V_{int} = g|\Psi(\mathbf{r})|^2$.

By factorizing the time dependence of the order parameter in this way $\Psi(\mathbf{r}, t) = \Psi(\mathbf{r}) e^{-i\mu t/\hbar}$

where μ represents the chemical potential of the system, we can also write the stationary Gross-Pitaevskii equation

$$\left(-\frac{\hbar^2}{2m}\nabla^2 + V_{ext}(\mathbf{r}, t) + g|\Psi(\mathbf{r})|^2\right)\Psi(\mathbf{r}) = \mu\Psi(\mathbf{r}). \quad (1.10)$$

The function Ψ is called order parameter and, because of equation 1.7, is normalized to the total number of atoms

$$\int |\Psi|^2 d\mathbf{r} = N. \quad (1.11)$$

This implies that the total density of the system coincides with the density derived from the order parameter

$$n(\mathbf{r}) = |\Psi(\mathbf{r})|^2. \quad (1.12)$$

By writing the order parameter as

$$\Psi(\mathbf{r}, t) = \sqrt{n(\mathbf{r}, t)}e^{i\phi(\mathbf{r}, t)} \quad (1.13)$$

from the Gross-Pitaevskii equation its possible to derive two other equations that, when taken in combination, are exactly analogous to the GPE:

$$\begin{aligned} \partial_t n(\mathbf{r}, t) + \nabla \cdot \mathbf{j} &= 0 \\ m\partial_t \mathbf{v} + \nabla \left(\frac{1}{2}m\mathbf{v}^2 + V_{ext} + gn - \frac{\hbar^2}{2m\sqrt{n}}\nabla^2\sqrt{n} \right) &= 0 \end{aligned} \quad (1.14)$$

where we have defined the velocity $\mathbf{v} = \hbar\nabla\phi/m$ and the current density as $\mathbf{j} = n\mathbf{v}$. The fact that the velocity field can be expressed as a gradient brings forth the important consequence that \mathbf{v} is irrotational ($\nabla \times \mathbf{v} = 0$). We will see that this condition makes velocity fields inside superfluids that are completely different from standard liquids. The first equation in 1.14 represents the equation of continuity giving rise to the conservation of particles in the system, while the second can be seen as the equation governing the time evolution for the velocity field. The term proportional to $\nabla^2\sqrt{n}$ in this equation is called ‘‘Quantum pressure’’ and can be ignored if the typical length scale for density fluctuations is bigger than the healing length $\xi = \hbar/\sqrt{2mgn}$ of the condensate. If one neglects this term, the two equations 1.14 become analogous to the hydrodynamic equations describing a non-viscous liquid with an irrotational velocity field.

1.1.1 Thomas Fermi limit

In the presence of an harmonic trapping potential

$$V_{ext}(\mathbf{r}) = \frac{1}{2}m\omega_x^2x^2 + \frac{1}{2}m\omega_y^2y^2 + \frac{1}{2}m\omega_z^2z^2 \quad (1.15)$$

one needs to solve the GPE numerically, apart from some interesting limiting cases. The consequences of the interaction term inside the GPE are readily identifiable: If the interaction is repulsive ($g > 0$), then the gas will expand and the size of the atomic cloud

will grow with respect to the non interacting case. At a certain point, when the interactions' strength crosses some critical value, the cloud density will become so smooth that one is able to neglect the kinetic energy term inside the GPE. This limit where one neglects the kinetic energy is called Thomas-Fermi limit and is characterized by the analytical solution:

$$\Psi_{TF} = \sqrt{n_{TF}^0(\mathbf{r})} \quad (1.16)$$

where

$$n_{TF}^0(\mathbf{r}) = \begin{cases} [\mu_{TF}^0 - V_{ext}(\mathbf{r})]/g & \text{if } \mu_{TF}^0 > V_{ext}(\mathbf{r}) \\ 0 & \text{otherwise.} \end{cases} \quad (1.17)$$

The value of the chemical potential in this approximation is given by the normalization condition $N = \int d\mathbf{r} n_{TF}^0(\mathbf{r})$ and is thus given by

$$\mu_{TF}^0 = \frac{\hbar\omega_{ho}}{2} \left(\frac{15Na}{a_{ho}} \right)^{2/5} \quad (1.18)$$

where $a_{ho} = \sqrt{\hbar/m\omega_{ho}}$ and $\omega_{ho} = (\omega_x\omega_y\omega_z)^{1/3}$.

If we consider for simplicity a spherically symmetric harmonic trap with frequency ω_{ho} and we use a_{ho} and $\hbar\omega_{ho}$ as units of length and energy we can write the GPE in the following way

$$\left[-\tilde{\nabla}^2 + \tilde{r}^2 + 8\pi \frac{Na_s}{a_{ho}} \tilde{\Psi}^2(\tilde{\mathbf{r}}) \right] \tilde{\Psi}(\tilde{\mathbf{r}}) = 2\tilde{\mu}\tilde{\Psi}(\tilde{\mathbf{r}}) \quad (1.19)$$

where $\tilde{\Psi} = N^{-1}a_{ho}^{-3/2}\Psi_0$. In these units the order parameter satisfies the following normalization condition: $\int d\tilde{\mathbf{r}} |\tilde{\Psi}|^2 = 1$.

From the GPE written with these units it is evident that the strength of the interatomic potential is completely fixed by the combination Na_s/a_{ho} , that is called Thomas-Fermi parameter. The Thomas-Fermi approximation will be valid if the homonym parameter is much bigger than one:

$$N \frac{a_s}{a_{ho}} \gg 1. \quad (1.20)$$

Typical values of a_s/a_{ho} are on the order of 10^{-3} so that for systems containing more than 10^5 atoms the Thomas-Fermi condition is effectively verified.

In the Thomas-Fermi limit the density profile of a gas where only contact interactions are present is given by an inverted parabola. This parabola will reach 0 in the classical inversion points for the motion. The classical inversion points R_k , $k = x, y, z$ are fixed by the trapping frequencies of the external potential thanks to the following condition:

$$\mu_{TF}^0 = \frac{1}{2} m \omega_k^2 R_k^2 \quad (1.21)$$

and using the Thomas-Fermi expression for the chemical potential we get that

$$R_k = a_{ho} \left(\frac{15Na}{a_{ho}} \right)^{1/5} \frac{\omega_{ho}}{\omega_k} \quad (1.22)$$

1.1.2 Solitons

In this section we consider a special class of solutions for the GPE, called *solitons*. In the particular case of repulsive forces between the gas particles, these solutions correspond to localized modulation of the density, that can move in the gas at a constant speed in such a way that their intrinsic form is preserved in time. If the density profile in the perturbed region is characterized by a lesser value with respect to the bulk density, these solutions are called gray solitons. The existence of such gray solitons is directly related to the non linearity of the GPE. The typical length scale of these modulations is in fact fixed by the healing length.

Let's consider a one dimensional system, where the order parameter Ψ depends only on the z coordinate through the combination $z - vt$. By introducing the dimensionless variable $\zeta = (z - vt)/\xi$ we can write the order parameter in the following way

$$\Psi(z, t) = \Psi_0(z - vt)e^{-i\mu t/\hbar} = \sqrt{n}f(\zeta)e^{-i\mu t/\hbar}. \quad (1.23)$$

Inserting this ansatz in the GPE and defining $U = 2m\xi v/\hbar$ we get

$$2iU \frac{df}{d\zeta} = \frac{d^2f}{d\zeta^2} + f(1 - |f|^2). \quad (1.24)$$

Our goal is to find a localized solution for this equation. This requirement can be implemented thanks to the following boundary conditions

$$|f| \xrightarrow{\zeta \pm \infty} 1 \quad \frac{df}{d\zeta} \xrightarrow{\zeta \rightarrow \pm \infty} 0 \quad (1.25)$$

which imply that at long distances from the center of the modulation the density should come back to the unperturbed value, that is \sqrt{n} .

Solving the GPE with these boundary conditions we get the following solution

$$\Psi_0(z - vt) = \sqrt{n} \left(i \frac{v}{c} + \sqrt{1 - \frac{v^2}{c^2}} \tanh \left(\frac{z - vt}{\sqrt{2}\xi} \sqrt{1 - \frac{v^2}{c^2}} \right) \right) \quad (1.26)$$

where $c = \sqrt{gn/m}$ represents the speed of sound.

The density profile of the system can be obtained by squaring this quantity and thus takes the following form:

$$n(z - vt) = |\Psi_0|^2 = n + \delta n(z - vt) \quad (1.27)$$

where we have defined

$$\delta n(z - vt) = -n \left(1 - \frac{v^2}{c^2} \right) \cosh^{-2} \left(\frac{z - vt}{\sqrt{2}\xi} \sqrt{1 - \frac{v^2}{c^2}} \right). \quad (1.28)$$

From this we get that the density has a minimum in the center of the soliton where

$$n(0) = \frac{nv^2}{c^2} \quad (1.29)$$

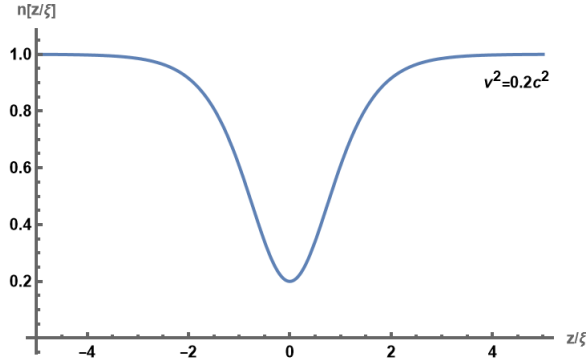


Figure 1.1: Normalized density profile for a grey soliton. The length scale of this soliton is proportional to the healing length and becomes bigger as the speed of the soliton tends to the sound velocity.

like is shown in figure 1.1. This value is then 0 for a soliton that propagates with 0 velocity, also called dark soliton. Its also important to notice that the size of the soliton is proportional to the healing length, but is amplified by a factor $(1 - v^2/c^2)^{1/2}$, that becomes bigger and bigger as $v \rightarrow c$.

1.2 Dipolar gases

The dipolar interaction is characterized by the following two-body interaction potential

$$V_{dd}(\mathbf{r}) = \frac{C_{dd}}{4\pi} \frac{\hat{e}_1 \cdot \hat{e}_2 r^2 - 3(\hat{e}_1 \cdot \mathbf{r})(\hat{e}_2 \cdot \mathbf{r})}{r^5} \quad (1.30)$$

where \hat{e}_1 and \hat{e}_2 represent the unit vectors that define the direction of the dipoles, while \mathbf{r} represents their relative distance. C_{dd} is instead a constant that depends on the specific type of dipolar interaction and defines the interaction's strength.

In what follows we will work with dipoles that have the same orientation in space, orientation that in the experiment will be fixed by an external magnetic field. In this way the dipolar potential assumes the following simplified expression:

$$V_{dd}(r, \theta) = \frac{C_{dd}}{4\pi} \frac{1 - 3 \cos^2(\theta)}{r^3} \quad (1.31)$$

where θ represents the angle formed by the 2 dipoles as can be seen from figure 1.2. By comparing the dipolar potential with the contact one

$$V = \frac{4\pi\hbar^2 a_s}{m} \delta(\mathbf{r}) \quad (1.32)$$

its immediate to find two fundamental differences. The long-range character of the dipolar interaction, and its anisotropy. Both these features contribute to new interesting physical properties in dipolar gases.

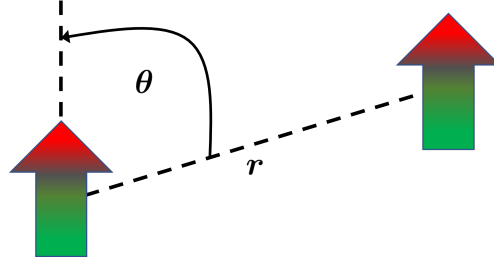


Figure 1.2: Definition of the angle θ and distance r between two dipoles used in equation 1.31. Image adapted from [38].

Long range nature of the force The $1/r^3$ law for the dipolar potential makes it long range when compared to the $1/r^6$ law exhibited by Van der Waals forces at long distance. For central potentials that scale as $1/r^p$, the phase shifts $\delta_\ell(k)$ that characterize the two body scattering properties behave, in three dimensions and for $k \rightarrow 0$, as $k^{2\ell+1}$ if $\ell < (p-3)/2$ and as k^{p-2} otherwise. From this it follows that for the van der Waals potential ($p = 6$) the scattering channel with $\ell = 0$ is the dominant one at low energy and that the full form of the potential can be replaced with an effective zero range one. The strength of this new effective potential will be completely determined by the s -wave scattering length.

Instead, in the case of dipolar interactions ($p = 3$), all partial waves will give a contribution to the scattering properties and this potential cannot be replaced with an effective one.

Anisotropy of the force Anisotropy is another fundamental feature of the dipolar interaction. Equation 1.31 shows that the sign of the potential depends on the angle θ . The dipolar force reaches 0 when $\theta = \theta_{cr} = \arccos(1/\sqrt{3}) \approx 54.7^\circ$, has a repulsive character when $\theta > \theta_{cr}$ and an attractive one in the opposite limit.

A peculiar feature of the potential that is related to this anisotropic character is given by its 3D Fourier transform

$$V_{dd}^{3D}(\mathbf{q}) = \int d\mathbf{r} e^{i\mathbf{q}\cdot\mathbf{r}} V_{dd}(\mathbf{r}) = C_{dd} \left(\cos^2(\alpha) - \frac{1}{3} \right) \quad (1.33)$$

that is seen to be completely independent from the modulus q , quite similarly to what happens to the contact interaction. However, $V_{dd}^{3D}(\mathbf{q})$ depends on the angle α that the wave vector \mathbf{q} forms with the dipole's polarization. This dependency gives rise to an anisotropy in the sound velocity inside dipolar superfluids. A kind of geometry that favours stability inside dipolar gases is the so called "Pancake geometry", where the dipoles are oriented in the direction orthogonal to the plane. In this regime, the repulsive nature of the force becomes dominant. In the strong axial confinement regime, we can use a Gaussian ansatz in the dipole's direction for the density $n(z) \propto \mathcal{G}(z)$ and use this function to average out the z direction from the dipolar potential. In this 2D limit the Fourier transform of the dipolar potential takes the form:

$$V_{dd}^{2D}(q) = \frac{2}{3} \frac{C_{dd}}{\sqrt{2\pi}a_z} \left[1 - F \left(\frac{qa_z}{\sqrt{2}} \right) \right] \quad (1.34)$$

Species	Dipole	a_{dd}
^{87}Rb	$1.0\mu_B$	0.037 nm
^{52}Cr	$6.0\mu_B$	0.80 nm
^{168}Er	$7.0\mu_B$	3.7 nm
^{164}Dy	$10\mu_B$	7 nm
^{40}K ^{87}Rb	0.57 D	0.21 μm
^{23}Na ^{40}K	2.72 D	2.3 μm

Table 1.1: Dipolar moments of different atomic and molecular species. Data taken from [39].

where $F(x) = (3\sqrt{3}/2)|x|e^{x^2}\text{erfc}(x)$ and $\text{erfc}(x)$ represents the complementary error function [38].

Dipolar forces of the form 1.30 can be obtained both with atoms that possess a permanent magnetic moment or with polar molecules that possess a permanent electric moment. In the first case one has

$$C_{dd} = \mu_0\mu_M^2 \quad \text{Magnetic atoms} \quad (1.35)$$

where μ_0 represents the magnetic permeability of free space and μ_M is the magnetic moment of the atom. In the case of electric interactions one instead has

$$C_{dd} = \langle d \rangle^2 / \epsilon_0 \quad \text{Polar molecules} \quad (1.36)$$

where $\langle d \rangle$ represents the average value of the electric dipole moment and ϵ_0 is the electric permittivity of free space. The value of C_{dd} thus depends strongly on the electric or magnetic nature of the dipolar interaction as well as on the atomic/molecular species under consideration. Some typical values of atomic and molecular values for C_{dd} are reported in table 1.1. Dipolar interactions can also be obtained with Rydberg atoms, that have a shorter lifetime but can still give rise to strong effects given their high value of polarizability.

Magnetic moments are on the order of the Bohr magneton μ_B , while electric moments of polar molecules are on the order of ea_0 , where a_0 represents the Bohr radius.¹ From this it follows that the ratio between the coupling constants C_{dd} evaluated for electric and magnetic cases scale as:

$$\frac{C_{dd}^{el}}{C_{dd}^{mag}} = \left(\frac{ea_0}{\epsilon_0\mu_0\mu_B} \right)^2 = \frac{4}{\alpha} \gg 1 \quad (1.37)$$

where $\alpha \approx 1/137$ represents the fine structure constant. Alkali atoms have a very small magnetic moment ($\mu_M \lesssim 1\mu_B$) and are thus not suited to investigate magnetic effects, even if the role of the dipolar interaction can still be seen by reducing the contact scattering length through Feshbach resonances. Most of the experiments on dipolar atoms work with atomic species like chromium, dysprosium and erbium, that possess high values of magnetic moment. Thanks to the long range nature of the dipolar interaction, it's even possible

¹Electric dipole moments are usually expressed in Debyes where $1 \text{ D} \approx 0.39ea_0$.

to cool down to degeneracy fermionic isotopes of Dy and Er by employing a standard evaporation scheme. This is because the elastic scattering between identical fermions is not suppressed at low energy, thanks to the dipolar interaction.

Regarding the electric interactions, heteronuclear polar molecules represent an interesting platform where to study dipolar physics, thanks to their high electric dipole moment. Experimental works on the cooling to degeneracy of these molecules are now directed towards a first cooling stage of two different atomic species that are then associated in weakly bound molecular states called Feshbach molecules. These weakly bound states are then brought to the absolute ground state of the molecule thanks to a two photon adiabatic Raman process. This kind of experiments are extremely complicated because of the tendency of the molecules to decay given their high chemical activity (For example, two K-Rb molecules will tend to decay towards K-K+Rb-Rb states).

Another useful quantity describing the strength of the dipolar interaction is given by the so called effective dipolar range, that is given by

$$a_{dd} = \frac{C_{dd}m}{12\pi\hbar^2} \quad (1.38)$$

and is of extreme importance to compare the value of a_{dd} with the one for the contact s -wave scattering length. The ratio

$$\epsilon_{dd} = \frac{a_{dd}}{a_s} = \frac{C_{dd}m}{12\pi\hbar^2 a_s} \quad (1.39)$$

quantifies the relative strength of the dipolar interaction.

1.2.1 Harmonic confinement of dipolar condensate

To study the equilibrium properties of a dipolar condensate trapped in a harmonic potential it's still possible to use the GPE, generalized to include the dipolar interaction term:

$$\left(-\frac{\hbar^2}{2m}\nabla^2 + V_{ho}(\mathbf{r}) + g|\Psi(\mathbf{r})|^2 + V_{dd}^{mf}(\mathbf{r}) \right) \Psi(\mathbf{r}) = \mu\Psi(\mathbf{r}) \quad (1.40)$$

where

$$V_{dd}^{mf}(\mathbf{r}) = \int d\mathbf{r}' V_{dd}(\|\mathbf{r} - \mathbf{r}'\|) |\Psi(\mathbf{r}')|^2 \quad (1.41)$$

represents the mean field potential determined by the dipolar interaction.

An analytical solution of the GPE can still be obtained in the Thomas-Fermi limit where one neglects the contribution given by the kinetic energy term. In this limit the GPE reduces to

$$V_{ho} + gn + V_{dd}^{mf} = \mu. \quad (1.42)$$

In the presence of an harmonic confinement, that for simplicity we take as axially symmetric ($\omega_x = \omega_y$), if the dipoles are oriented in the z direction the solution for the Thomas-Fermi profile at equilibrium still admits a quadratic dependence on the spatial coordinates

$$n(\mathbf{r}) = n_0 \left(1 - \frac{r_{\perp}^2}{R_{\perp}^2} - \frac{z^2}{Z^2} \right) \quad (1.43)$$

like in the simple contact interaction case. In this equation, $r_{\perp} = (x^2 + y^2)^{1/2}$, R_{\perp} and Z represent the Thomas-Fermi radii in the radial and axial direction, respectively. n_0 is instead the peak density, that is related to the total number of atoms through the relationship $N = (8\pi/15)n_0R_{\perp}^2Z$. The result 1.43 follows from the fact that the dipolar mean field contribution inside the GPE, when evaluated on the density profile 1.43, still shows a quadratic dependence from the coordinates given by

$$V_{dd}^{mf} = \frac{n_0 C_{dd}}{3} \left[\frac{r_{\perp}^2}{R_{\perp}^2} - 2 \frac{z^2}{Z^2} - f(\kappa) \left(1 - \frac{3}{2} \frac{r_{\perp}^2 - 2z^2}{R_{\perp}^2 - Z^2} \right) \right] \quad (1.44)$$

where $\kappa = R_{\perp}/Z$ represents the aspect ratio of the dipolar condensate and $f(\kappa)$ is given by:

$$f(\kappa) = \frac{1 + 2\kappa^2}{1 - \kappa} - \frac{3\kappa^2}{(1 - \kappa)^{3/2}} \tanh^{-1}(\sqrt{1 - \kappa^2}). \quad (1.45)$$

One aspect that is important to notice is given by the fact that the aspect ratio κ of the gas does not coincide with the aspect ratio $\lambda = \omega_z/\omega_{\perp}$ of the external trap. The relationship between these two aspect ratios can be obtained from the self consistent equation:

$$3\kappa^2 \epsilon_{dd} \left[\left(\frac{\lambda^2}{2} + 1 \right) \frac{f(\kappa)}{1 - \kappa^2} - 1 \right] + (\epsilon_{dd} - 1)(\kappa^2 - \lambda^2) = 0 \quad (1.46)$$

from which we see that when there is no dipolar interaction, i.e. $\epsilon_{dd} = 0$, one gets back the result $\kappa = \lambda$.

This phenomenon is called magnetostriction and to better show it off let's consider a spherically symmetric trap. Let's suppose that the atomic cloud can be described by a Thomas-Fermi density given by $n(\mathbf{r}) = n_0(1 - r^2/R^2)$. If we insert this density inside the equation for the mean field dipolar potential we get

$$V_{dd}^{mf}(\mathbf{r}) = \epsilon_{dd} \frac{m\omega_{trap}^2}{5} (1 - 3\cos^2(\theta)) \begin{cases} r^2 & r < R \\ R^5/r^3 & r > R \end{cases} \quad (1.47)$$

from which it follows that the mean field potential has the form of a saddle, with localized minima in the dipoles direction, like its shown in figure 1.3. Because of these potential minima localized in the z direction, it's favorable for the cloud to become oblate in the z direction, even if the trap is spherically symmetric.

1.2.2 Elementary excitations of a uniform dipolar gas

The general form for the excitation spectrum of a uniform weakly interacting Bose gas composed by N particles in a volume V can be easily obtained in the context of Bogoliubov theory and is given by

$$\epsilon^2(\mathbf{q}) = \epsilon_0(\mathbf{q}) [\epsilon_0(\mathbf{q}) + 2n\mathcal{V}(\mathbf{q})] \quad (1.48)$$

where $\epsilon_0(\mathbf{q}) = \hbar^2 q^2 / 2m$, $n = N/V$ and $\mathcal{V}(\mathbf{q})$ represents the Fourier transform of the full interaction potential between the particles, that is given by the sum of the contact and

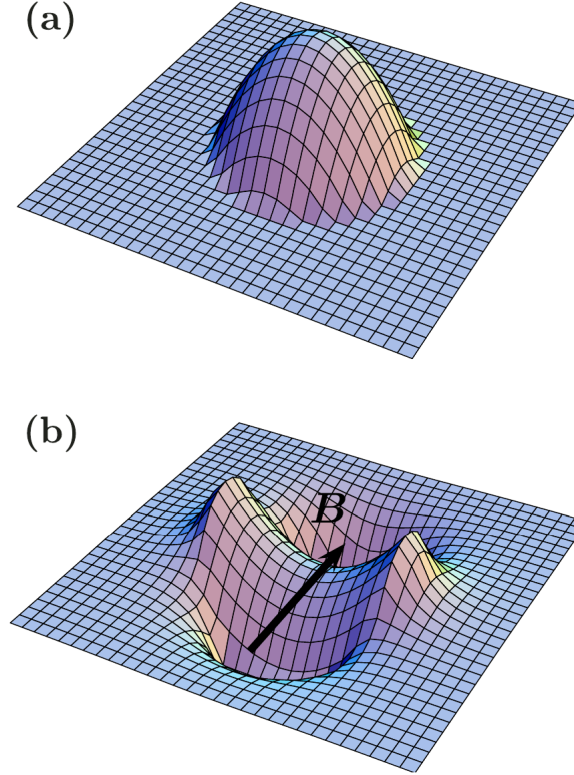


Figure 1.3: (a) Inverted paraboloid that is the density distribution $n(\vec{r})$. (b) V_{dd}^{mf} induced by the density distribution in (a). Image taken from [38].

dipolar terms. If, for the dipolar part, we use equation 1.33 we get the following expression for the Bogoliubov spectrum:

$$\epsilon_{\mathbf{q}}^2 = \epsilon_0(\mathbf{q}) \left[\epsilon_0(\mathbf{q}) + 2gn(1 + \epsilon_{dd}(3 \cos^2 \alpha - 1)) \right]. \quad (1.49)$$

From this spectrum it is possible to characterize the properties of the system in the long wavelength limit $q \rightarrow 0$. For example it is possible to see that in this limit the dispersion law takes the phononic form but with a speed of sound that depends on the angle α between the \mathbf{q} vector and the dipoles' orientation. This speed of sound is given by:

$$c(\theta) = c_0 [1 + \epsilon_{dd}(3 \cos^2(\theta) - 1)]^{1/2} \quad (1.50)$$

where $c_0 = \sqrt{gn/m}$ represents the speed of sound of a non dipolar condensate.

If the condensate is strongly trapped in the dipole's direction, a better potential for the magnetic interaction to be inserted in 1.48 is given by the one expressed in equation 1.34. The spectrum obtained with such a potential for different values of ϵ_{dd} is sketched in figure 1.4. In the figure we can see that by increasing ϵ_{dd} an energy minimum appears in the spectrum for $q \neq 0$. This minimum is analogous to the rotonic minimum that appears in the spectrum of liquid helium that is shown in figure 1.6 but it now arises from the effect of dipolar interactions. For a critical value of ϵ_{dd} this minimum goes to zero when

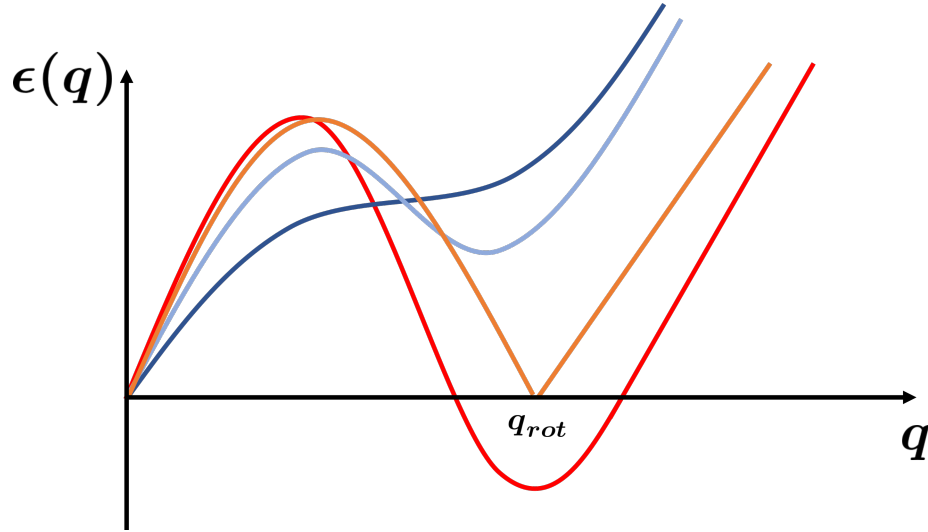


Figure 1.4: Sketch of the excitation spectrum of the pancake shaped dipolar condensate for different values of ϵ_{dd} .

$q = q_{rot}$. This means that the q_{rot} mode can be spontaneously populated even at $T = 0$. When ϵ_{dd} becomes bigger than the critical value ϵ_{dd}^{crit} the energy of the roton mode becomes imaginary and the system becomes unstable to modulations with $q \approx q_{rot}$. In dipolar quantum gases, the value of ϵ_{dd} can be tuned by changing the s -wave scattering length for the contact part of the interaction via Feshbach resonances.

In the mean field approach, the instability cannot be compensated and the gas collapses. However, beyond mean field effects such as the Lee-Huang-Yang (LHY) correction can lead to a stabilization of the new modulated system and bring forth supersolidity.

Thanks to the local density approximation the LHY term can be inserted inside the GPE to get the so called extended Gross-Pitaevskii equation (eGPE) [40]:

$$\left(-\frac{\hbar^2 \nabla^2}{2m} + V_{ext}(\mathbf{r}) + gn(\mathbf{r}) + V_{dd}^{mf}(\mathbf{r}) + \gamma(\epsilon_{dd})n^{3/2}(\mathbf{r}) \right) \Psi(\mathbf{r}) = \mu\Psi(\mathbf{r}) \quad (1.51)$$

where we have defined

$$\gamma(\epsilon_{dd}) = \frac{16}{3\sqrt{\pi}} ga_s^{3/2} \int_0^\pi d\theta \sin \theta [1 + \epsilon_{dd}(3 \cos^2(\theta) - 1)]^{5/2}. \quad (1.52)$$

Thanks to the eGPE it is possible to study dipolar gases throughout all their excitation spectrum and even in the supersolid regime.

1.3 Superfluidity

Superfluidity is a phenomenon strictly connected to the one of Bose-Einstein condensation. Superfluids are characterized by a viscosity equal to zero and can thus flow inside tight capillars without dissipating energy. ^4He superfluidity, below the so called λ point, was

discovered by Kapitza in 1938 [7] and, independently, by Allen and Misener in the same year [6]. This phenomenon was later explained by Landau (1941) [17] who showed that, if the spectrum of elementary excitation of the system followed some specific criteria, then the flow of the fluid could not generate dissipation. In figure 1.5 is shown the phase diagram for ^4He .

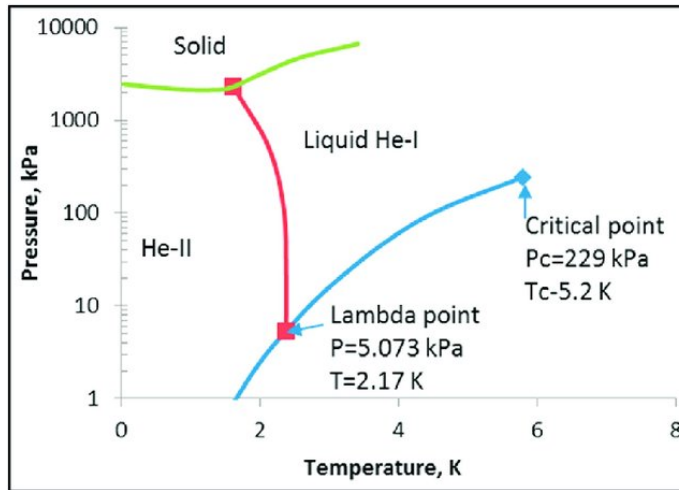


Figure 1.5: Phase diagram for ^4He in proximity of the superfluid phase transition. Image taken from [41].

1.3.1 Landau criterion for superfluidity

In 1938 London proposed an explanation for the concept of superfluidity of liquid helium in terms of Bose-Einstein condensation [42]. By inserting the numbers describing liquid helium inside the BEC equations he got a critical temperature for the transition which was around 2.8 K, that was extremely close to the experimentally determined temperature for the superfluid transition (2.17 K).

Phenomenologically, a critical velocity was observed for the liquid flow, after which the system was no more superfluid. Let's see now what was Landau's argument to describe this result.

Let's consider an impurity of mass M that can move inside the liquid with velocity v . Landau thought that the liquid could be seen as superfluid only if this impurity could move inside the system without creating any excitation. Landau's argument for the breaking of superfluidity takes into account the specific excitation spectrum of the superfluid, shown in figure 1.6. Let's describe with \mathbf{p} the momentum of the elementary excitations and with $\epsilon(\mathbf{p})$ their energy. Before the creation of an excitation the initial energy of the system is given by the kinetic energy of the impurity plus the superfluid's initial energy, that we can take as 0, so that:

$$E_i = \frac{1}{2} M v^2 . \quad (1.53)$$

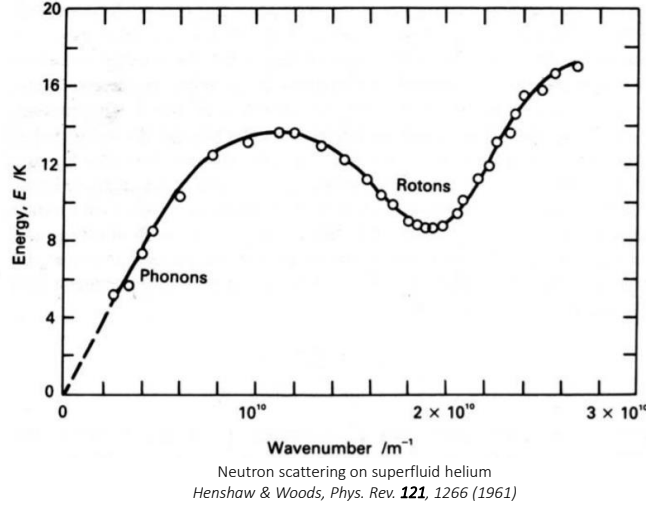


Figure 1.6: Excitation spectrum of superfluid helium. Image taken from [43].

Let's now suppose that the interaction between the superfluid and the impurity generates an excitation with momentum \mathbf{p} . To conserve the total momentum of the system the impurity need to lose \mathbf{p}/M from its initial velocity, so that now the energy of the system is given by

$$E_f = \frac{1}{2}M \left(\mathbf{v} - \frac{\mathbf{p}}{M} \right)^2 + \epsilon(\mathbf{p}). \quad (1.54)$$

The energy difference in this process is given by

$$\begin{aligned} \Delta E &= E_f - E_i = \\ &= \frac{\mathbf{p}^2}{2M} - \mathbf{v} \cdot \mathbf{p} + \epsilon(\mathbf{p}). \end{aligned} \quad (1.55)$$

Landau's argument is that there will be superfluidity if ΔE is greater than 0. In other words, the creation of an excitation should not lower the system's energy:

$$\Delta E > 0 \quad \forall \mathbf{p} \Rightarrow \text{Superfluidity.} \quad (1.56)$$

We can rewrite this condition in the following way

$$\epsilon(\mathbf{p}) > \left(\mathbf{v} \cdot \mathbf{p} - \frac{\mathbf{p}^2}{2M} \right)_{max} \xrightarrow{M \rightarrow \infty} v p. \quad (1.57)$$

For the system to be superfluid we then have to impose that the impurity velocity should be less than a critical value v_c

$$v < \left(\frac{\epsilon(\mathbf{p})}{p} \right)_{min} = v_c. \quad (1.58)$$

To see if this condition can be satisfied it is necessary to know the excitation spectrum ϵ . By considering a weakly interacting Bose gas we have that

$$\epsilon(p) = \left[(cp)^2 + \left(\frac{\mathbf{p}^2}{2m} \right)^2 \right]^{1/2} \xrightarrow{p \rightarrow 0} cp \quad (1.59)$$

and from this expression we see that in weakly interacting Bose gases the Landau's critical velocity is given by the speed of sound $v_c = c$.

The Landau criterion holds also for strongly interacting superfluids such as liquid ^4He , even if in this case v_c is seen to be smaller than the sound velocity because of more complex structures in the excitation spectrum.

For an ideal Bose gas, we instead have that $\epsilon(\mathbf{p}) = \mathbf{p}^2/2m$ and in this case we get that $v_c = 0$. Because of this argument we can say that an ideal BEC is not a superfluid.

1.3.2 Two fluid theory

A useful description of superfluidity is given by two-fluids hydrodynamics. In this description we think of the system at a finite temperature as composed by two different phases. One is a normal viscous liquid while the other is superfluid.

Let's call with \mathbf{v}_n the velocity for the normal part of the fluid and with \mathbf{v}_s the velocity of the superfluid. The distribution $N_{\mathbf{p}}$ of elementary excitation in the system can be written as

$$N_{\mathbf{p}} = \frac{1}{\exp\left(\frac{\epsilon(\mathbf{p}) + \mathbf{p} \cdot (\mathbf{v}_s - \mathbf{v}_n)}{k_B T}\right) - 1} \quad (1.60)$$

This distribution will be greater than zero for all values of \mathbf{p} only if $\|\mathbf{v}_s - \mathbf{v}_n\|$ is less than the critical value v_c . Because of this $N_{\mathbf{p}}$ is thus consistent with the Landau criterion. Equation 1.60 only makes sense if the system is in thermodynamic equilibrium. This implies that there should be no friction between the normal and superfluid components. In accordance with the picture described until now, we can write the system's density as the sum between the normal and superfluid components:

$$\rho = \rho_s + \rho_n \quad (1.61)$$

The mass density current (which represents the total momentum for unit volume) can be written as

$$m\mathbf{j} = \rho_s \mathbf{v}_s + \rho_n \mathbf{v}_n \quad (1.62)$$

Let's consider the frame of reference where the superfluid is still. Here we have that

$$m\mathbf{j} = \rho_n \mathbf{v}_n \quad (1.63)$$

The total momentum carried by the system can be written as $\mathbf{P} = \sum_{\mathbf{p}} N_{\mathbf{p}} \mathbf{p}$. This expression can be written for unit volume in the following way

$$m\mathbf{j} = \int \frac{d\mathbf{p}}{(2\pi\hbar)^3} \mathbf{p} N_{\mathbf{p}} \quad (1.64)$$

which implies that

$$\rho_n \mathbf{v}_n = \int \frac{d\mathbf{p}}{(2\pi\hbar)^3} \mathbf{p} N_{\mathbf{p}} \quad (1.65)$$

where $N_{\mathbf{p}}$ is given by equation 1.60 with $\mathbf{v}_s = 0$. By expanding $N_{\mathbf{p}}$ in powers of \mathbf{v}_n and by keeping only the linear term we get

$$\rho_n = -\frac{1}{3} \int \frac{d\mathbf{p}}{(2\pi\hbar)^3} p^2 \left. \frac{dN_{\mathbf{p}}}{d\epsilon} \right|_{\mathbf{v}_n=0}. \quad (1.66)$$

This is the central result for Landau's theory because it allows the calculation of the normal part of the density in terms of the distribution $N_{\mathbf{p}}$. This equation is only valid in the limit where the elementary excitations are well defined and they do not interact with one another. This condition is generally satisfied for uniform systems under the critical temperature.

From equation 1.66 is possible to arrive at the result that ρ_n coincides with the thermal fraction of the system only for sufficiently high temperatures.

1.3.3 Vortices

The Vortex solution of the GPE shows non trivial features given by the presence of a region of space where the density goes to 0. The size of this region is of the order of the healing length. Vortices are generally not a stable configuration for the system, and only in reference frames that rotate at sufficiently high angular velocities they represent a local minimum for the energy functional associated with the GPE.

The study of vortices is of fundamental importance in the context of rotation for superfluids. This is because it is known that the velocity field of a classical system rotating with angular velocity Ω is given by the rigid body formula $\mathbf{v} = \Omega \times \mathbf{r}$ so that $\nabla \times \mathbf{v} = 2\Omega \neq 0$. This velocity field contradicts the irrotationality condition for superfluids, that are thus expected to rotate in a different way.

To discuss this point lets consider a gas confined in a macroscopic cylinder of radius R and length L . We want to find solutions for the GPE that correspond to rotations around the cylinder's axis. Given the symmetry of the system we can search for solutions of the form

$$\Psi_0(\mathbf{r}) = e^{is\varphi} |\Psi_0(r)| \quad (1.67)$$

where we introduced cylindrical coordinates. For the order parameter to be well defined, we need to impose that the phase term remains the same when we shift φ by 2π . This condition, also called single valuedness condition, is only true if we impose $s \in \mathbb{Z}$. Since the angular momentum operator is given in cylindrical coordinates by $L_z = \sum_N \ell_z = -i\hbar N \partial_\varphi$, we can see that the order parameter as written in equation 1.67 is an eigenfunction of the z component of the angular momentum with $L_z = Ns\hbar$. Equation 1.67 represents a gas that is rotating around the z axis with the following velocity

$$\mathbf{v}_s = \frac{\hbar s}{m r} \hat{\varphi}. \quad (1.68)$$

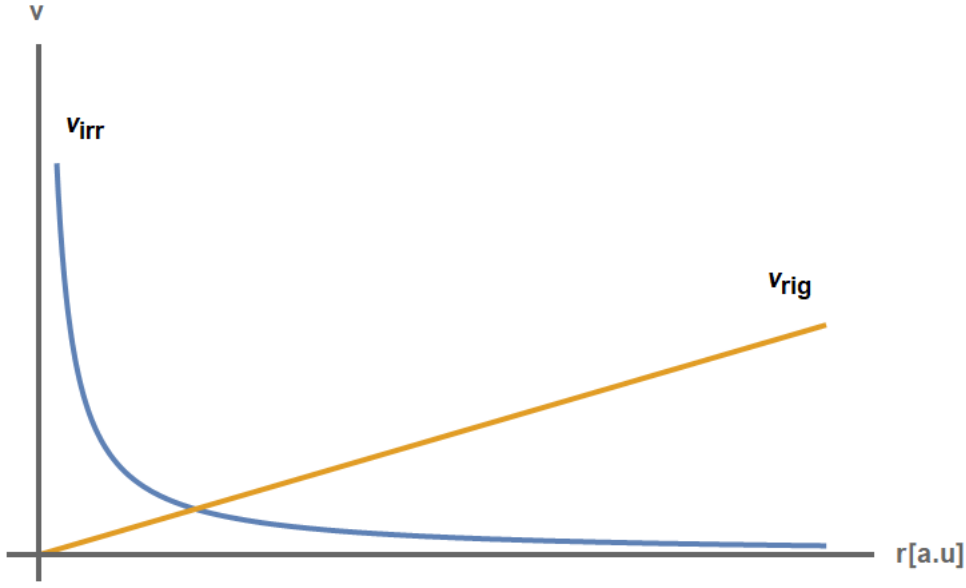


Figure 1.7: Comparison between the velocity field of the superfluid v_{irr} and the rigid body one v_{rig} .

This expression is totally different from the rigid rotator formula $\mathbf{v} = \boldsymbol{\Omega} \times \mathbf{r}$, that is still tangential, but whose modulus increases with r . In figure 1.7 is shown a comparison between the two velocities.

The circulation of the velocity along a closed line around the z -axis is given by

$$\oint_{\gamma} \mathbf{v}_s \cdot d\boldsymbol{\ell} = \int_0^{2\pi} \frac{\hbar}{m} s d\varphi = 2\pi s \frac{\hbar}{m} = s \frac{h}{m} \quad (1.69)$$

and it is quantized in steps of h/m , independently from the radius of the circuit γ chosen to make the integral. Since the integrand is proportional to a gradient, one can also use the Stokes theorem to evaluate the integral

$$\oint_{\gamma} \mathbf{v}_s \cdot d\boldsymbol{\ell} = \frac{\hbar}{m} \oint_{\gamma} \nabla \phi \cdot d\boldsymbol{\ell} = \frac{\hbar}{m} \int_S \nabla \times \nabla \phi \cdot d\mathbf{S} \quad (1.70)$$

where $\partial S = \gamma$, $d\mathbf{S} = \hat{n} dS$ and \hat{n} represents the unit vector normal to the surface S . The circulation calculated in this way is 0 since the curl of a gradient is always 0. To make the two results for the circulation coincide (when $s \neq 0$) we need to observe that Stokes theorem can only be applied if ϕ satisfies some regularity conditions, and this is true except where the modulus of the wavefunction (i.e. the density) is equal to 0. To make the two results coincide we then need to have inside γ some places where the gas' density goes to 0. These points will thus represent the central points for the emerging vortices.

The Gross-Pitaevskii equation written in cylindrical coordinates for this system is given by

$$-\frac{\hbar^2}{2m} \frac{1}{r} \frac{d}{dr} \left(r \frac{d|\Psi_0|}{dr} \right) + \frac{\hbar^2 s^2}{2mr^2} |\Psi_0| + g |\Psi_0|^3 = \mu |\Psi_0|. \quad (1.71)$$

If we now make the assumption that at long distances from the vortex' center the density of the gas should coincide with its uniform value we can introduce the following ansatz

$$|\Psi_0| = \sqrt{n}f(\eta) \quad f(\eta \rightarrow \infty) = 1 \quad (1.72)$$

where $\eta = r/\xi$. By inserting this ansatz into the GPE we get

$$\frac{1}{\eta} \frac{d}{d\eta} \left(\eta \frac{df}{d\eta} \right) + \left(1 - \frac{s^2}{\eta^2} \right) f - f^3 = 0. \quad (1.73)$$

For $\eta \rightarrow 0$ the dominant terms in this equation are given by

$$\frac{1}{\eta} f' - \frac{s^2}{\eta^2} f = 0. \quad (1.74)$$

This differential equation admits as a solution $f \sim \eta^{|s|}$ and because of this we can see that the density $|\Psi_0(r)|^2$ tends to 0 when approaching the axis of the vortex.

From the dimensionless nature of this differential equation we see that the region near the vortex line in which the density is significantly different from \sqrt{n} is of the order of the healing length ξ of the condensate.

1.3.4 Superfluids under rotation

Let's consider a superfluid at a finite temperature that is enclosed in a cylinder that can rotate about its axis of symmetry. If this cylinder is put under rotation, only the normal component of the liquid shall rotate with it. If the angular velocity is sufficiently small, the superfluid component will remain still. If instead this angular velocity exceeds some critical value, than the state where the superfluid is immobile will become energetically unstable. The reason for this is that, in the frame of reference that is rotating with the same angular velocity as the container, that is the system where we expect the onset of thermodynamic equilibrium, the quantity that needs to be minimized is given by

$$E_r = E - \mathbf{\Omega} \cdot \mathbf{L} \quad (1.75)$$

where E and \mathbf{L} are, respectively, the energy and angular momentum of the superfluid in the laboratory reference frame and $\mathbf{\Omega}$ is the angular velocity of the container. From this expression we can see that, for sufficiently big $\mathbf{\Omega}$, states in which $\mathbf{\Omega} \cdot \mathbf{L} > 0$ become favorable with respect to the ones in which $L = 0$, that correspond to the non rotating superfluid.

Since a superfluid cannot rotate in a rigid way, rotations inside the superfluid will be accompanied by the creation of quantized vortices. Let's consider a single vortex that is generated around the symmetry axis of the cylinder. From equation 1.68 we know that the superfluid velocity is given in this case by

$$\mathbf{v}_s = \frac{\hbar s}{m r} \hat{\phi} \quad s \in \mathbb{Z}. \quad (1.76)$$

This velocity is extremely different from the one of the rigid rotator, given by $v = \Omega r$. The angular momentum of the superfluid in this configuration is given by

$$L_z = \int d\mathbf{r} \rho_s v_s r = \pi R^2 L \rho_s \frac{\hbar}{m} s \quad (1.77)$$

where L represents the length of the cylinder and R its radius, so that $\pi R^2 L$ is the volume of the cylinder. In deriving this expression we implicitly supposed that the radius r_c of the vortex, that characterizes the distance in which ρ_s is significantly perturbed from its average value, is much less than R , and ρ_s in the equation is the value for the superfluid density in the bulk of the system.

The energy associated to this vortex state is given by

$$E_v = \int \frac{1}{2} \rho_s v_s^2 d\mathbf{r} = L \pi \rho_s s^2 \left(\frac{\hbar}{m} \right)^2 \log \left(\frac{R}{r_c} \right) \quad (1.78)$$

where the radial integration was taken from r_c to R . From this expression we see that the dependence of E_v from r_c is logarithmic and thus the energy of the vortex depends weakly from its radius.

The expressions for L_z and for E_v show why the states with $|s| > 1$ are not stable. This is because $L_z \sim s$ while $E_v \sim s^2$ so that the energy to be minimized (that is given by $E_v - \omega L_z$) increases with s .

Using the expression for E_v we are now capable of determining the critical value Ω_c for the existence of a stable vortex. This is the value one obtains when $E_v = 0$ and is given by

$$\Omega_c = \frac{E_v}{L_z} = \frac{\hbar}{m R^2} \log \left(\frac{R}{r_c} \right) \quad (1.79)$$

for vortices carrying a single quantum of circulation ($s = 1$). If one considers angular velocities that are bigger than Ω_c other vortices will appear inside the superfluid.

1.4 Supersolids under rotation

1.4.1 Introduction

A supersolid is a unique and intriguing state of matter that combines the properties of both a solid and a superfluid. In a supersolid, the atoms forming it spontaneously arrange themselves in such a way that a density modulation appears inside the system. This density modulation of the ground state results in a symmetry breaking since no external potential is inducing this modulation and no trace of it can be found in the original hamiltonian. Thanks to this density modulation, supersolids show a reduced superfluid fraction with respect to a regular superfluid even at $T = 0$ when no thermal component is present. Because of this, supersolids behave in a completely different way when they are put under rotation. In figure 1.8 is showed what happens when, instead of applying rotations to a perfect superfluid, one considers a supersolid.

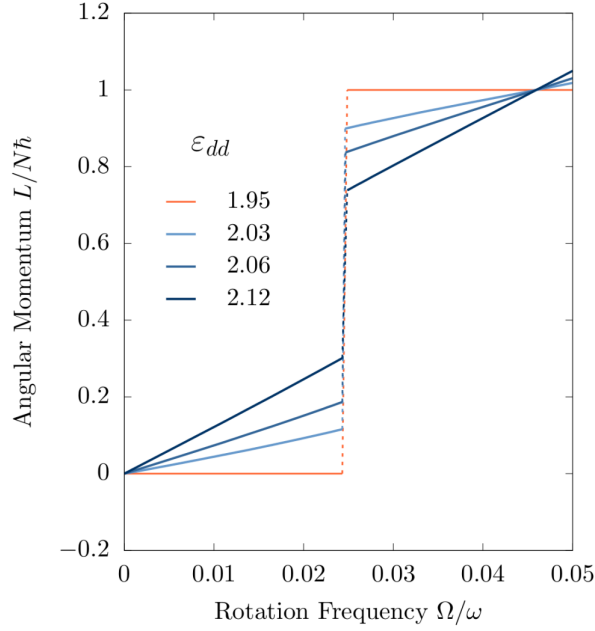


Figure 1.8: Angular momentum $L/N\hbar$ of the ground state in the rotating frame, as a function of rotation frequencies for different values of ϵ_{dd} i.e. through the superfluid to supersolid phase transition. In the superfluid phase ($\epsilon_{dd} = 1.95$) its possible to observe the jump of angular momentum that is typical of superfluids. In the supersolid case the linear gain in angular momentum before and after jumps reflects the response to rotation of the solid part. Image taken from [44].

This figure shows that, even for supersolids, one has jumps in angular momentum that are still related to the creation of vortices. What is different from the case of perfect superfluidity is the fact that the supersolid, thanks to its solid part, can acquire angular momentum even before exciting vortices, and the gain in angular momentum that the system obtains when exciting a vortex is less than $\hbar N$ by a factor that depends on the superfluid fraction. In 1970 Leggett developed a theory that is able to predict the first branch of figure 1.8 before the excitation of vortices. In this theory he was able to relate the superfluid fraction with the density of the system.

1.4.2 Leggett's theory on the rotation of supersolids

Let's consider N atoms confined in a cylindrical annulus that has internal radius R and thickness d . Suppose we rotate the enclosing surfaces of the cylinder at a constant angular velocity ω . The free energy of the system in the rest frame is assumed to be of the form

$$F(\omega) = F_0 + \frac{1}{2}I_0\omega^2 + \Delta F(\omega) \quad (1.80)$$

where F_0 represents the free energy when $\omega = 0$, I_0 is the classical moment of inertia of the system that can be written as NmR^2 if we neglect terms in d/R , and $I_0\omega^2/2$ represents

the classical contribution to the free energy when the annulus is rotating.

The term $\Delta F(\omega)$ represents the difference between $F(\omega)$ and the classical result and is assumed to be an even function of ω that is also periodic with period ω_0 where

$$\omega_0 = \frac{\hbar}{\alpha m R^2} . \quad (1.81)$$

We can write the function $\Delta F(\omega)$ in the form

$$\Delta F(\omega) = -\frac{1}{2} \frac{\rho_s}{\rho} I_0 \omega^2 \quad (1.82)$$

and this equation defines the superfluid fraction as $f_s = \rho_s/\rho$, where ρ_s represents the superfluid density and ρ the total one.

Thanks to this definition we can write the total free energy of the system as

$$F(\omega) = F_0 + \frac{1}{2} I \omega^2 \quad (1.83)$$

where the moment of inertia of the system I is now renormalized to take into consideration its superfluid properties

$$I = (1 - \rho_s/\rho) I_0 . \quad (1.84)$$

We now want to give an estimate of this superfluid fraction.

When the enclosing walls are at rest the ground state wave function $\Psi_0(\mathbf{r}_1, \dots, \mathbf{r}_i, \dots, \mathbf{r}_N)$ and its corresponding energy can be found by minimizing the expectation value of the hamiltonian \mathcal{H} subject to appropriate boundary constraints.

The full hamiltonian of the system is given by

$$\mathcal{H} = -\frac{\hbar^2}{2m} \sum_{i=1}^N \nabla_i^2 + \frac{1}{2} \sum_{i \neq j}^N U(\mathbf{r}_i - \mathbf{r}_j) + \sum_{i=1}^N V(\mathbf{r}_i) \quad (1.85)$$

where $V(\mathbf{r})$ represents a single particle potential that takes into account the confinement of the annulus' walls and $U(\mathbf{r}_i - \mathbf{r}_j)$ represents instead the interparticle interaction potential. The constraints which the wavefunction must obey are the requirement of symmetry (or antisymmetry) with respect to the interchange of any two identical particles, but also the condition of single valuedness with respect to each coordinate \mathbf{r}_i .

If we now introduce, for every atom, cylindrical polar coordinates (r_i, θ_i, z_i) in the usual way, the single valuedness condition can be written in the following way

$$\begin{aligned} \Psi_0(r_1, \theta_1, z_1, \dots, r_i, \theta_i + 2\pi, z_i, \dots, r_N, \theta_N, z_N) = \\ = \Psi_0(r_1, \theta_1, z_1, \dots, r_i, \theta_i, z_i, \dots, r_N, \theta_N, z_N) \quad \forall i . \end{aligned} \quad (1.86)$$

From this point forward, we suppress the r and z coordinates if they are not needed.

Let's now consider what happens when the enclosing surfaces of the annulus are rotated with constant angular velocity ω . The potential V will now be time dependent in the rest frame. This problem can be solved by just changing the reference frame to the one

that's comoving with the walls. To do this we need to use the Formula for the Galilean transformation of a wave function and apply it to the ground state.

If we change our description to a reference frame that is moving at a relative velocity \mathbf{v} with respect to the previous one, the wavefunction transforms according to this equation:

$$\Psi'(\mathbf{r}, t) = \Psi(\mathbf{r} - \mathbf{v}t, t) \exp\left\{\frac{i}{\hbar} \left(m\mathbf{v} \cdot \mathbf{r} - \frac{1}{2}m\mathbf{v}^2t\right)\right\}. \quad (1.87)$$

In our case the velocity between the 2 reference frames is given by $\mathbf{v} = -\omega R\hat{\theta}$ which means that the new ground state will be given by

$$\Psi'_0(\theta_1, \dots, \theta_i, \dots, \theta_N) = \Psi_0(\theta'_1, \dots, \theta'_i, \dots, \theta'_N) \exp\left\{-im\omega R^2 \sum_i \theta'_i(t)/\hbar\right\} \quad (1.88)$$

where we have defined $\theta'_i = \theta_i - \omega t$.

Of course, when $\omega = 0$ the new ground state coincides with the rest frame one.

In this new frame of reference, the single valuedness condition now becomes

$$\Psi_0(\theta_1, \dots, \theta_i + 2\pi, \dots, \theta_N) = \exp\left\{-2\pi im\omega R^2/\hbar\right\} \Psi_0(\theta_1, \dots, \theta_i, \dots, \theta_N). \quad (1.89)$$

We can now minimize \mathcal{H} with this new boundary condition. This will give rise to a ground state energy that, in principle, will depend on ω . We call this energy $E_0(\omega)$.

Since we are working at $T = 0$ we can immediately find from the definition of $\Delta F(\omega)$ that

$$\Delta F(\omega) = E_0 - E_0(\omega) \quad (1.90)$$

and from this equation we can see that, if $E_0(\omega)$ does not depend on ω , then $\Delta F = 0$ and the system cannot be superfluid.

From the inspection of the boundary condition 1.89 we also find that $E_0(\omega + \hbar/mR^2) = E_0(\omega)$ which means that the quantity α defined in 1.81 needs to be an integer.

We can now try and give an estimate of the energy $E_0(\omega)$ using a variational approach. To do this we construct a trial function that satisfies the boundary condition 1.89 in the following way

$$\Psi(\mathbf{r}_1, \dots, \mathbf{r}_N; \omega) = \exp\left\{i \sum_{i=1}^N \varphi(\mathbf{r}_i; \omega)\right\} \Psi_0(\mathbf{r}_1, \dots, \mathbf{r}_N) \quad (1.91)$$

where the function $\varphi(\mathbf{r})$ is real and satisfies

$$\varphi(\theta + 2\pi) = \varphi(\theta) - 2\pi m\omega R^2/\hbar \quad (1.92)$$

whereas Ψ_0 represents the ground state wavefunction in the rest frame and so it satisfies the single valuedness condition given in 1.86. Given this we see that the wavefunction defined in 1.91 satisfies the boundary condition 1.89 and is then a good trial function.

Using Ψ to calculate the expectation value of \mathcal{H} we get²

$$\langle \mathcal{H} \rangle_{trial} = E_0 + \frac{\hbar^2}{2m} \int (\nabla \varphi)^2 \rho(\mathbf{r}) d\mathbf{r} \quad (1.93)$$

²To get this result one needs to use the fact that the ground state function in the rest frame is real.

where

$$\rho(\mathbf{r}) = \int \prod_{i=2}^N d\mathbf{r}_i |\Psi_0(\mathbf{r}, \mathbf{r}_2, \dots, \mathbf{r}_N)|^2 \quad (1.94)$$

represents the single particle density.

Since we are neglecting terms in d/R , we can “Unroll” the annulus to form a rectangular parallelepiped of length $2\pi R$ and change the boundary condition 1.92 on φ to the following

$$\varphi(x + 2\pi R, y, z) = \varphi(x, y, z) - 2\pi m R^2 \omega / \hbar \quad (1.95)$$

where x, y, z are cartesian coordinates and x runs from 0 to $2\pi R$.

If we now take for simplicity a trial function where φ is a function of x only, we can apply the standard calculus of variation to minimize 1.93 that can now be written as

$$\langle \mathcal{H} \rangle_{trial} = E_0 + \frac{\hbar^2}{2m} \int dx dy dz (\partial_x \varphi(x))^2 \rho(x, y, z) \quad (1.96)$$

by defining $\tilde{\rho}(x) = \int dy dz \rho(x, y, z)$ we get

$$\langle \mathcal{H} \rangle_{trial} = E_0 + \frac{\hbar^2}{2m} \int_0^{2\pi R} dx (\partial_x \varphi(x))^2 \tilde{\rho}(x) \quad (1.97)$$

and, by the theory of the calculus of variations, the function $\varphi(x)$ that minimizes this energy will be the one for which the functional derivative of $\langle \mathcal{H} \rangle$ with respect to ϕ is equal to 0:

$$\frac{\delta \langle \mathcal{H} \rangle_{trial}}{\delta \varphi(x)} = 0. \quad (1.98)$$

Evaluating this functional derivative we get

$$\partial_x (\tilde{\rho}(x) \partial_x \varphi(x)) = 0. \quad (1.99)$$

Solving this simple equation we get the following expression for the phase

$$\varphi(x) = \int_0^x \frac{c}{\tilde{\rho}(x)} dx. \quad (1.100)$$

Using the boundary condition 1.92 we get

$$-2\pi m R^2 \omega / \hbar = \int_0^{2\pi R} \frac{c}{\tilde{\rho}(x)} dx \quad (1.101)$$

which means that, by defining k such that

$$\frac{1}{k} = \frac{1}{\lambda} \int_0^\lambda \frac{1}{\tilde{\rho}(x)} dx \quad (1.102)$$

we can write the integration constant c as

$$c = -\frac{m R \omega}{\hbar} k \quad (1.103)$$

and by inserting this result in the expression for the phase we get

$$\varphi(x) = -\frac{mR\omega}{\hbar}k \int_0^x \frac{1}{\tilde{\rho}(x)} dx . \quad (1.104)$$

By inserting this result in the expression for $\langle \mathcal{H} \rangle$ we get

$$\langle \mathcal{H} \rangle_{trial} = E_0 + \frac{1}{2}NmR^2\omega^2 f_s^+ \quad (1.105)$$

where we have defined f_s^+ as

$$f_s^+ = \left[\frac{1}{\lambda} \int_0^\lambda \frac{dx}{\tilde{\rho}(x)/\bar{\rho}} \right]^{-1} \quad (1.106)$$

where $\bar{\rho} = N/2\pi R$.

Since we have worked with a trial function and not with the real groundstate, we know that the energy calculated in this way will always be bigger than the real ground state energy. Given this and comparing 1.105 with equation 1.82 we see that f_s^+ represents an upper bound for the real superfluid fraction of the system

$$f_s \leq f_s^+ . \quad (1.107)$$

For a normal superfluid, $\tilde{\rho}(x) = \bar{\rho}$ which means that $f_s^+ = 1$ and this inequality only gives the trivial result that $\rho_s \leq \rho$.

When instead we are dealing with a ground state density that is not translationally invariant, as is the case of the supersolid, we get the non trivial result $f_s^+ < 1$.

Given the expression for the trial ground state wavefunction 1.91, we can use the standard expression $\hbar\partial_x\varphi/\hbar$ to get the velocity field in Leggett's theory [45]

$$v(x) = -\omega R \frac{k}{\tilde{\rho}(x)} . \quad (1.108)$$

For a uniform superfluid we have $\rho(x) = \text{const.}$ so that the velocity field will be constant and equal to $-\omega R$.

Equation 1.108 represents the result for the velocity field in the rotating frame. To get the velocity in the lab frame one needs to make the Galilean transformation back by writing $v_{lab} = v + \omega R$. In this way we get the known result that a perfect superfluid in the laboratory frame does not move, $v_{lab} = \omega R - \omega R = 0$.

The full result for v_{lab} when we consider a generic $\tilde{\rho}(x)$ is given by

$$v_{lab}(x) = \omega R \left(1 - \frac{k}{\tilde{\rho}(x)} \right) \quad (1.109)$$

and we see that this expression will be different from zero when $\tilde{\rho}(x)$ is a modulated function, like it happens in a supersolid.

We can now calculate the moment of inertia of the system from its definition as the ratio between the angular momentum and the angular frequency

$$I = \frac{\langle L \rangle}{\omega} \quad (1.110)$$

where $L = mNRv_{lab}$ represents the angular momentum in the lab frame and where $\langle \cdot \rangle = \int dx \cdot \tilde{\rho}(x)$.

Inserting equation 1.109 inside the expression for the angular momentum we get

$$I = mNR^2(1 - f_s^+) = I_0(1 - f_s^+) \quad (1.111)$$

which is consistent with equation 1.84 and the fact that we are using a variational ansatz.

1.5 Dynamical Polarizability

Let's consider an atom described by its unperturbed Hamiltonian \mathcal{H}_0 . Let's call the ground state of this Hamiltonian $|0\rangle$ and its energy ϵ_0 . Let's suppose that this atom is now perturbed by the interaction with an external electric field \mathbf{E} oscillating with angular frequency ω .

The Hamiltonian that describes this interaction can be written in the dipole approximation as:

$$\mathcal{H}' = -\mathbf{D} \cdot \mathbf{E}(a + a^\dagger) \quad (1.112)$$

where a^\dagger, a are the second quantization operators that create and destroy a photon with energy $\hbar\omega$ respectively, $\mathbf{D} = -e \sum_i \mathbf{r}_i$ represents the electric dipole operator of the atom, \mathbf{r}_i represents the position of the i -th electron with respect to the atomic center of mass, e is the absolute value of the electronic charge and the sum runs on all the electrons.

By supposing that $\mathcal{H}' \ll \mathcal{H}_0$ we can work in the framework of perturbation theory and say that, to first order in \mathcal{H}' , the correction to the energy of the ground state of the system due to the perturbation can be written as

$$\Delta E^{(1)} = \langle \text{GS} | \mathcal{H}' | \text{GS} \rangle \quad (1.113)$$

where, since we are working in second quantization for the electric field, we need to take into consideration also the quantum state of the light, which we suppose it's of the form $|\kappa\rangle$, where κ represents the number of photons, so that $|\text{GS}\rangle = |\kappa\rangle |0\rangle$ represents the tensor product of the atom and light states. This state has energy $\epsilon_0 + \kappa\hbar\omega$.

Since the atom in the ground state is spherically symmetric, $|0\rangle$ is a state with well defined parity and so $\Delta E^{(1)} = 0$ because the dipole is an odd operator under parity.

To get the first non trivial correction to the ground state energy we have to go to the next order in the expansion that can be written in the following way

$$\Delta E^{(2)} = \sum_{n, \kappa'} \frac{|\langle \text{GS} | \mathcal{H}' | \kappa', n \rangle|^2}{\epsilon_0 + \kappa\hbar\omega - (\epsilon_n + \kappa'\hbar\omega)} \quad (1.114)$$

where $|n\rangle$ represents an excited state of the atom with energy ϵ_n , $|\kappa'\rangle$ is a Fock state for the light with energy $\kappa'\hbar\omega$ and the sum runs on all the states of the system except for the ground state.

Seeing as though the light field part of \mathcal{H}' can both create and destroy a photon with energy $\hbar\omega$ and since both of these processes contribute to the expression 1.114, we can trace out the light part and arrive at the expression

$$\Delta E^{(2)} = \frac{1}{\hbar} \sum_n |\langle 0|\mathbf{D} \cdot \mathbf{E}|n\rangle|^2 \left(\frac{1}{\omega_{n0} - \omega} + \frac{1}{\omega_{n0} + \omega} \right) \quad (1.115)$$

for the leading order correction to the atomic ground state energy, where we have introduced the notation $\omega_{n0} = (\epsilon_n - \epsilon_0)/\hbar$ for the atomic transition frequencies.

By writing explicitly the absolute value in $\Delta E^{(2)}$, we can write the left hand side in 1.115 as

$$\langle 0|\mathbf{D} \cdot \mathbf{E} \sum_n \frac{|n\rangle\langle n|}{\hbar} \left(\frac{1}{\omega_{n0} - \omega} + \frac{1}{\omega_{n0} + \omega} \right) \mathbf{D} \cdot \mathbf{E}^* |0\rangle. \quad (1.116)$$

If we now define the operator

$$\mathcal{X} := \frac{1}{\hbar} \sum_n |n\rangle\langle n| \left(\frac{1}{\omega_{n0} - \omega} + \frac{1}{\omega_{n0} + \omega} \right) \quad (1.117)$$

we get the important result that $\Delta E^{(2)}$ can be seen as the expectation value on the atomic ground state of the operator:

$$\mathcal{H}^s = \mathbf{D} \cdot \mathbf{E} \mathcal{X} \mathbf{D} \cdot \mathbf{E}^* \quad (1.118)$$

that we call *Stark operator* [46].

Equation 1.118 is clearly made by the product of two rank-1 tensors (or vectors) and a rank-0 one (or scalar). Because of this \mathcal{H}^s can be decomposed through its irreducible representation as [47]

$$\mathcal{H}^s = \sum_{\ell=0}^2 \{\mathbf{D}\mathcal{X}\mathbf{D}\}^\ell : \{\mathbf{E}\mathbf{E}^*\}^\ell \quad (1.119)$$

where we have introduced the double dot notation to define the scalar product between two tensors of the same rank as:

$$\{\mathbf{D}\mathcal{X}\mathbf{D}\}^K : \{\mathbf{E}\mathbf{E}^*\}^K := \sum_{Q=-K}^K (-1)^K \{\mathbf{D}\mathcal{X}\mathbf{D}\}_Q^K \{\mathbf{E}\mathbf{E}^*\}_{-Q}^K. \quad (1.120)$$

In this expression the brackets are defined in terms of the Clebsch-Gordan coefficients by

$$\begin{aligned} \{\mathbf{D}\mathcal{X}\mathbf{D}\}_Q^K &= \sum_{qq'} \langle 11qq'|11KQ\rangle D_q \mathcal{X} D_{q'} \\ \{\mathbf{E}\mathbf{E}^*\}_Q^K &= \sum_{qq'} \langle 11qq'|11KQ\rangle E_q E_{q'}^* \end{aligned} \quad (1.121)$$

and the components D_q, E_q are given by

$$\begin{aligned} D_{\pm 1} &= \mp \frac{1}{\sqrt{2}} (D_x \pm iD_y) & D_0 &= D_z \\ E_{\pm 1} &= \mp \frac{1}{\sqrt{2}} (E_x \pm iE_y) & E_0 &= E_z \end{aligned} \quad (1.122)$$

By writing explicitly each term of the summation in 1.119 we get

$$\mathcal{H}^s = \mathcal{H}^{scal} + \mathcal{H}^{vect} + \mathcal{H}^{tens} . \quad (1.123)$$

Because we are interested in working with linearly polarized light, we can make the assumption that $\mathbf{E} \equiv \mathbf{E}^*$ and since $\{\mathbf{E}\mathbf{E}^*\}^1 \propto \mathbf{E} \times \mathbf{E}^*$, we get that in this limit $\mathcal{H}^{vect} = 0$ and our Stark operator is represented only by a scalar and a tensor part.

We are now ready to be more specific about the form of the operators \mathcal{H}^{scal} and \mathcal{H}^{tens} . Since we are dealing with an unperturbed atom, its ground state can be written as

$$|0\rangle = |\gamma FM\rangle \quad (1.124)$$

where F represents the quantum number associated with the total angular momentum \mathbf{F} , M represents its projection onto the z direction and γ is a placeholder for all the other quantum numbers that define the state.

If there is no magnetic field present in the system, the ground state has a $(2F + 1)$ -fold degeneracy and the new ground state can be obtained by diagonalizing \mathcal{H}^s in this manifold. This can be done by making use of the Wigner-Eckart theorem to obtain

$$\langle \gamma FM | \mathcal{H}^{scal} | \gamma FM' \rangle = \frac{\delta_{MM'}}{\sqrt{2F+1}} \langle \gamma F || \mathbf{D} \cdot \chi \mathbf{D} || \gamma F \rangle E^2 \quad (1.125)$$

and

$$\langle \gamma FM | \mathcal{H}^{tens} | \gamma FM' \rangle = \sum_{Q=-2}^2 (-1)^{F-M} \begin{pmatrix} F & 2 & F \\ -M & Q & M' \end{pmatrix} \langle \gamma F || \{\mathbf{D}\chi\mathbf{D}\}^2 || \gamma F \rangle (-1)^Q \{\mathbf{E}\mathbf{E}\}_{-Q}^2 \quad (1.126)$$

where $\langle || \dots || \rangle$ represents a reduced matrix element and where we have introduced the Wigner $3jm$ symbols defined through the Clebsch-Gordan coefficient by:

$$\begin{pmatrix} j_1 & j_2 & j_3 \\ m_1 & m_2 & m_3 \end{pmatrix} = \frac{(-1)^{j_3+m_3+2j_1}}{\sqrt{2j_3+1}} \langle j_1 j_2 - m_1 - m_2 | j_1 j_2 j_3 m_3 \rangle . \quad (1.127)$$

These matrix elements of \mathcal{H}^{scal} and \mathcal{H}^{tens} are seen to depend only on one atomic quantity, which is a reduced matrix dipole element.

It is now convenient to define these expectation values through scalar and tensor polarizabilities in this way

$$-\frac{1}{4}\alpha_{scal}E^2 = \langle \gamma F | \mathcal{H}^{scal} | \gamma F \rangle \quad (1.128)$$

and

$$-\frac{1}{8}\alpha_{tens}(3E_z^2 - E^2) = \langle \gamma FF | \mathcal{H}^{tens} | \gamma FF \rangle \quad (1.129)$$

These definitions are given so that when the electric field is directed along z the polarizability of the $M = F$ stretched state is given by [48]

$$\Delta E^{(2)} = -\frac{1}{2\epsilon_0 c} \alpha I \quad (1.130)$$

where $I = \epsilon_0 c E^2 / 2$ represents the electric field intensity and where we have defined

$$\alpha = \alpha_{scal} + \alpha_{tens} . \quad (1.131)$$

In deriving these equations we have used the fact that

$$\{\mathbf{E}\mathbf{E}\}_0^2 = \frac{1}{\sqrt{6}}(3E_z^2 - E^2) \quad (1.132)$$

and the fact that, when $M = M'$, the only contribution in the sum in 1.126 is given by the $Q = 0$ term.

In our experiment there is always a magnetic field present that makes its contribution to the total Hamiltonian by a Zeeman term \mathcal{H}^z . In most cases this contribution is much larger than \mathcal{H}^s but still smaller than \mathcal{H}_0 , so that the correct course of action is to apply first order perturbation theory for \mathcal{H}^z . This removes the $(2F + 1)$ degeneracy of the ground state, and then apply our results for $\Delta E^{(2)}$ to the new ground state one gets.

The result is that the energy correction to the state $|\gamma F M\rangle$ can be written as

$$\Delta E^{(2)} = -\frac{1}{4}\alpha_{scal}E^2 - \frac{1}{8}\alpha_{tens}\frac{3M^2 - F(F+1)}{F(2F-1)}(3E_z^2 - E^2) \quad (1.133)$$

and we can see that, when $|M| = F$ in this formula, we get back the equations previously discussed.

By defining θ , like it's shown in figure 1.9, as the angle that the electric field \mathbf{E} makes with respect to the quantization axis z , we can rewrite the expression 1.133 as

$$\Delta E^{(2)} = -\frac{1}{2\epsilon_0 c} \left[\alpha_{scal} + \frac{3M^2 - F(F+1)}{F(2F-1)} \frac{3\cos^2(\theta) - 1}{2} \alpha_{tens} \right] I \quad (1.134)$$

or, for a stretched state, as

$$\Delta E^{(2)} = -\frac{1}{2\epsilon_0 c} \left[\alpha_{scal} + \frac{3\cos^2(\theta) - 1}{2} \alpha_{tens} \right] I . \quad (1.135)$$

It is often useful to write α_{scal} and α_{tens} in terms of reduced matrix elements, which are better suited for comparisons with experiments.

The appropriate expressions are found to be

$$\begin{aligned} \alpha_{scal} = & -\frac{1}{3(2F+1)} \sum_{(\gamma F)'} (-1)^{F'-F} |\langle \gamma F || \mathbf{D} || \gamma' F' \rangle|^2 \times \\ & \times \left(\frac{1}{\hbar\omega_{n0} - \hbar\omega + i\hbar\Gamma_n/2} + \frac{1}{\hbar\omega_{n0} + \hbar\omega + i\hbar\Gamma_n/2} \right) \end{aligned} \quad (1.136)$$

and

$$\begin{aligned} \alpha_{tens} = & -2\sqrt{\frac{5}{6}} \frac{\sqrt{F(2F-1)}}{\sqrt{(2F+3)(F+1)(2F+1)}} \sum_{(\gamma F)'} (-1)^{F'-F} \begin{Bmatrix} 1 & 1 & 2 \\ F & F & F' \end{Bmatrix} |\langle \gamma F || \mathbf{D} || \gamma' F' \rangle|^2 \times \\ & \times \left(\frac{1}{\hbar\omega_{n0} - \hbar\omega + i\hbar\Gamma_n/2} + \frac{1}{\hbar\omega_{n0} + \hbar\omega + i\hbar\Gamma_n/2} \right) \end{aligned} \quad (1.137)$$

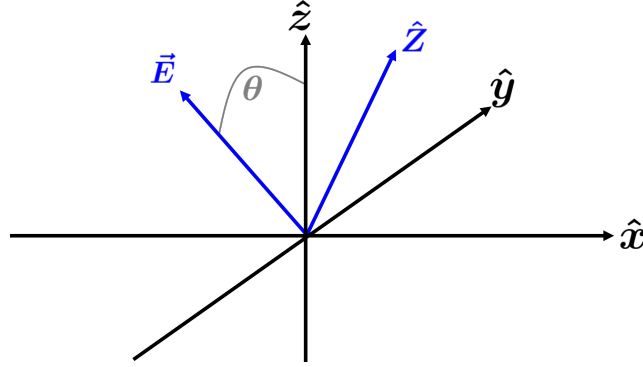


Figure 1.9: Definition of the angle θ that the electric field \vec{E} makes with the quantization axis z . In the picture, \hat{Z} represents the propagation direction of the laser that, in the experiment, generates the electric field.

where we have introduced the Wigner's 6j symbol $\left\{ \begin{smallmatrix} 1 & 1 & 2 \\ F & F' & F' \end{smallmatrix} \right\}$ and where we have shifted the energy levels ϵ_n by an imaginary term $i\hbar\Gamma_n/2$ to take into account the effect of spontaneous emission. Because of this shift the polarizabilities are now described by a real and an imaginary component.

The real component is what one should put inside the expression 1.135 for the energy correction of the ground state. The imaginary component is instead related to a photon scattering rate by the equation [49]

$$\Gamma_{scattering} = \frac{1}{\hbar\epsilon_0 c} \left[\text{Im}(\alpha_{scal}) + \frac{3 \cos^2(\theta) - 1}{2} \text{Im}(\alpha_{tens}) \right] I. \quad (1.138)$$

In the experiment the atoms interact with the electric field produced by a laser. This electric field will then not be spatially uniform.

If the intensity of the electric field varies slowly in a distance comparable with the atomic dimension, the results we got still hold and the energy correction $\Delta E^{(2)}$ now depends on the atomic center of mass position \mathbf{r} because $I \rightarrow I(\mathbf{r})$.

$\Delta E^{(2)}(\mathbf{r})$ can then be interpreted as an effective potential for the atom-light interaction that we write in the form

$$\mathcal{U}(\mathbf{r}) = -\frac{1}{2\epsilon_0 c} \left[\text{Re}(\alpha_{scal}) + \frac{3 \cos^2(\theta) - 1}{2} \text{Re}(\alpha_{tens}) \right] I(\mathbf{r}). \quad (1.139)$$

This expression can be rewritten in short as

$$\mathcal{U}(\mathbf{r}) = -\frac{1}{2\epsilon_0 c} \alpha(\theta, \omega) I(\mathbf{r}) \quad (1.140)$$

where we have defined the total polarizability $\alpha(\theta, \omega)$ as

$$\alpha(\theta, \omega) = \alpha_s(\omega) + \frac{3 \cos^2(\theta) - 1}{2} \alpha_t(\omega) \quad (1.141)$$

where $\alpha_s = \text{Re}[\alpha_{scal}]$ and $\alpha_t = \text{Re}[\alpha_{tens}]$.

We can now calculate the expression of the force felt by the atoms.

This force can be written as

$$\mathbf{F}(\mathbf{r}) = -\nabla\mathcal{U}(\mathbf{r}) = \frac{\alpha(\theta, \omega)}{2\epsilon_0 c} \nabla I(\mathbf{r}). \quad (1.142)$$

For the intensity, supposing we are working with a gaussian beam that is propagating in a general direction called Z (that should not be in principle the same z that defines the quantization axis, as shown in figure 1.9), we can use the standard expression found in [50] for $I(\mathbf{r})$:

$$I(\mathbf{r}) = \frac{2P}{\pi w^2(Z)} \exp\left(-\frac{2(X^2 + Y^2)}{w^2(Z)}\right) \quad (1.143)$$

where \hat{X}, \hat{Y} are unit vectors that together with \hat{Z} form a right-handed frame of reference, P is the average power of the laser,

$$w(Z) = w_0 \left[1 + \left(\frac{Z}{Z_R}\right)^2\right]^{1/2} \quad Z_R = \pi w_0^2 / \lambda. \quad (1.144)$$

We can now write the force in the X direction as:

$$F_X(\mathbf{r}) = -\frac{4P\alpha(\theta, \omega)}{\pi\epsilon_0 c w^4(Z)} X \exp\left(-\frac{2(X^2 + Y^2)}{w^2(Z)}\right). \quad (1.145)$$

This force reaches its maximum value when the atomic cloud is centered in $(X, Y, Z) = (w_0/2, 0, 0)$ and in this point the force takes the value:

$$F_X^{max} = -\frac{2P\alpha(\theta, \omega)}{\pi\sqrt{e}\epsilon_0 c w_0^3}. \quad (1.146)$$

1.6 Imaginary time evolution

Let's consider a quantum system described by the hamiltonian \mathcal{H} .

The time dependent Schrödinger equation that describes the time evolution of a wave function $\psi(\mathbf{r}, t)$ is given by:

$$i\hbar\partial_t\psi(\mathbf{r}, t) = \mathcal{H}\psi(\mathbf{r}, t). \quad (1.147)$$

We can now make the substitution $\tau = it/\hbar \Rightarrow \partial_\tau = -i\hbar\partial_t$ inside the Schrödinger equation and get [51]

$$\partial_\tau\psi(\mathbf{r}, \tau) = -\mathcal{H}\psi(\mathbf{r}, \tau). \quad (1.148)$$

If we consider t to be an "Imaginary time", then τ will be real and 1.148 represents the Schrödinger equation written in imaginary time.

The formal solution of 1.148 is given by

$$\psi(\mathbf{r}, \tau) = e^{-\mathcal{H}\tau}\psi(\mathbf{r}, 0) \quad (1.149)$$

and by recalling that the equilibrium Boltzmann distribution is given by $\exp(-\mathcal{H}/k_B T)$ where k_B represents the Boltzmann constant and T is the temperature, we can interpret τ to be an inverse of a temperature.

Increasing the imaginary time will therefore be equivalent to lowering the temperature. Let's now suppose that we know the eigenstates of \mathcal{H} , which are the time-independent functions $\psi_n(\mathbf{r})$ that satisfy

$$\mathcal{H}\psi_n(\mathbf{r}) = E_n\psi_n(\mathbf{r}) \quad (1.150)$$

where E_n represents the energy eigenvalue of the state ψ_n .

$\{\psi_n(\mathbf{r})\}$ represents a complete base of functions and we can then decompose the general solution $\psi(\mathbf{r}, \tau)$ of the imaginary time Schrödinger equation in the following way:

$$\begin{aligned} \psi(\mathbf{r}, \tau) &= \sum_n c_n \psi_n(\mathbf{r}) \exp(-E_n \tau) = \\ &= c_0 \psi_0(\mathbf{r}) + \sum_{n \neq 0} \psi_n(\mathbf{r}) \exp(-E_n \tau) \end{aligned} \quad (1.151)$$

where the sum runs over all the eigenstates of \mathcal{H} and in the last term we fixed the energy of the ground state $E_0 \equiv 0$.

The only time dependence in this expression comes from the exponential factor $\exp(-E_n \tau)$, from which we can see that the contribution to $\psi_n(\mathbf{r}, \tau)$ given by the n -th eigenstate decays exponentially with respect to the ground state one.

Because of this argument we can say that, after a sufficiently long "Time", the only contribution left to the state $\psi(\mathbf{r}, \tau)$ will be given by the ground state, if the initial wave function had some nonzero contribution given by the ground state:

$$\psi(\mathbf{r}, \tau \rightarrow \infty) \rightarrow c_0 \psi_0(\mathbf{r}) . \quad (1.152)$$

In this limit, the ground state $n = 0$ is projected out of the initial trial function. Therefore, by evolving the system in this "Imaginary time", we can obtain the ground state of the hamiltonian \mathcal{H} .

Creation of arbitrary potential patterns using a DMD

This chapter is dedicated to the characterization of a digital micromirror device (DMD), which is a reflective spatial light modulator that can be used to modulate the amplitude of an incoming light beam, and to the realization of arbitrary potential patterns made thanks to it.

The first section of this chapter is dedicated to the explanation of the working principle of the DMD as well as to the description of its properties as a diffraction grating.

In the second section I describe the two optical setups devised for the characterization of the DMD, describing the optical path's critical points. Since the DMD only allows for a spatial modulation of light, any preexisting shape of the impinging intensity profile remains superimposed with the DMD's modulation. I therefore realized in Mathematica a feedback mechanism to realize homogeneous light patterns. Section three is dedicated to the explanation of this feedback process.

In the last section I show some simulations made for the superfluid and supersolid formed inside the experimentally realized ring light. This simulations are a good test to check if we were able to realize an optical setup free from aberrations.

2.1 The Digital Micromirror Device

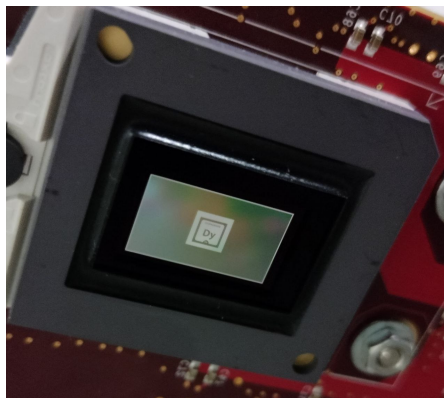


Figure 2.1: A picture of the DMD with the dysprosium chemical symbol displayed on it.

The Digital Micromirror Device is a reflecting spatial light modulator that controls the

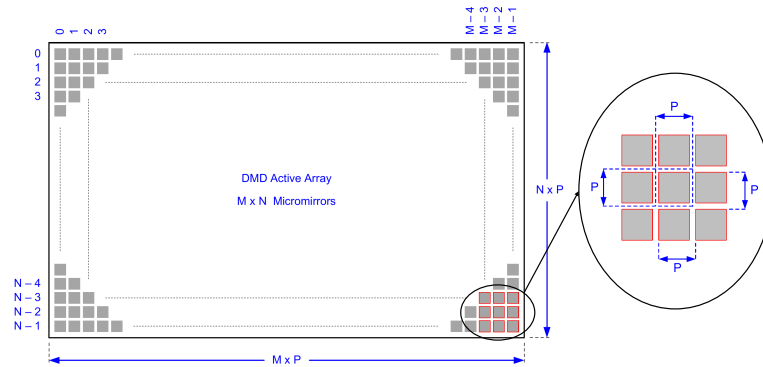


Figure 2.2: Scheme of the DMD's micromirror array. $P = 7.56 \mu\text{m}$ represents the pixel size of the array. $N \times M = 1080 \times 1920$ represents the array's dimensions in pixels. Figure taken from [52].

amplitude of an incoming light beam. A picture of the DMD board is shown in figure 2.1. The one used in this thesis work is the "DLP65000 0.65 1080p MVSP Type A" by Texas Instruments [52]. This DMD is composed by an array of 1080×1920 squared micromirrors. A pixel of the DMD has its linear dimension d equal to $7.56 \mu\text{m}$. In figure 2.2 is shown a scheme of this array.

Each one of these micromirrors can turn along his diagonal axis by $\pm 12^\circ$, as shown in figure 2.3, with a switching time of around $1 \mu\text{s}$. The status of each micromirror is then binary and can be controlled by a computer software given by the manufacturing company. By inputting on the software a black and white .bmp image (meaning that the entries of the matrix forming the image should be only zeros and ones) that has the same dimensions as the DMD board itself, this image will be displayed on the DMD board and can then be

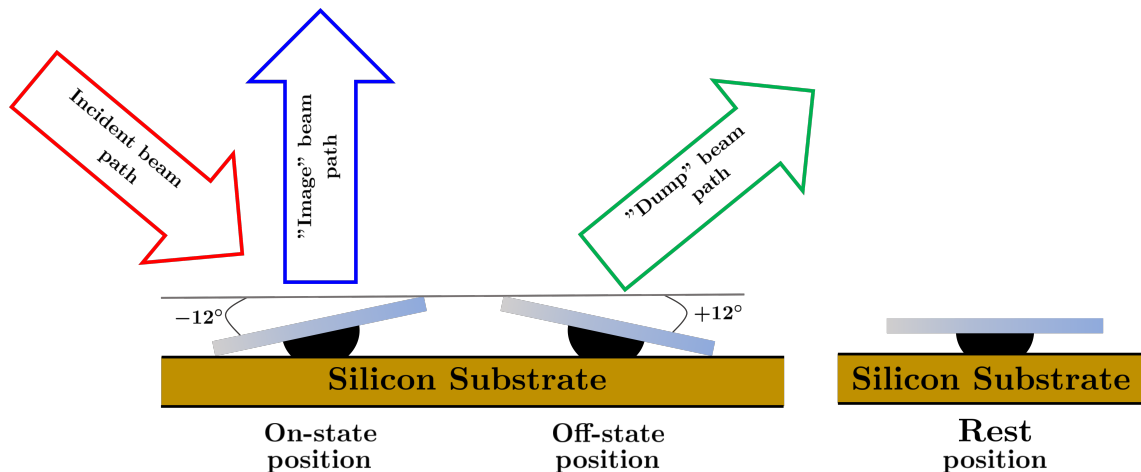


Figure 2.3: Sketch of the light impinging on the DMD and of the three possible positions for the micromirrors. When the DMD is switched off all the mirrors get aligned in the parked position, also called rest position. When the DMD is switched on the micromirrors can only assume the On or Off state positions.

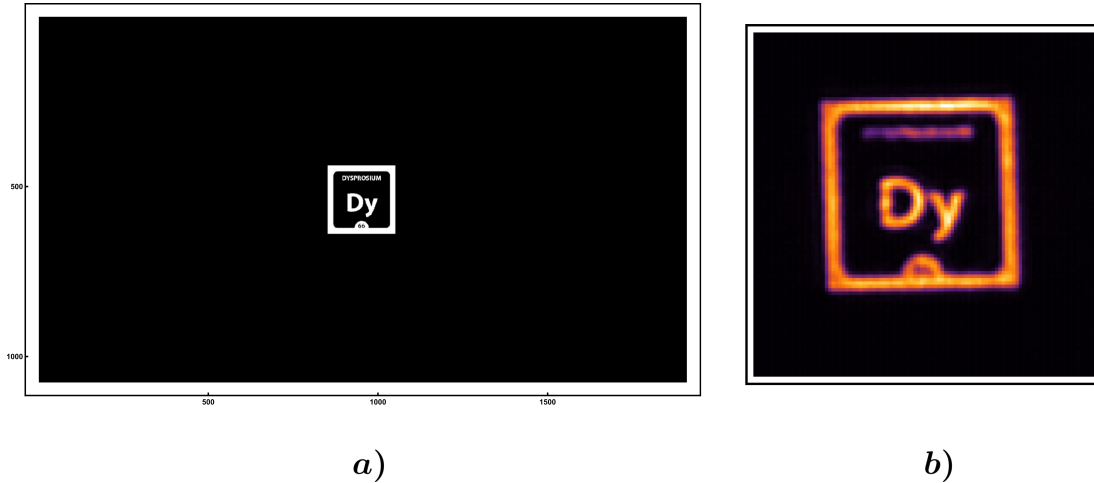


Figure 2.4: Example of a pattern sent to the DMD program and resulting imprint on the outgoing beam. (a) Pattern sent to the DMD. (b) Recorded image of the spatial profile of the outgoing beam from the DMD after a 5× demagnification.

casted inside the light impinging on the DMD. This is done by assigning every entry of the matrix with its corresponding pixel. If a pixel is in the 0 (Off) state it means that the corresponding micromirror will be tilted in one way, whereas if the pixel is in the 1 (On) state the micromirror will be tilted 24 degrees in the other direction.

If one only thinks about ray optics, the result of the different tilting of the mirrors will produce 2 different outgoing beams. One that is called “Dump” beam, that is the one generated by the mirrors tilted in the Off state, and one beam called the “Image” beam, generated by the On state mirrors.

This creates the imprinting of the image sent to the DMD inside the “Image” beam, whereas the “Dump” beam contains a negative of this image.

When the DMD gets switched off, all the micromirrors get set to the so called “Rest” position, that is parallel with respect to the substrate lying underneath them.

In figure 2.4 is shown an example of the formation of a 2D image inside a light beam made by sending a specific pattern to the DMD.

The DMD, thanks to the periodic pattern made by its pixels in both its array’s dimensions, also acts as a two dimensional diffraction grating, showing multiple outgoing diffraction orders. Since in our experimental setup we only work with a single one of these orders, this diffraction results in a source of power loss with respect to the incoming light beam. In general, when working with a diffraction grating, a wavelength λ is diffracted into the m -th order of diffraction at an angle that follows this simple equation:

$$m \frac{\lambda}{d} = \sin \theta - \sin \theta_0 \quad (2.1)$$

where the angles are defined in figure 2.5.

Since the micromirrors are tilted with respect to the substrate, the DMD actually acts as a blazed diffraction grating, with blazing angle given by $\varphi = 12^\circ$.

Because of this, one can search for the blazing condition for the DMD, that is, the condition in which a specific diffraction order gets most of the reflected power.

To get the equation defining this condition, one starts from the two equations that describe a blazed grating. These equations are the following [53]:

$$\begin{aligned} m \frac{\lambda}{d} &= \sin \theta - \sin \theta_0 \\ 0 &= \sin(\theta - \varphi) - \sin(\theta_0 + \varphi) . \end{aligned} \quad (2.2)$$

Normally for a grating, these equations are solved to find the blazing angle φ that maximizes the power into the $m = 1$ diffraction order for a specific wavelength and a specific incident angle.

In the case of the DMD, $\varphi = 12^\circ$ is fixed by the micromirrors' geometry and one instead can find if there are some diffraction orders that fulfill the blazing condition.

From the second of the two equations written in 2.2 one finds the condition

$$\theta = \theta_0 + 2\varphi \quad (2.3)$$

which is telling the simple fact that the peak of the intensity distribution will be at the angle that represents the reflection from the single micromirror.

Inserting 2.3 inside 2.2 we get the following equation

$$\mathcal{F}_m(\theta_0) = 0 \quad (2.4)$$

where we have defined

$$\mathcal{F}_m(\theta_0) = \arcsin\left(m \frac{\lambda}{d} + \sin \theta_0\right) - \theta_0 - 2\varphi . \quad (2.5)$$

This is the equation that gives out the blazed diffraction order as a function of the incident angle θ_0 .

In figure 2.6 is shown a plot of $\mathcal{F}_m(\theta_0)$ for various orders of diffraction.

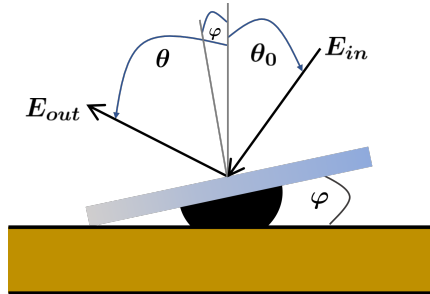


Figure 2.5: Definition of the angles used in the text for the diffraction of the DMD. θ_0 represents the angle at which light hits the normal to the substrate of the DMD whereas θ represents the angle at which light is diffracted. φ represents the angle made by the normal of the micromirror with respect to the normal of the substrate and is equal to 12 degrees.

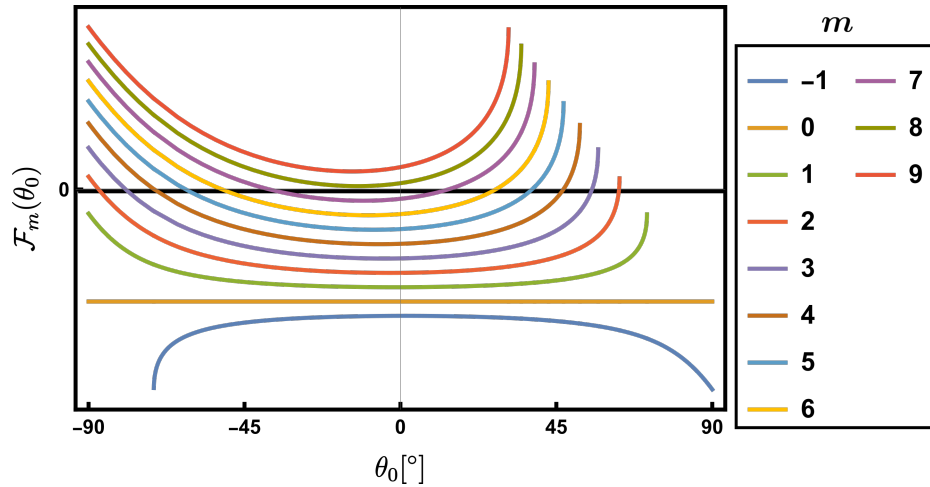


Figure 2.6: Sketch of the function $\mathcal{F}_m(\theta_0)$ as a function of θ_0 for different diffraction orders m . When $\mathcal{F}_m(\theta_0) = 0$ the m -th order is the most intense one if the incoming light hits the DMD at the angle θ_0 . The various curves are drawn for $\lambda = 405$ nm and $d = 7.56 \cos(12^\circ)$ μm .

As one can see from the picture, at different incident angles will correspond different blazed diffraction orders.

In particular it's interesting to notice that, since $\varphi = 12^\circ$ is constant, the 0-th order of the grating, the one that does not disperse different wavelengths at different angles, will never achieve blazing.

2.2 Optical Setup to study the DMD

Both the optical setups described in this section feature a demagnification part where the image that is projected onto the DMD gets reduced in size through a microscope and is then observed on a CCD camera. Demagnifying the image through the microscope is important for two reasons. The first one being the fact that, when the DMD will be placed in the actual experiment to make real potentials for the atoms, in the optical setup we will implement a 2 stage demagnification process to make potentials that have sizes comparable to the Bose-Einstein condensate and to the supersolid. The second reason as to why it's important to demagnify is the fact that in this way a certain number of pixels of the DMD will be mapped to the same camera pixel. This brings out the possibility of making gray scaled images on the camera by starting just with a black and white image on the DMD.

2.2.1 First optical setup

In figure 2.7 is shown the first optical setup realized to study the DMD.

The laser source of this first apparatus is a 405 nm diode laser.

This laser is coupled inside a single mode fiber to make the resulting beam a TEM_{00} mode. Then the light passes through a $\lambda/2$ waveplate that rotates its polarization. This is done

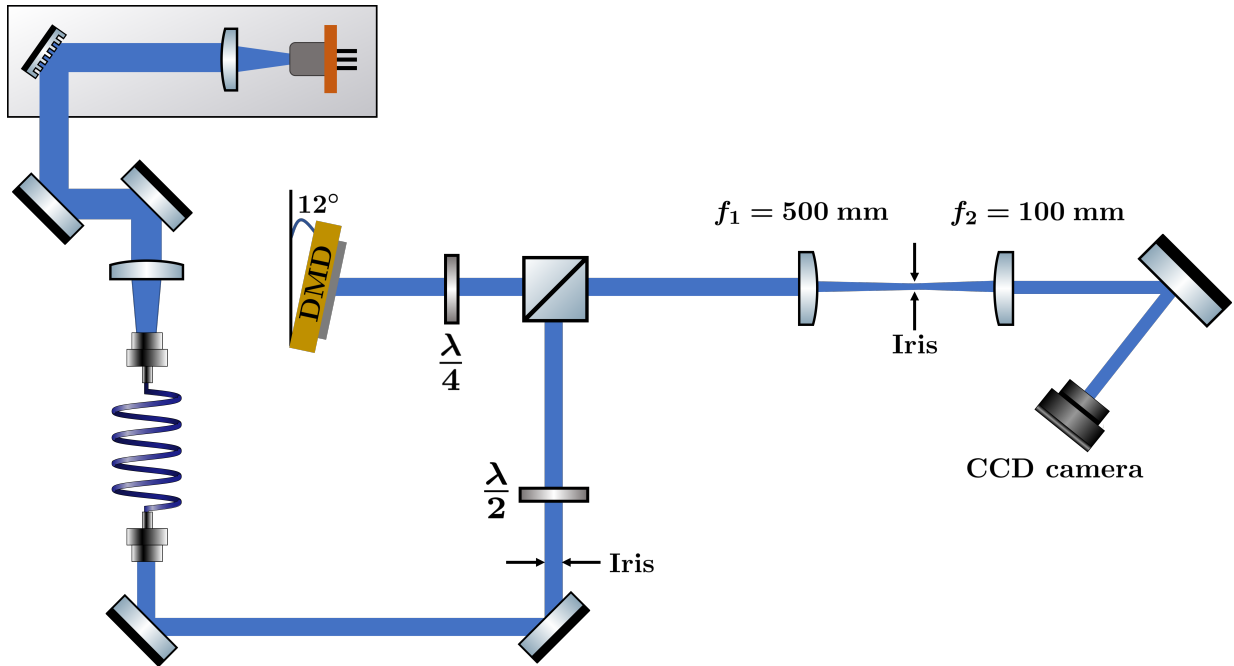


Figure 2.7: Sketch of the first experimental setup devised to study the DMD. This represents a compact scheme to use the DMD that has the downside of having to place the board at a 12 degree angle with respect to the impinging beam.

so that when the light will pass through a polarizing beam splitter (PBS), we can have control on how much power gets reflected in the direction of the DMD.

The light then hits the DMD and the outgoing beam will then have imprinted inside the spatial profile of the DMD. The DMD is tilted by 12 degrees with respect to the incoming beam so that the reflected light is parallel to the incoming one. The beam then goes back inside the PBS, and this time it is transmitted thanks to the double pass through the $\lambda/4$ waveplate.

After the cube we place 2 lenses, the first one has focal length f_1 equal to 500 mm and the second one has $f_2 = 100$ mm. The first lens is placed at a distance of 500 mm from the DMD whereas the second is placed at a distance of 100 mm from the camera. We don't need to worry about placing an iris before the first lens to select only one diffraction order because the spatial separation between 2 orders on the first lens is equal to $f_1\lambda/d \approx 27$ mm and this is greater than the 25 mm diameter of the first lens.

This 2 lenses are placed at a relative distance of $f_1 + f_2$ to make a microscope for the image (this same lenses configuration also acts as a telescope for the collimated beam). This microscope magnifies the image imprinted on the DMD by a factor of $f_2/f_1 = 0.2$, which means that the resulting image on the CCD camera will be 5 times smaller than the one imprinted on the DMD. An iris is placed in the focal plane inside the microscope. Since the first lens of the microscope makes the Fourier transform of the image [53], placing an iris in this point acts as a bandpass filter, cutting the high frequency components of the Fourier transform of the image and making it less detailed when its transformed back by

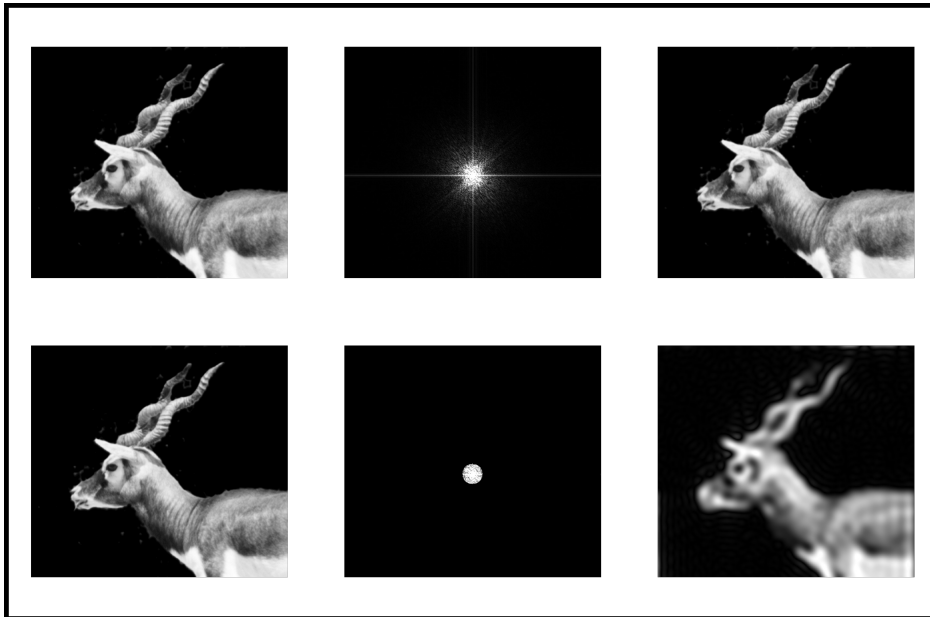


Figure 2.8: Demonstration of how an high frequency cut in the Fourier space leads to blurred images when transforming back to real space. In the first row it's shown an image of a blackbuck, to its right I've plotted the absolute value of its Fourier transform and again on the right its shown the inverse Fourier transform, that is equal to the starting picture. In the second row the same is shown, but now in the Fourier space there is applied the band-pass filter that blocks high frequency components of the image. We can see that when we now revert back to real space the image is less detailed and more blurry.

the second lens. An example of how an high frequency cut leads to less detailed images is shown in figure 2.8.

As one can see from figure 2.1, the DMD is placed at a 45 degree angle with respect to the optical table. This is done so that the on and off states for the micromirrors will send light parallel to the table. Because of this if the CCD camera was placed parallel to the table, one would see in the camera images that are rotated by 45 degrees. To try and correct this we also place the camera in an inclined position. In section 2.3 we will see that this experimental correction is not enough to get completely straight images and a second stage of rotation, this time through software, needs to be implemented.

2.2.2 Second optical setup

By making ground state simulations for both the superfluid and the supersolid trapped inside the rings that we were able to produce with the first optical setup (see section 2.4) we understood that what's really important to get a cylindrically symmetric solution of the Gross-Pitavskii equation is to have little to no aberrations inside the ring. This is because we are working with a repulsive ring and the atoms actually fill out the space where there is no light, meaning that the atoms are not sensitive in fluctuations of the potentials that happen in places were their wavefunctions are almost zero.

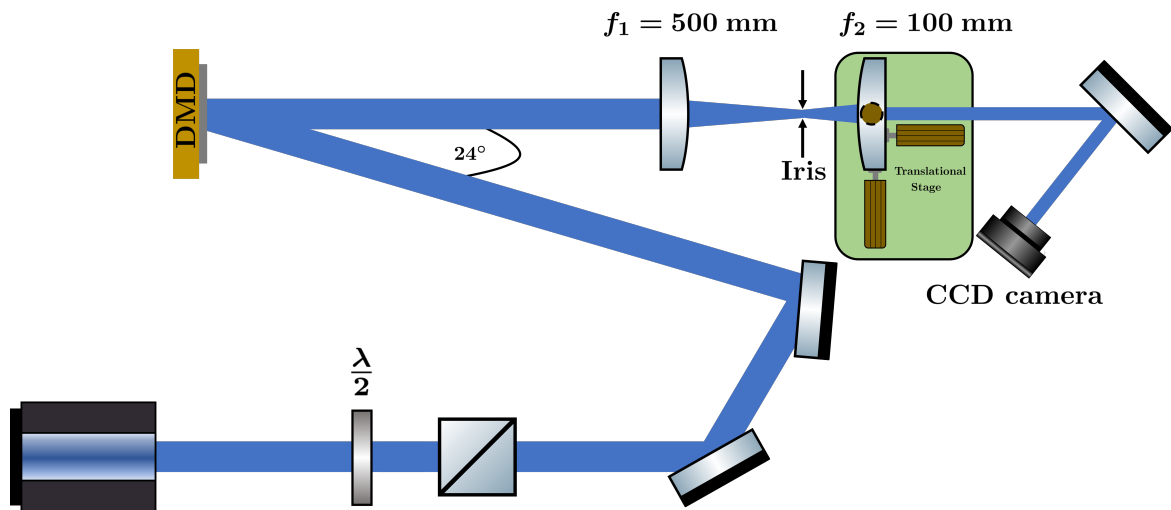


Figure 2.9: Sketch of the second experimental setup used to study the DMD. The DMD is now placed at a right angle with respect to the impinging beam.

These aberrations can be caused by a non perfect alignment of the optical path and they can cause some light to come inside the ring and break the symmetry of the system.

Other aberrations, such as astigmatism in the recorded ring on the camera, can also cause the breaking of cylindrical symmetry because they make the ring oval shaped.

To correct these imperfections we realize a second optical setup for the DMD, which is shown in figure 2.9. In this new optical setup the laser source is different from the one employed in the scheme shown in figure 2.7 but this is not important since the setup is used to study the DMD and not the laser.

We now have the DMD with no tilt whatsoever, and to make the beam come out straight from it we now impinge on the board with a 24 degrees angle. This correction is made so that all the ring imprinted on the beam will hit the camera simultaneously, whereas before, since the DMD was tilted by 12 degrees and the camera was not, this was generating an astigmatic image on the camera.

We now also remove the rotation of the camera by 45 degrees. In this way it is much easier to properly align the camera. The rotation of the recorded images is then completely done by software.

We also introduce a translational stage on the second lens. This makes it possible to align the lens with extreme precision and in this way we minimize all the possible sources of aberrations.

2.3 Feedback procedure

Let's suppose that one feeds to the DMD a flat top image. Because of the gaussian spatial profile of the beam, the resulting image recorded on a camera placed after the DMD will show the flat top but with an intensity distribution that is still the one of the laser, that is, a gaussian distribution. This is shown in figure 2.10.

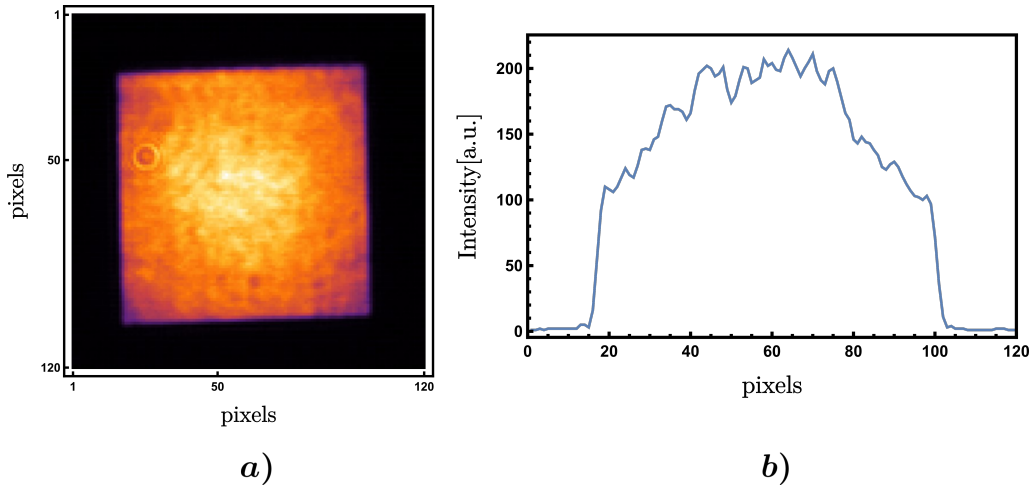


Figure 2.10: (a) Recorded image of the flat top with no correction on the camera. (b) Cut of the intensity distribution along the flat top.

To solve this problem I created a Mathematica program that, through a feedback process, can make the potential more homogeneous.

Since the DMD has to be rotated at a 45 degree angle with respect to the optical table, as one can see from figure 2.10, the recorded image on the camera will be tilted with respect to the image imprinted on the DMD. This can be corrected to first approximation by also tilting the camera, but cannot be completely corrected in this way. Also, since in the optical path going from the DMD to the camera is placed a magnification system, the recorded image on the camera cannot be directly compared with the one displayed in the DMD since they have different dimensions.

The first part of the feedback program is then a calibration, where one measures the rotation angle and the scaling of the image, with respect to the DMD one.

This is done by displaying in the DMD an image consisting of three dots that form two perpendicular lines. This image is shown in figure 2.11.

By recording the resulting image on the camera, it's possible to extract both the rotation angle and the scaling factor.

Thanks to this parameters one can take the image on the CCD camera and make an affine transformation into an image that is comparable with what is sent to the DMD, as is shown in figure 2.12.

Once the calibration process is completed the real feedback can start.

The feedback starts by applying the affine transformation on the acquired image on the CCD, and comparing it to the target image. This comparison results in an error matrix that can be used to correct the image sent to the DMD and the whole process starts again by acquiring a new image on the camera.

In mathematical formulas, at the n -th iteration the error matrix \mathcal{E}_n is defined by the difference between the target image \mathcal{T} and the transformed image acquired by the camera, that we call \mathcal{C}_n

$$\mathcal{E}_n = \mathcal{T} - \mathcal{C}_n . \quad (2.6)$$

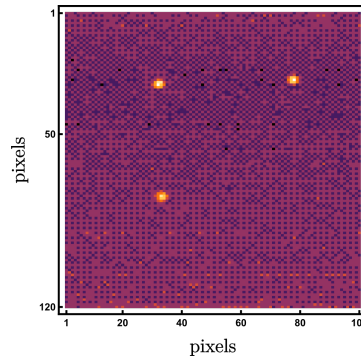


Figure 2.11: Calibration image captured by the CCD camera. This image is used to get the rotation angle and magnification.

By using the matrix \mathcal{E}_n , we can write the image that gets sent to the DMD in the next iteration in this way

$$\mathcal{D}_{n+1} = \mathcal{D}_n + \kappa_p \mathcal{E}_n \quad (2.7)$$

where we have defined \mathcal{D}_n as the image that gets sent to the DMD in the n -th iteration and where κ_p represents a gain coefficient that needs to be adjusted to get the best correction in the least amount of iteration steps. In our case we got the best results with $\kappa_p = 0.2$. Since the DMD can only read images containing 0s and 1s (black and white images), before sending \mathcal{D}_n to the DMD, one needs to apply a dithering algorithm to it, to make it black and white.

The dithering algorithm we use is the Floyd-Steinberg one [54], given in mathematical

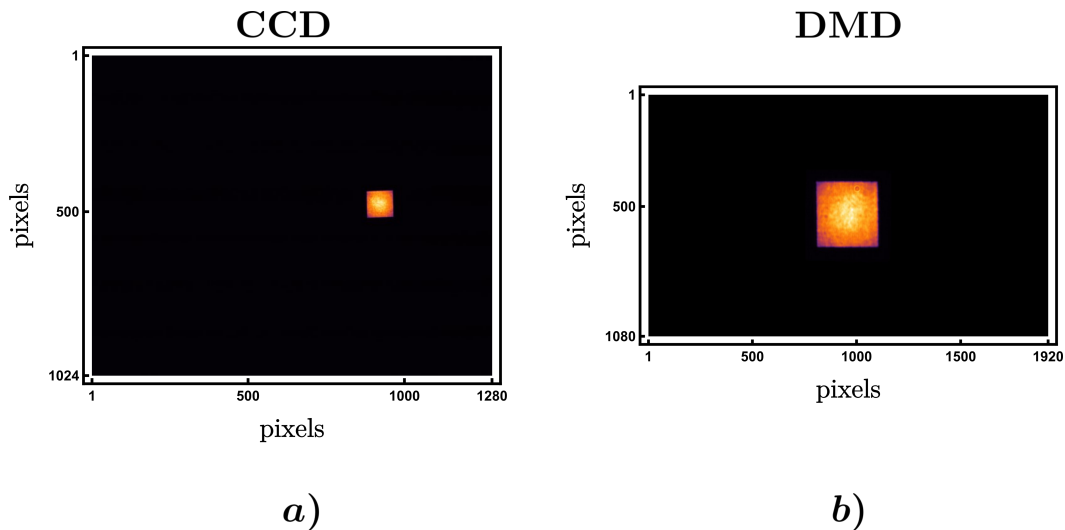


Figure 2.12: (a) Image of the flat top recorded in the CCD camera. (b) Image of the flat top in the DMD dimensions after the affine transformation.

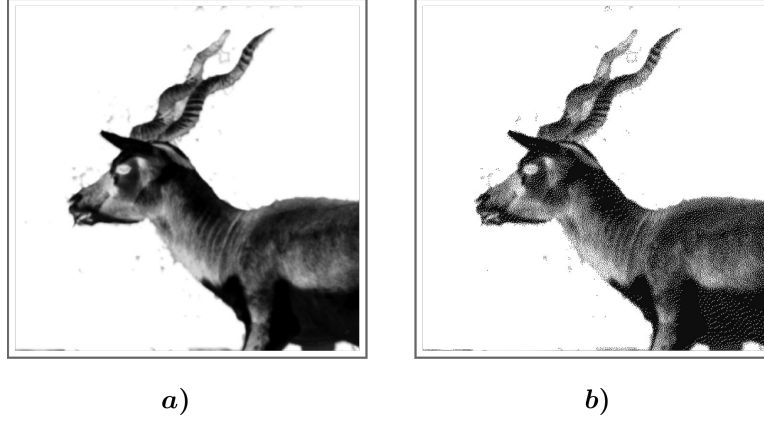


Figure 2.13: Results of the Floyd-Steinberg algorithm on a black buck image. (a) Image to be dithered. (b) Dithered image. As it's visible in the bottom right corner of (b), this algorithm collects all the dithering error on this corner of the image. This is fine in our case since this corner of the DMD is usually not utilized.

terms by

$$\begin{pmatrix} \tilde{\mathcal{D}}_{i-1,j-1} & \tilde{\mathcal{D}}_{i-1,j} & \tilde{\mathcal{D}}_{i-1,j+1} \\ \tilde{\mathcal{D}}_{i,j-1} & \tilde{\mathcal{D}}_{i,j} & \tilde{\mathcal{D}}_{i,j+1} \\ \tilde{\mathcal{D}}_{i+1,j-1} & \tilde{\mathcal{D}}_{i+1,j} & \tilde{\mathcal{D}}_{i+1,j+1} \end{pmatrix} = \begin{pmatrix} \tilde{\mathcal{D}}_{i-1,j-1} & \tilde{\mathcal{D}}_{i-1,j} & \tilde{\mathcal{D}}_{i-1,j+1} \\ \tilde{\mathcal{D}}_{i,j-1} & \tilde{\mathcal{D}}_{i,j} & \tilde{\mathcal{D}}_{i,j+1} \\ \tilde{\mathcal{D}}_{i+1,j-1} & \tilde{\mathcal{D}}_{i+1,j} & \tilde{\mathcal{D}}_{i+1,j+1} \end{pmatrix} + \begin{pmatrix} 0 & 0 & 0 \\ 0 & 0 & 7/16 \\ 3/16 & 5/16 & 1/16 \end{pmatrix} \Delta \tilde{\mathcal{D}}_{i,j} \quad (2.8)$$

where we have defined the matrix $\tilde{\mathcal{D}} = \mathcal{D}/\max[\mathcal{D}]$, $\tilde{\mathcal{D}}_{i,j}$ represents the (i,j) -th element of the matrix and

$$\Delta \tilde{\mathcal{D}}_{i,j} = \tilde{\mathcal{D}}_{i,j} - \text{Round}[\tilde{\mathcal{D}}_{i,j}] \quad (2.9)$$

represents the error one makes by rounding $\tilde{\mathcal{D}}_{i,j}$ to the closest integer.

In figure 2.13 it's shown a result of the algorithm on a deer image.

The feedback process described above is analogous to what happens in a PI controller. In fact, even though it was not implemented in our case, one can even introduce an integral correction by writing

$$\mathcal{D}_{n+1} = \mathcal{D}_n + \kappa_n \mathcal{E}_n + \kappa_i \sum_{m=0}^n \mathcal{E}_m . \quad (2.10)$$

At each point of the iteration it's possible to quantify the discrepancy between the target and the obtained image thanks to the error \mathcal{R} defined by the following equation:

$$\mathcal{R} = 100 \left[\sum_{i,j} \left(\frac{\mathcal{D}_{i,j} - \mathcal{T}_{i,j}}{\mathcal{T}_{i,j}} \right)^2 \frac{1}{\mathcal{A}} \right]^{1/2} \quad (2.11)$$

where $\mathcal{A} = 1080 \times 1920$ represents the DMD area in pixels.

The results for the correction of a flat top are shown in figure 2.14.

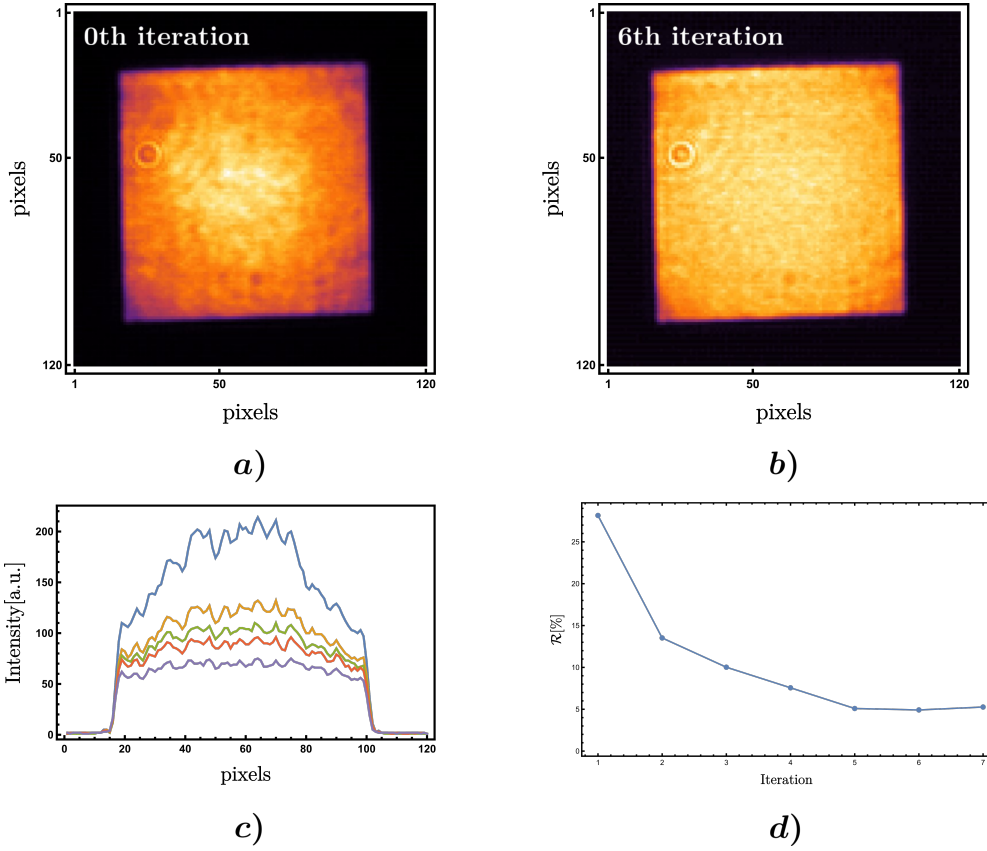


Figure 2.14: Results for the correction of a flat top. (a) Recorded flat top on the CCD camera without any correction. The gaussian profile of the beam is clearly visible inside the flat top. (b) Flat top at the sixth iteration of the correction feedback. (c) Intensity distribution along a horizontal cut on the flat top for different iterations. (d) Error function \mathcal{R} shown as a function of the iterations.

In the figure we can see that the intensity distribution is much more uniform after the feedback program.

This same feedback algorithm can be implemented other types of 2D potentials, such as rings or gradients.

2.4 Simulations

We use the imaginary time evolution method explained in section 1.6 to find the ground state of the extended Gross-Pitaevskii hamiltonian:¹

$$\mathcal{H} = \left(-\frac{\hbar^2 \nabla^2}{2m} + V_{h.o.}(\mathbf{r}) + V_{ring}(x, y) + g|\psi(\mathbf{r}, \tau)|^2 + V_{dd}^{mf}(\mathbf{r}, \tau) + \gamma(\epsilon_{dd})|\psi(\mathbf{r}, \tau)|^3 \right) \quad (2.12)$$

¹The order parameter ψ in this equation needs to be normalized to the total number of atoms N by writing $\int |\psi|^2 d\vec{r} = N$.

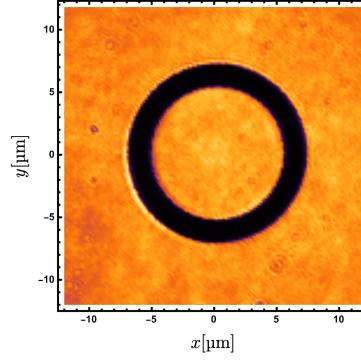


Figure 2.15: Ring potential used in the simulations.

where $V_{h.o.}(\mathbf{r})$ represents an harmonic confining term

$$V_{h.o.}(\mathbf{r}) = \frac{1}{2}M(\omega_x^2x^2 + \omega_y^2y^2 + \omega_z^2z^2) \quad (2.13)$$

$g = 4\pi\hbar^2a_s/m$ represents the strength of the contact interaction, a_s being the s -wave scattering length. $\Phi_{dd}(\mathbf{r}, \tau)$ represents the mean field contribution given by equation 1.41 and the beyond mean field term $\gamma(\epsilon_{dd})|\psi(\mathbf{r}, \tau)|^3$ is inserted to study the onset of supersolidity in the system. $\gamma(\epsilon_{dd})$ is defined in 1.52. Lastly, inside equation 2.12 the term $V_{ring}(x, y)$ represents the 2D confining ring experimentally generated through the use of the DMD. In figure 2.15 is shown a figure of the ring potential used as V_{ring} . This is just a recorded picture of the DMD ring acquired on the camera shown in figure 2.9 after a feedback loop. Since the ring will have a radius of 5 μm in the atomic plane, the image's dimensions are adjusted to make it this size. Moreover, the intensity of the image, that in the camera is a 8-bit number, is converted in an energy, to make the ring potential have an average height of about 200 nK.

The simulations are done to see if the experimentally achieved rings are free enough from defects and aberrations to make the superfluid delocalize inside the ring and to see the second order transition happen inside this annular potential.

The simulations are done with a total atom number $N = 50 \times 10^3$ and an harmonic potential characterized by $(\omega_x, \omega_y, \omega_z) = (20, 20, 100)$ Hz. This potential is inserted mainly to trap the atoms in the z direction and in the experiment will be realized through an optical light sheet made by a green laser.

The simulations are done at different scattering lengths across the superfluid to supersolid quantum phase transition. In figure 2.16 the results of various simulations made for different scattering length are shown.

As one can see from this simulations, even though we are working in the second setup shown in figure 2.9 to free the ring from aberrations and we made the feedback loop on the ring, we get a superfluid ground state that, even though it's completely delocalized inside the ring, still shows some non uniformity.

This lack of homogeneity of the superfluid is translated in a supersolid that does not show a perfect periodic lattice structure.

Leaving aside these problems, the simulations are telling us that the potentials we are

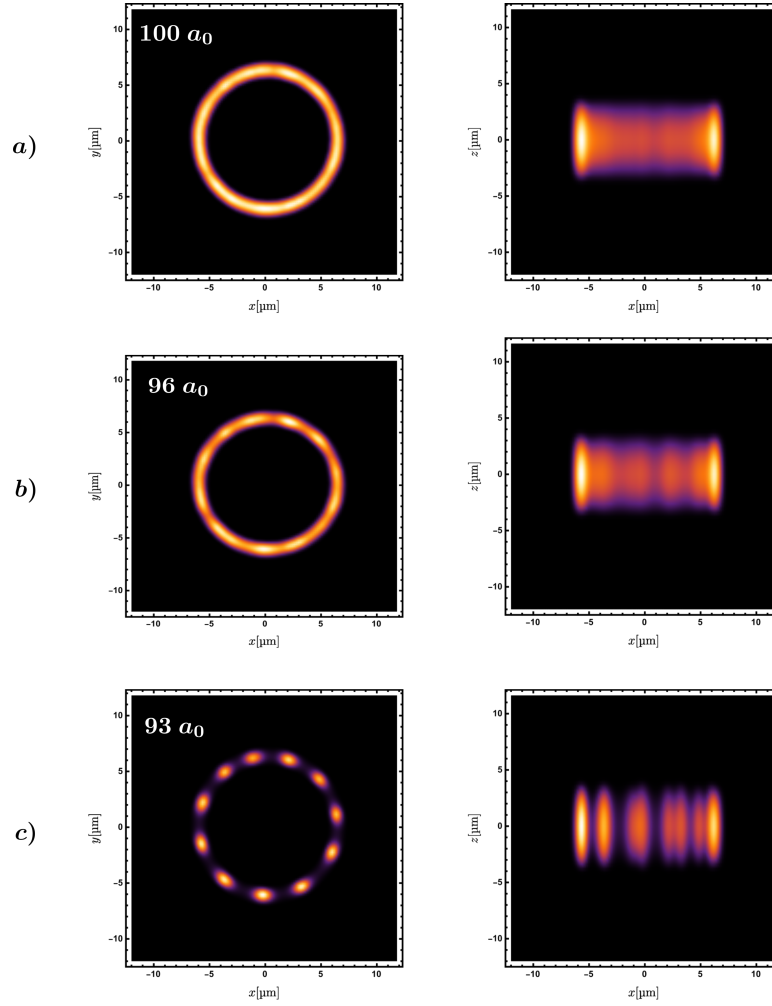


Figure 2.16: Results of the simulations made. (a) At $a_s = 100a_0$ which is still in the superfluid phase. (b) At $a_s = 96a_0$ the supersolid droplets start to form. (c) When $a_s = 93a_0$ the droplets are completely formed.

simulating are good enough to see the formation of the supersolid and the delocalization of the superfluid. Of course, when we will project the ring on top of the atoms, the value for the potential barriers that we will be able to realize will be determined by the laser intensity and by the atoms polarizability through the formula for the potential reported in 1.140.

In the next chapter I will report on our experimental measurements of the dynamical polarizability of dysprosium. Measurements that were made to give an estimate on the potentials we will be able to project on the atoms.

Characterization of a blue light source for optical trapping of dysprosium atoms

In the first part of this third chapter I present the work done to realize and characterize a source of tunable blue light working at around 404 nm with a gaussian spatial mode profile. This blue light will be implemented in the experiment to realize repulsive potentials for dysprosium. Working with this particular wavelength will be nice because, since the resolution of images scales linearly with the wavelength, working with shorter wavelengths will result in a better resolution for our potentials. In this regard 404 nm is almost as low as one can go before needing to use extremely specific lasers and optics.

Since dysprosium has a strong absorption line at 404.7 nm, that is extremely close to our working wavelength, the optical setups implemented were realized with the intent of narrowing down the laser spectrum, to make it not cross the transition.

In the second part of the chapter I present our experimental results for the measurement of the dynamical polarizability of dysprosium around 404 nm. A measurement of this quantity is important because the polarizability of dysprosium has never been studied at this particular wavelength before and having access to this number is fundamental for us because it relates to the height of the potentials that the atoms will feel when trapped inside our light.

In the third part of the chapter I also present our implementation of a Master-Amplifier injection lock configuration, made to have more blue light power to work with. The master laser for this setup is the one characterized in the first part of the chapter, whereas the amplifier is a second diode laser.

At the end of the chapter I summarize the measurements made to calibrate the magnification of an imaging optical system needed to give an estimate of the 404 nm laser waist in the atomic plane.

All the work relating to this chapter was done in the dysprosium lab in Pisa. When I joined the group the experiment was already able to produce the degenerate Bose gas of ^{162}Dy . Details on the experimental apparatus and sequence can be found in [18, 55, 56].

3.1 Repulsive light implemented in the experiment

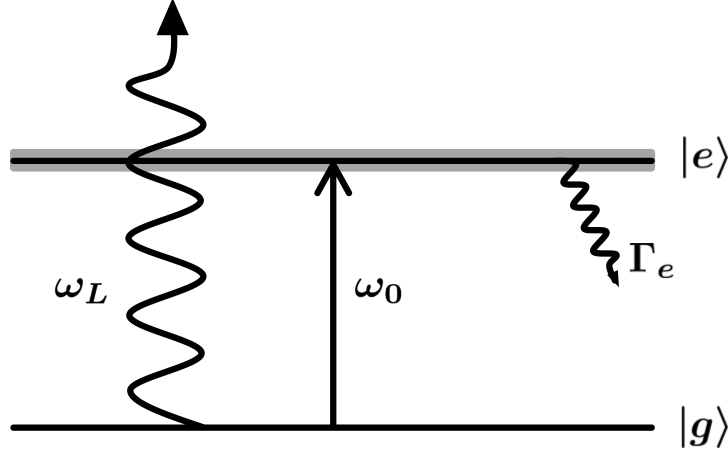


Figure 3.1: Representation of a two level system with transition frequency ω_0 interacting with an electric field oscillating with frequency ω_L . $|g\rangle$ represents the ground state and $|e\rangle$ the excited one. The atomic line is broadened by the spontaneous emission which occurs with a rate Γ_e .

We want to work with a laser that generates a repulsive potential for dysprosium which means, in a simplified picture where we consider the Dy atom as a two-level system, that the emission frequency ω_L of the laser should be larger than the transition frequency of our two level system, that we call ω_0 , as shown schematically in figure 3.1.

The same argument can be written in terms of wavelengths using the relationship $\lambda = 2\pi c/\omega$ where c represents the speed of light. Of course, since wavelengths are inversely proportional to frequencies, the requirement is that the laser wavelength λ_L should be less than the transition one, λ_0 .

The first repulsive light source used in the experiment is a *Nichia NDV4313* [57] diode laser which is a continuous wave multimode laser capable of outputting up to 120 mW of power at around 405 nm. The emission wavelength of this light source is extremely close to that of a Dysprosium absorption transition, which is the $[\text{Xe}]4f^{10}6s^2(^5I_8) \rightarrow [\text{Xe}]4f^{10}(^5I_8)6s6p(^1P_1^o)(8,1)_7$. This is a strong dipole-permitted transition with $\lambda_0 = 404.7$ nm and $\Gamma_e/2\pi \approx 30$ MHz [58]. In figure 3.2 are shown the three strong absorption transition for Dysprosium that are in the blue region. Working this close to resonance with the laser wavelength means that, to good approximation, we can retain only this transition in the sum that defines the polarizabilities (equations 1.136 and 1.137) because the other transitions give a negligible contribution when $\lambda_L \approx 405$ nm and, also, one should expect these polarizabilities to be much higher than the typical values one gets when working with far off-resonance potentials created with infrared light at 1064 nm where it was found [59] that $\alpha_{scal}(\lambda = 1064 \text{ nm}) = (184.4 \pm 2.4)$ a.u. and $\alpha_{tens}(\lambda = 1064 \text{ nm}) = (1.7 \pm 0.6)$ a.u. where a.u. stands for atomic units.

Unfortunately working this close to resonance has also some downsides. As already mentioned the laser output is multimode, meaning that it has a broad spectrum of

emission. If some of this emission crosses the transition wavelength going above it, this light will contribute to an attractive potential instead of a repulsive one. Moreover, the more we close the gap between ω_L and ω_0 , the more the light scattering rate defined in 1.138 will grow, eventually diverging when $\omega_L = \omega_0$. Since we want the light-atom interaction to be coherent, real scattering processes are to be avoided, which means that it is mandatory that the laser spectrum shouldn't reach the transition.

3.2 Realizing and monitoring a single mode diode laser

Given what we said about the laser spectrum being broad, the first measurement to make for the laser is to characterize its spectrum, to see if there's really some light crossing the transition frequency.

We made this measurement employing the Monochromator situated in the Atomic Physics lab at the department of Physics and Astrophysics, Unifi. A monochromator is a device that, through the aid of a diffraction grating, can be used to measure the spectrum of a light source. In figure 3.3 is shown the setup we implemented to do the measurement.

The laser beam is focused in the aperture slit of the monochromator. After the slit, light is diverging because of diffraction and a first curved mirror collimates the light, which

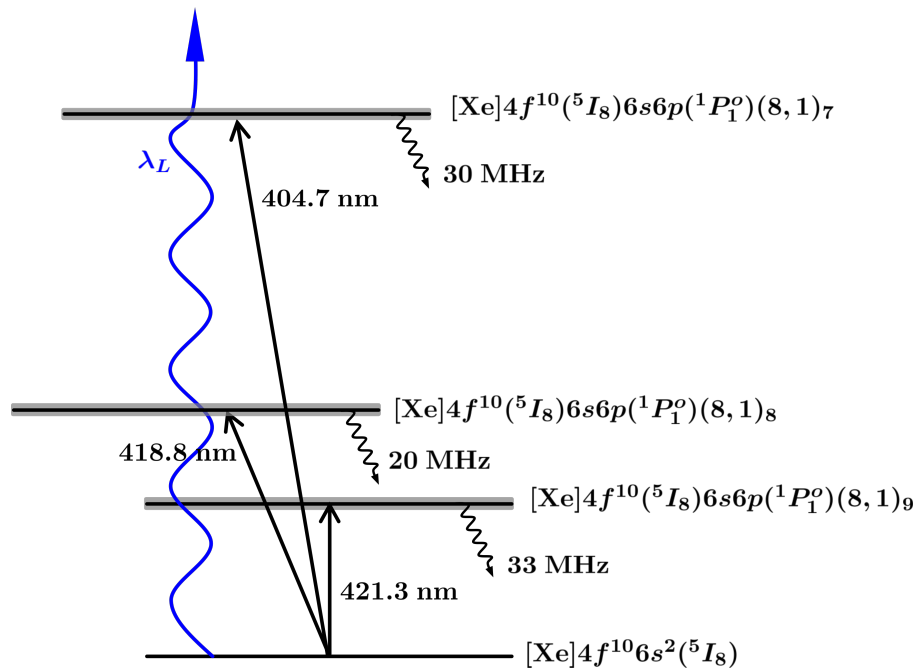


Figure 3.2: Strong absorption lines for dysprosium in the blue region of the spectrum. Data taken from [58]. The 421 nm transition is the one currently exploited in the system for the Zeeman slower, the angled slower, transverse cooling and for the imaging. The energy separations are not to scale.

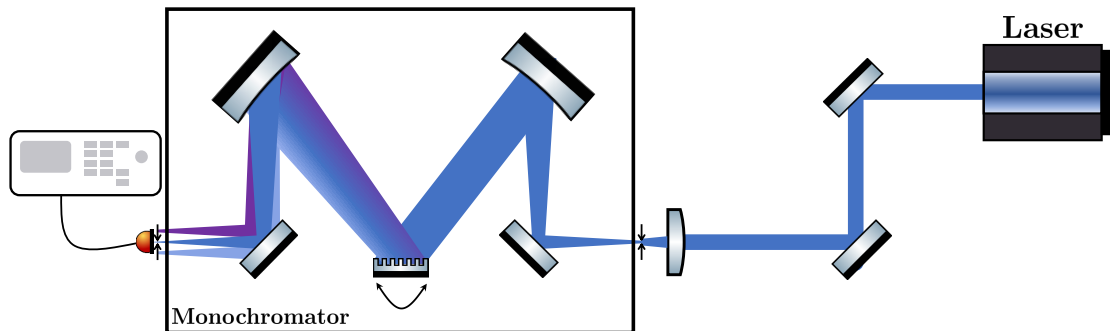


Figure 3.3: Schematics of the setup used to measure the laser spectrum.

then impinges on a diffraction grating. Light after the grating is dispersed so that at different angles there will be different wavelengths. A second curved mirror takes the light coming from the grating and refocuses it in the exit plane, where a second slit is placed. This second slit selects the wavelength that can hit the photodetector placed behind the slit. The grating is mounted on a rotating platform so that, by turning, it can make all the different wavelengths hit the detector. Thanks to this mechanism one can relate the turning time of the grating to the measured light's frequency.

One recorded spectrum of the Nichia diode laser is shown in figure 3.4.

As shown in the picture, the spectrum of the bare diode laser actually crosses strongly the transition's wavelength. Seeing as though the emission of a diode laser is pretty sensitive to the diode's temperature, it's possible to try and change the spectrum by changing the temperature of a Peltier Cell placed in thermal contact with the diode itself. The results of such a procedure are shown in figure 3.5. As shown in the picture, by lowering the diode's temperature it's possible to shift its spectrum to lower wavelengths, although one cannot lower the temperature indefinitely because going under the dew point could damage the diode. Because of this, having the laser working for long periods at a temperature lower than 15° is not an option, and so one has to think about changing the laser spectrum in a

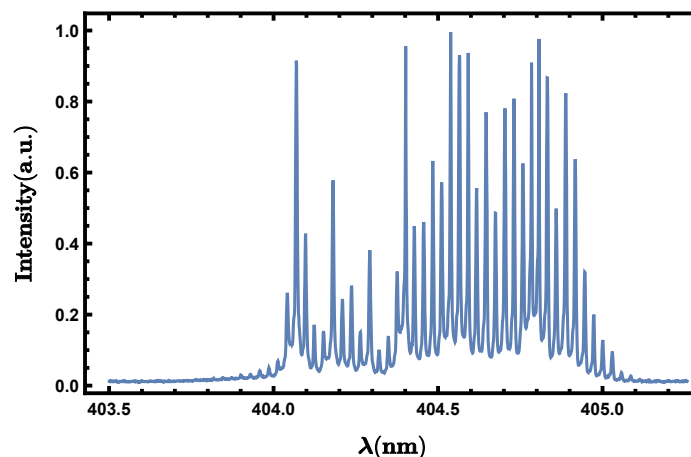


Figure 3.4: Diode laser spectrum at a certain temperature.

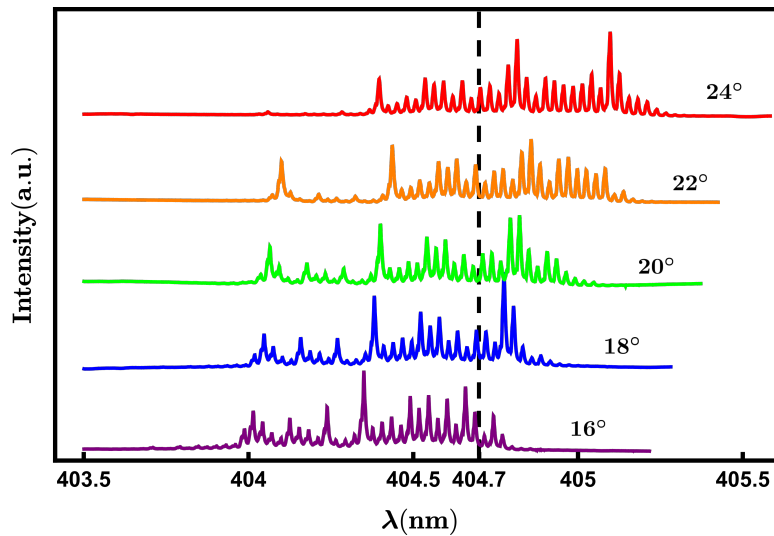


Figure 3.5: Graph showing the diode laser spectrum as its temperature varies. Increasing the temperature tends to increase the emission wavelength because the energy gap of the diode is inversely proportional to the temperature, meaning that as the temperature grows the band gap of the diode gets smaller and so the gain curve of the laser gets shifted upwards in wavelength.

different way than just shifting it.

To do this we implemented an extended cavity for our diode laser, as shown schematically in figure 3.6. The blazed grating in this setup is mounted in the so called *Littrow design*, where the first order of diffraction is reflected back into the diode and acts as a pass-band filter, permitting only a certain range of frequencies to get back into the active medium and gain power, whereas the zero order of the grating defines the output beam direction. This makes the laser system *single mode*, severely reducing the broadness of its spectrum, at the cost of a lower power output given by the non perfect efficiency of the grating. Another advantage of the extended cavity laser configuration (ECDL) is that, by rotating the diffraction grating, it's possible to tune the laser peak emission wavelength by a couple

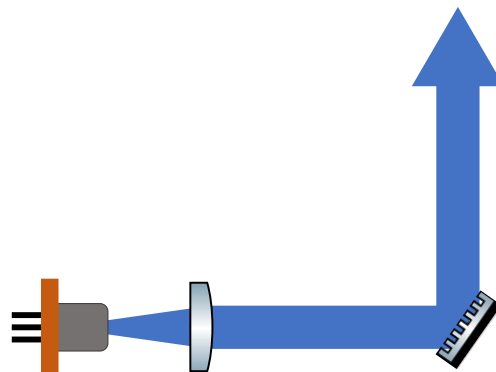


Figure 3.6: Extended cavity configuration for the blue diode laser.

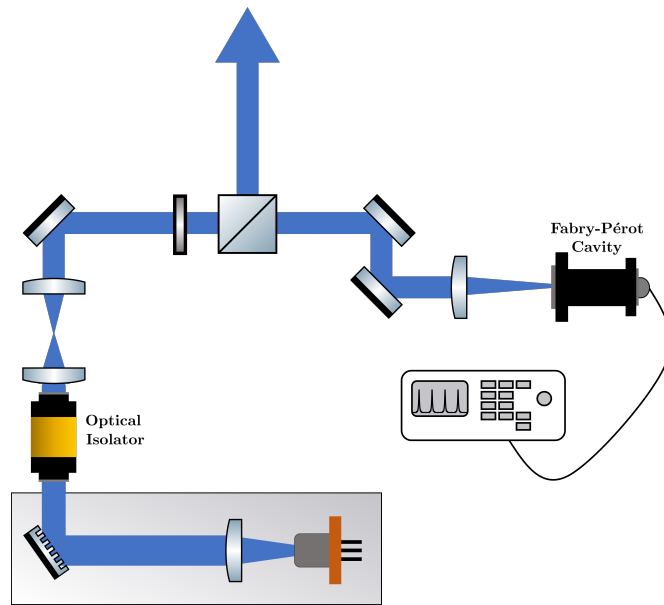


Figure 3.7: Minimal working design to implement a Fabry-Perot cavity to monitor the “Single modedness” of the ECDL laser.

of nanometers.

To monitor the frequency operation of the diode laser we use a scanning Fabry-Perot interferometer (*Thorlabs SA200-3B* [60]), which is basically just a confocal cavity where the back mirror is attached to a piezoelectric and can thus move. This cavity is characterized by a Free spectral range of 1.5 GHz and a typical finesse of about 250.

In figure 3.7 is shown the minimal setup we implemented to monitor the diode emission spectrum. After exiting from the extended cavity, the light passes through an optical isolator, implemented to avoid having reflection coming back inside the active medium of the laser. These reflections are particularly dangerous when the laser is working in single mode. We then place a telescope, made by two plano-convex lenses, to better match the beam profile with the one accepted by the cavity. A beam splitter and a half waveplate are then used to select how much power goes towards the cavity and how much goes instead towards the atoms. Lastly, a lens is placed before the cavity to have the waist of the laser in the middle of it, and to make it the right size. By scanning the position of the back-end mirror of the cavity and monitoring its transmission signal through the use of a photodiode (that’s already mounted on the Thorlabs cavity) it’s possible to clearly distinguish when the laser is working in single or multi mode, as shown in figure 3.8. Using the configuration shown in figure 3.7 we are now ready to test if this now single mode laser can interact in a coherent way with the Dysprosium atoms. To do that we measure lifetimes of a dysprosium BEC as a function of the interaction time with this blue laser coming from the ECDL cavity.

The BEC is initially trapped in a crossed dipole trap made by two 1064 nm infrared lasers, and the blue laser hits the BEC in a plane that is perpendicular to this crossed trap, as shown in figure 3.9. This kind of measurement is directly related to the scattering

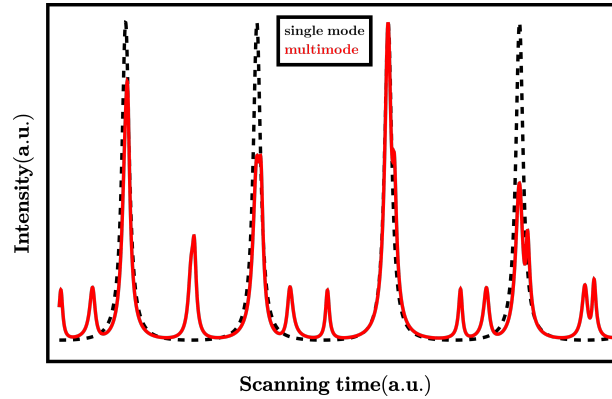


Figure 3.8: Oscilloscope signal when the laser is working in single or multi mode.

properties of the atom light interaction since, if an atom scatters a blue photon, it gets a recoil energy of about 360 nK and this is enough to kick it out of the dipole trap. The results for the lifetime in this configuration are shown in figure 3.10.

Using a fitting function of the form

$$f(t) = Ae^{-t/\tau} \quad (3.1)$$

it's possible to extract from the data the lifetime τ , defined as the interaction time at which the number of trapped atoms is $1/e$ of the initial number.

With the setup shown in figure 3.7 we were able to get a lifetime of (120 ± 30) ms. This lifetime is far too short for our purposes, and such a result shows that even if the laser is working in single frequency mode, since we are working extremely close to an absorption transition for the atoms, there is still some light that crosses resonance and that's making the scattering rate really high. To double check this result we also made lifetime measurements on the thermal gas, which we can get by just stopping the evaporation ramp midway. The results of this measurement are shown in figure 3.11. As one can see from this picture, the size of the thermal cloud is increasing the more it

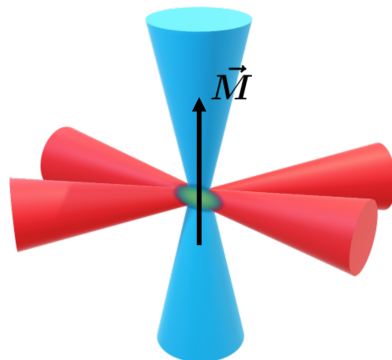


Figure 3.9: Sketch of the crossed dipole trap (in red) and the blue laser (in blue) on top of the BEC. The magnetization \vec{M} of the BEC is directed along the blue beam.

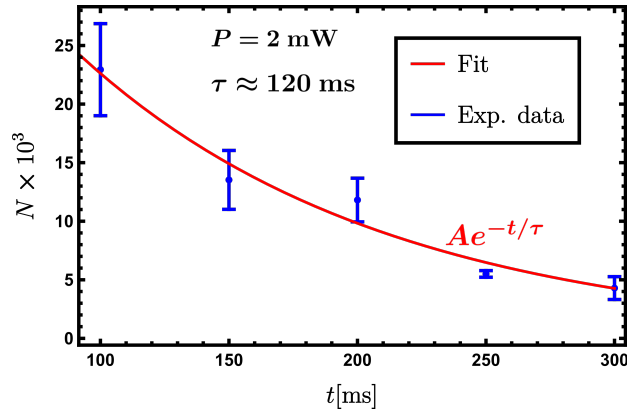


Figure 3.10: Lifetime of the BEC as a function of the interaction time with the blue laser. In red is shown an exponential fit on the data, used to get the lifetime τ of the condensate.

interacts with the blue laser, directly showing the heating produced by the laser. To solve this problem we employed a second dispersive element in the optical path of this blue laser, like it's shown in figure 3.12. In this new setup, the laser light still goes through the optical isolator and the first telescope that were already placed before. After the telescope the light gets splitted in two branches, one going to the monitoring cavity and the other goes to the second grating. We can select how much power goes in both branches thanks

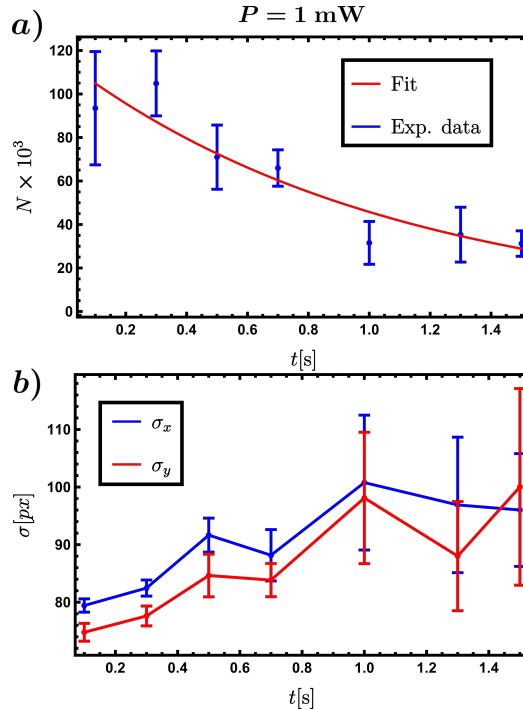


Figure 3.11: (a) Plot of the lifetime of the thermal gas as a function of the interaction time with the blue laser. (b) Plot of the size of the thermal gas as a function of the interaction time with the laser. The measurement was done with a laser power of about 1 mW.

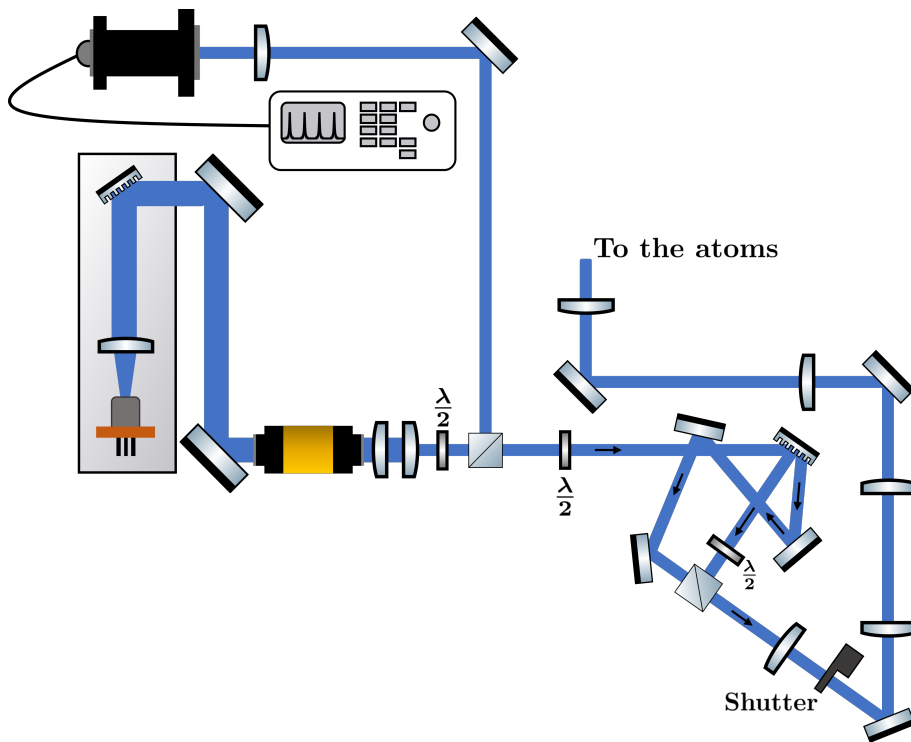


Figure 3.12: Sketch of the setup used to send both the first and the zeroth order of a second diffraction grating to the atoms.

to the half waveplate placed before the beam splitter.

Since, as is shown in figure 3.13, gratings have different efficiencies for different polarizations, before impinging on the grating the light passes through a second half waveplate to match its polarization with the one for which the grating has its peak efficiency. After hitting the grating light is diffracted into two main orders. The zero-th, which is the one that is not sensitive to the wavelength, and the first, which instead makes light with different wavelengths go into different directions. The mirrors' setup shown in figure 3.12 is made so that both the zeroth and the first order can be directed towards the atoms. A first telescope made with cylindrical lenses is then implemented in the optical path to make the beam profile more circular, and a second telescope is instead placed to make the beam bigger, so that when the light hits the final focusing lens it will have a smaller waist in the atomic plane. A shutter is also placed inside the optical path to change the interaction time with the atoms. Thanks to the second grating we can send the remaining on resonance light that is still present in the laser away from the centroid of the beam. In this way if the beam is aligned to hit the atomic cloud the spurious wavelengths will not interact with the atoms and so we should expect to see an increased lifetime of the BEC in this configuration. The results of this new lifetime on the BEC are shown in figure 3.14. As one can see from the picture, with this new experimental setup we get a much longer lifetime for the trapped BEC, that is (1.5 ± 0.4) s, which shows how we were really able to filter out the on resonance wavelengths and make them not interact with the atoms.

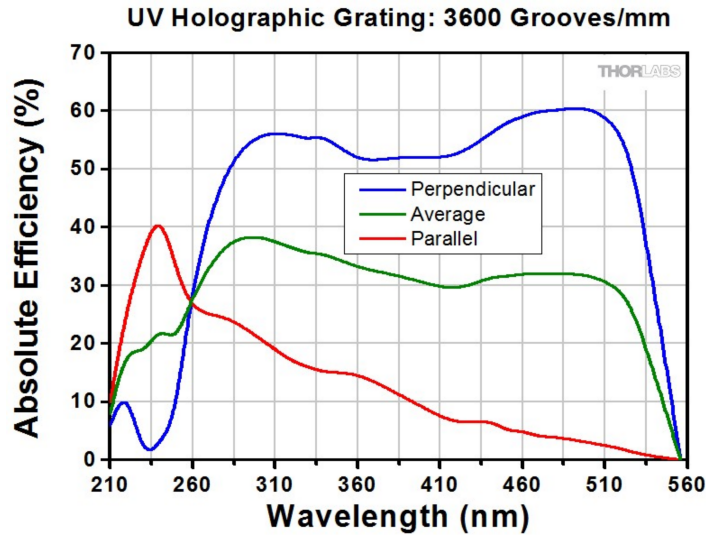


Figure 3.13: Efficiency plotted as a function of wavelength for a grating. The different curves are plotted for different incident polarization. Image taken from [61].

This measurement was made with a blue laser power P of about 0.5 mW and a laser waist on the atoms w_0 of about 30 μm , although the waist in this configuration is a bit ill defined since in this setup the laser was not a gaussian beam, as is clearly seen in figure 3.15 (a), where it's shown a picture of the beam waist profile as captured by a camera. This is problematic because, to work with the DMD, one wants to have a gaussian beam impinging on it but also to make the measurement of the atom polarizability (see section 3.3) is also important to work with gaussian beams. To solve this problem we decided to couple this blue laser into a single mode fiber, as shown schematically in figure 3.16. Thanks to the use of this single mode fiber, we can now send to the atoms a much better shaped beam,

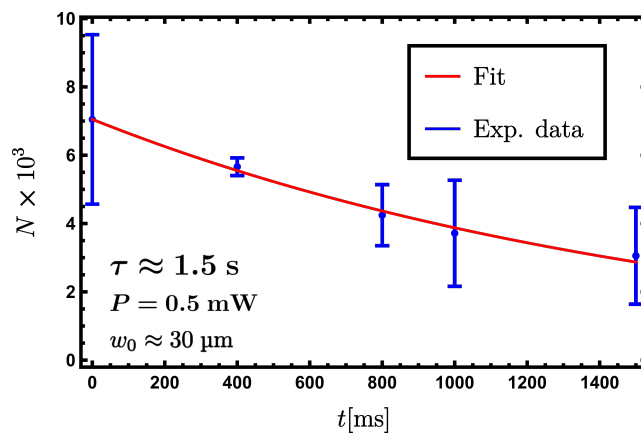


Figure 3.14: Results for the lifetime of the BEC in the new configuration of figure 3.12. Thanks to this new setup we see a much improved lifetime, which shows how this setup is effective at eliminating the spurious wavelengths from the atoms. This measurement was done with a laser power of about 0.5 mW and a waist on the atomic plane of about 30 μm .

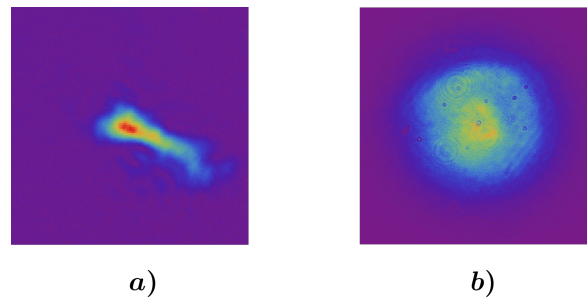


Figure 3.15: Recorded image on a CCD camera of the beam's radial profile. (a) Before the coupling to the single mode fiber. (b) After exiting the single mode fiber.

much more similar to a gaussian one, as shown in figure 3.15(b). Furthermore, since the beam that is hitting the single mode fiber is still the first order of a diffraction grating, different wavelengths inside this beam will impinge on the collimating lens of the fiber in different positions, meaning that wavelengths that are far enough away from the beam center will not get coupled inside the fiber. Because of this the fiber in this particular setup also acts as a frequency filter. To show that this is really what's happening we made another lifetime for the BEC with the setup shown in figure 3.16. The results for this lifetime are shown in figure 3.17. This result shows that the setup shown in figure 3.16 is indeed a valid configuration to create a gaussian beam of blue light that can be tuned to work around 1 nm away from resonance but still interact in a coherent way with the

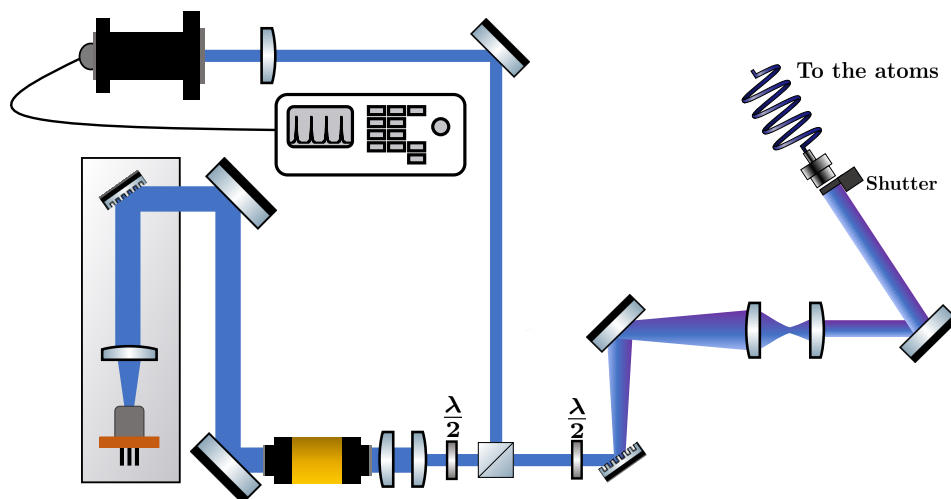


Figure 3.16: Sketch of the setup used to couple the blue laser into a single mode fiber. The light that gets coupled to the fiber is still coming from the first order of a diffraction grating. This makes so that wavelengths that are far from the central emission peak of the laser hit the collimating lens of the fiber on its edge (or they don't hit at all) and because of this they don't get coupled inside the fiber. Thanks to this the fiber in this scheme also acts as a frequency filter for the laser. A fast shutter is placed just before the fiber to make short pulses of blue light of about 5 ms.

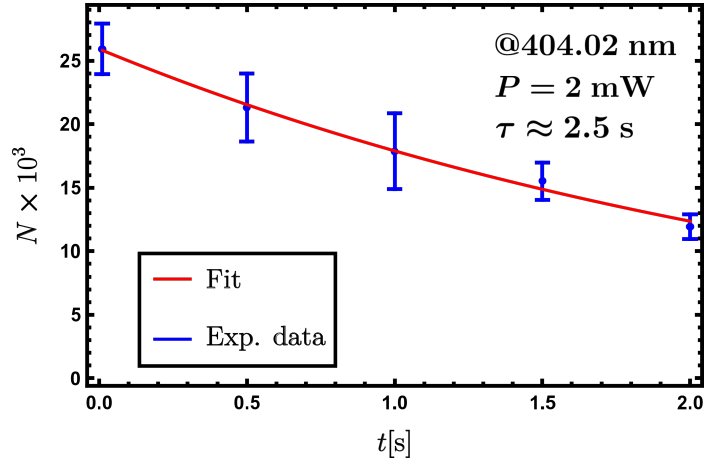


Figure 3.17: Lifetime of the trapped BEC as a function of the blue laser power using the setup shown in figure 3.16. The measured lifetime is $\tau = (2.5 \pm 0.3)$ s. The blue laser wavelength reported in this picture is measured through a wavemeter.

atoms.

The downside of the setup shown in figure 3.16 is that, to make the beam gaussian and to get rid of the on resonance wavelengths, we make use of two diffractive elements (in our case, two gratings) and we also couple the light inside a single mode fiber. Out of the extended cavity we have about 40 mW of power. After the optical isolator we have 25 mW left. After the grating in the first diffraction order we have about 10 mW and this light gets coupled inside the fiber where, because of the high mismatch between the laser mode and the fiber one, we only couple 30% of the light into the fiber. At the end of the optical path we can only send about $2 \div 3$ mW of power to the atoms. In the future, when we will insert the DMD in the system, this power will be cut even more because the DMD also acts as a diffraction grating, sending some light into a lot of different orders and we will only pick one of them. Because of these considerations we might ask ourselves if this laser power will be enough to create a potential that's deep enough to trap the atoms. As one can see from the expression 1.139, the potential for the atom-light interaction does not only depend on the intensity of the laser beam, but it also depends on another quantity called *polarizability*, that in principle should be very high seeing as we are working extremely close to a resonance. If the polarizability is high enough we could work with a low power laser and still have a high enough potential thanks to the polarizability. In the next section I present the work we made to make a measurement of this polarizability.

3.3 Measurement of the Dy's polarizability at around 404 nm

The first part of the setup we use to measure the polarizability is the same showed in figure 3.16. Now, the light that exits the fiber goes through another optical path that is

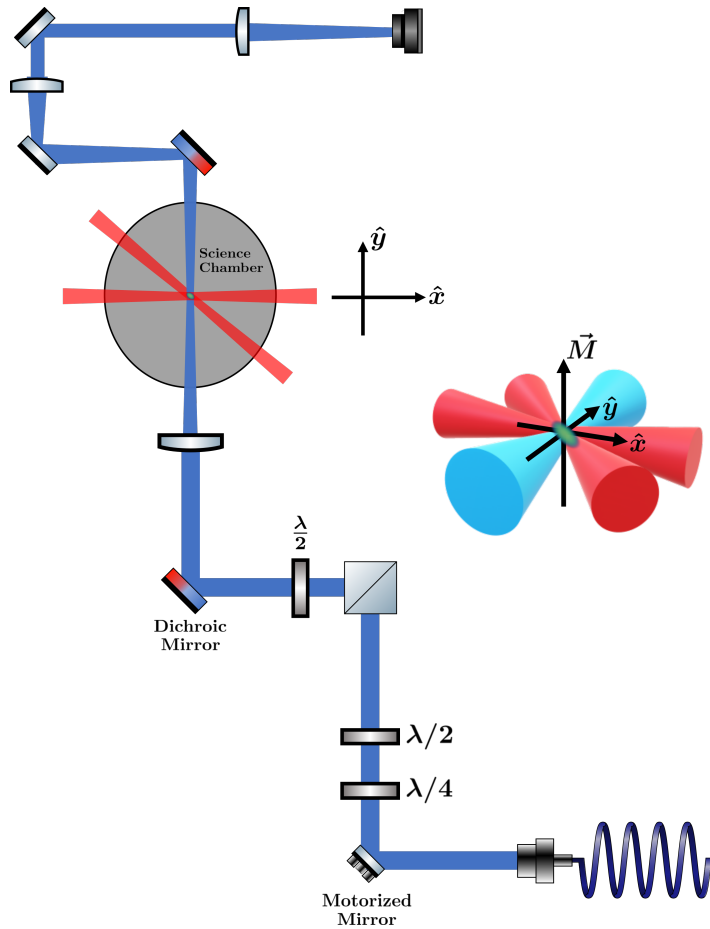


Figure 3.18: Last part of the experimental setup used to measure the dynamical polarizability of dysprosium. The motorized mirror is used to align the beam with the trapped atomic cloud. In the path there's a dichroic mirror just because it's also part of the MOT optical path. The camera on the top is used to make an imaging of the blue beam and measure its waist on the atomic plane.

shown schematically in figure 3.18.

The light comes out of the fiber (the same fiber that it enters in figure 3.16) with an elliptical polarization. To correct this we employ a $\lambda/4$ and a $\lambda/2$ waveplate in series to get back a linearly polarized beam. After a beam splitter we then have another half waveplate, and this we use to change the angle between the polarization of the laser and the magnetization \vec{M} of the BEC.

By changing this angle, that we define as θ , we can effectively change the total polarizability, given in section 1.5 and that we rewrite here for simplicity:

$$\alpha(\theta) = \alpha_s + \frac{3 \cos^2(\theta) - 1}{2} \alpha_t. \quad (3.2)$$

In the expression 3.2 the factor $(3M^2 - F(F + 1))/(F(2F - 1))$ is not present since the atoms are in the stretched state $M = -F = -8$.

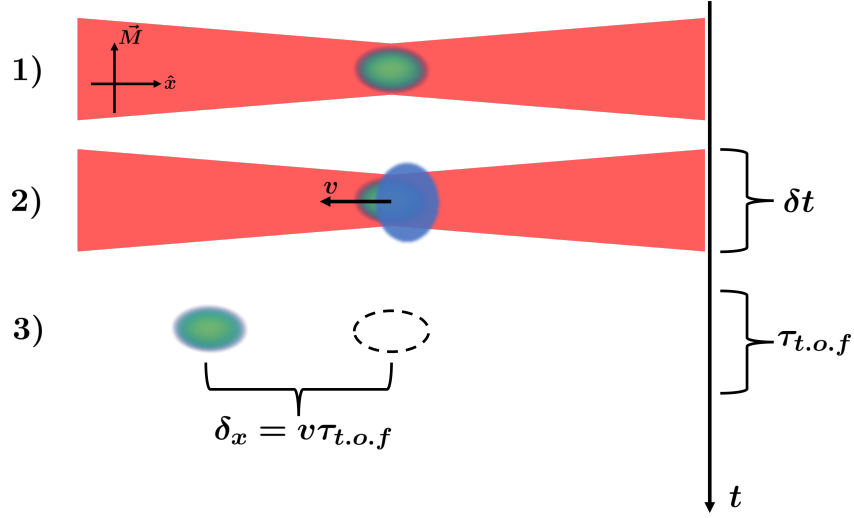


Figure 3.19: Experimental procedure to measure the polarizability. (1) The BEC is initially loaded in the crossed dipole trap. (2) At a certain time, the blue beam strikes the atomic cloud, and imprints a velocity on the atoms for a time δt . (3) After the second phase is over, both the blue beam and the infrared trap are switched off and the BEC undergoes free expansion for a time $\tau_{t.o.f.}$. In this phase the imprinted velocity of the second step gets converted into a displacement. After $\tau_{t.o.f.}$ has elapsed the imaging beam, directed along \hat{z} , hits the cloud and permits the measurement of δ_x .

To measure α we need to link it to some observable quantity. In our case it's not possible, as was done in [59], to measure the dipole oscillation of the BEC inside a trap made with this blue light, since our interaction is, all in all, repulsive. What we decided to do instead was to measure the displacement δ_x that the BEC makes when it's struck by a pulse of blue light. In figure 3.19 is shown a scheme of our experimental procedure. We start with the BEC trapped in a crossed dipole trap. At a certain time this BEC gets hit by the blue laser and interacts with it for a time defined as δt . This interaction imprints a velocity on the cloud. After the interaction time is over we turn off both the blue beam and the trap and let the BEC expand in time of flight for a time $\tau_{t.o.f.}$. During this time the imprinted velocity given by the blue beam gets converted into a displacement.

At the end we make a saturation absorption imaging of the cloud thanks to an on resonance 421 nm beam coming from the vertical direction. This imaging permits the measurement of δ_x . If the pulse is short enough so that the cloud isn't displaced while the beam is still on, we can write δ_x as

$$\delta_x = \frac{F_x \delta t \tau_{t.o.f.}}{M} \quad (3.3)$$

where F_x is the force imprinted on the BEC by the blue laser, δt is the pulse duration, $\tau_{t.o.f.}$ is the free expansion time for the atoms before the imaging and M is the dysprosium mass. In this approximation $F_x \delta t / M$ can be seen as the velocity imprinted on the atoms

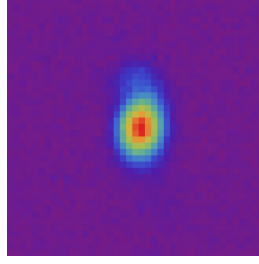


Figure 3.20: Recorded image on the camera shown in the optical setup 3.18 of the cross section of the 404 nm beam. This image is used to measure the beam waist in the atomic plane.

and by multiplying it by $\tau_{t.o.f.}$ one can get the expression for the displacement.

For the force F_x , there are two possible choices that one can make. If we suppose that the atomic cloud is point-like in dimensions with respect to the blue beam, and by supposing that the cloud sits in the place where the force has its maximum value, one can use the formula 1.146 for the force. Of course, the point like approximation is not completely justified since the BEC has some finite dimensions with respect to the laser waist¹ and to better refine this approximation one can use, instead of F_x^{max} , an average force F_x^{avg} , that we can define as the average of $F_x(\mathbf{r})$ over the atomic cloud in this way:

$$F_x^{avg} = \int d\mathbf{r} F_x(\mathbf{r})n(\mathbf{r}) \quad (3.4)$$

where $n(\mathbf{r})$ represents the BEC density normalized such that $\int d\mathbf{r} n(\mathbf{r}) = 1$, and $F_x(\mathbf{r})$ has the form reported in 1.145, except for the fact that we now have to deal with our real beam that, as one can see from figure 3.20, has an elliptical shape. To take into consideration this fact we slightly modify the expression of the force in the following way

$$F_x(\mathbf{r}) = -\frac{4P\alpha(\theta)}{\pi\epsilon_0 c w_x^3 w_z} x e^{-2x^2/w_x^2} e^{-2z^2/w_z^2} \quad (3.5)$$

where w_x and w_z represent the beam waist in the x direction and in the direction of the magnetization, respectively. These waists are measured through the CCD camera shown in figure 3.18 and to relate the dimensions on the camera to the ones in the atomic plane we make a calibration of the imaging's magnification that is explained in section 3.5. The results for these two waists are $(w_x, w_z) = (26 \pm 1, 34 \pm 1) \mu\text{m}$.

In the expression 3.5 it's not taken into consideration the fact that the waist is not the same throughout all the atomic dimension since the cloud has some width even in the propagation direction of the beam. This is because this width is of the order of $2 \mu\text{m}$ and is much less than the depth of focus of the beam that can be calculated to be around 7 mm , which means that the waists are practically constant throughout the BEC extension. Since it's still not possible to get a full experimental representation of $n(\mathbf{r})$, the next best thing we could do was to use for $n(\mathbf{r})$ the result of a simulation for our trapped BEC inside the

¹The BEC dimensions are $(\sigma_x, \sigma_y, \sigma_z) \approx (10, 2, 6) \mu\text{m}$.

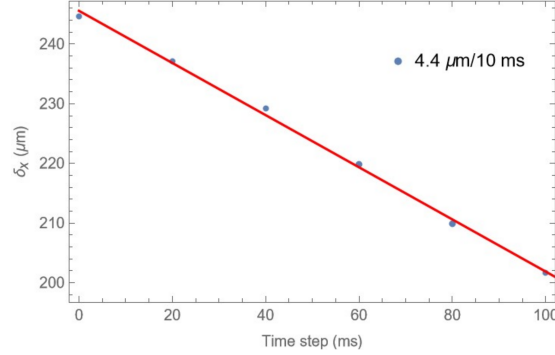


Figure 3.21: Displacement on the atomic plane of the beam as a function of the time pulses for the motorized mirror. Thanks to this measurement we can convert time pulses into atomic plane displacements.

crossed dipole trap. By doing the integral in 3.4 we get a 7% decrease of F_x^{avg} with respect to F_x^{max} . Even in this case though, the integral is made supposing that the center of mass of the BEC is positioned in the point where it feels the maximum force along x , this point being $\mathbf{r} = (\pm w_x/2, 0, 0)$. To be sure of this one needs to have enough experimental sensitivity on the cloud-beam relative displacement. In our case this is done with the aid of a motorized mirror, shown in figure 3.18. The motor on the mirror can tilt it in both directions and we can make it move by sending current pulses that can last as little as 10 ms through it. In figure 3.21 it's shown the measurement we made on this mirror to convert the time pulses into displacements in the atomic plane. We were able to show that this motorized mirror gives the sensitivity that we need by making the measurement shown in figure 3.22. In this figure it's shown the atomic center of mass displacement from its starting position after having interacted with the blue beam for a fixed δt and for a fixed $\tau_{t.o.f.}$, as a function of the beam position. This measurement shows that the motorized mirror we are using has high enough sensitivity to follow all the trend for the force, and by placing it in the maximum value for the displacement, we can be sure that the blue beam is exerting the maximum force on the atomic cloud. In the picture β represents the angle made by the direction of the imprinted velocity on the atoms (that I defined as the x -axis) and the horizontal direction of the imaging camera. This angle can be better interpreted by looking at figure 3.23. We are now ready to make some quantitative measurements regarding the scalar and tensor components of the polarizability.

The first thing we did was to measure the ratio between α_s and α_t . To do this we made measurements of the displacement of the BEC as a function of the angle θ between the light's polarization and the cloud's magnetization, with $\delta t = 9$ ms, $\tau_{t.o.f.} = 25$ ms and the beam's position fixed where it imprints the maximum force. Because of this, we can see from equations 3.5 and 3.3 that the displacement δ_x will depend linearly on the polarizability. The results of one of these measurements are shown in figure 3.24. δ_x shows clearly an oscillating behavior as θ varies. This is a nice test of the formula 3.3 and by fitting the experimental results with a function of the form 3.2 it's possible to extract from these measurements the value of α_s/α_t at a specific wavelength. To change the angle θ in

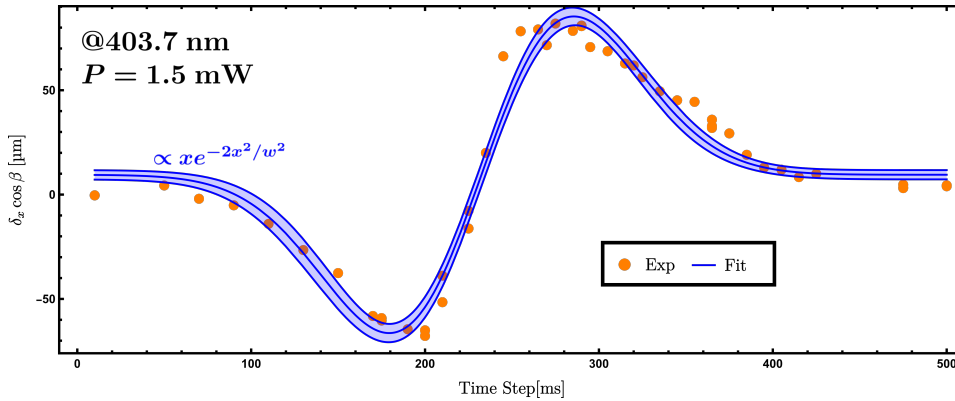


Figure 3.22: Plot of the BEC displacement in time of flight versus blue beam position (given in time steps of the motorized mirror). Through the aid of the motorized mirror, we were able to follow all the trend for the force, and by placing ourselves in either the maximum or minimum of this curve with the mirror, and doing the same procedure also for the orthogonal axis, we can be sure that atoms are feeling the maximum value for the force.

our experiment we make use of the last half waveplate shown in figure 3.18. To not skew the results, we need to make sure that the laser power in the atomic plane remains as fixed as possible when we change the light's polarization. The absorption of all the optical instrumentation has been shown to not depend on the light's polarization much, but as is shown in figure 3.18, after the last waveplate there is a dichroic mirror that can't be substituted since it's also part of the MOT optical setup. This dichroic mirror is made so

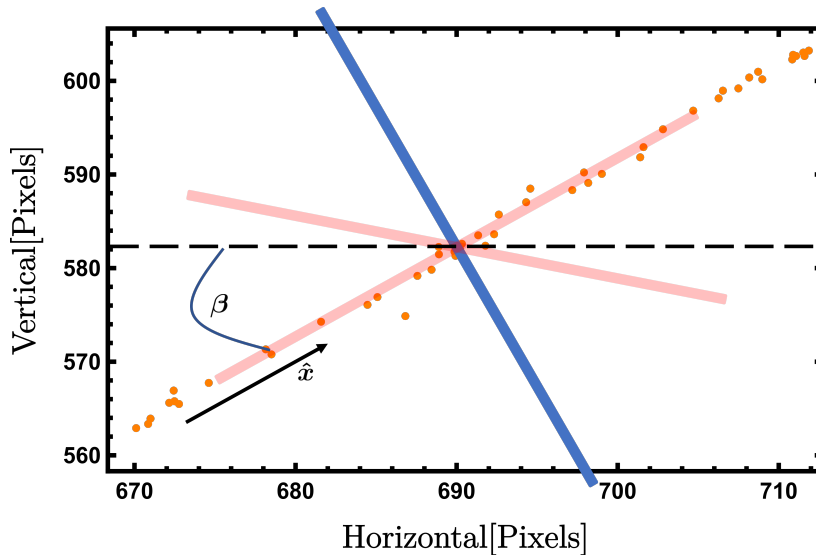


Figure 3.23: Definition of the angle β made by the horizontal direction of the camera used for the imaging and the x axis. The orange dots are the measured position of the BEC after a time of flight of 25 ms for different positioning of the blue beam. The BEC moves along a straight line that is orthogonal to the beam's direction.

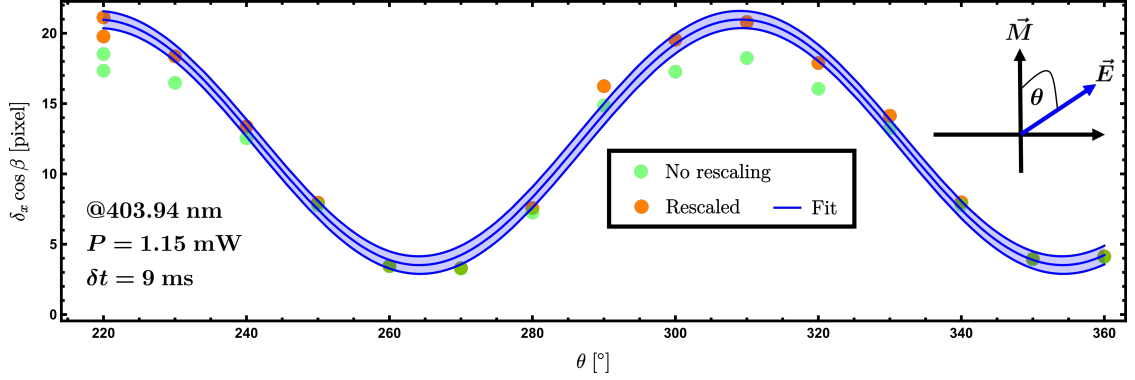


Figure 3.24: Displacement of the atomic center of mass $\delta_x \cos \beta$ along the horizontal direction of the imaging camera, as a function of the polarization angle θ . In green are shown the experimental data and in orange the experimental data rescaled to take into consideration the effect of the dichroic mirror.

that red light passes through it and blue light gets reflected instead. The problem with this mirror, as is shown in figure 3.25, is that it has a reflective power that depends strongly with the incident light's polarization. To correct for this power fluctuations we first make a fit on the experimental values of figure 3.25 with a sinusoidal fitting function of the form

$$f(\theta; A, B, \text{off}) = A \sin \left[\frac{2\pi}{B} \frac{\pi(\theta - \theta_0)}{180} \right] + \text{off} \quad (3.6)$$

and then, since the displacement is linear both in the power and in the polarizability, we can directly use this function to rescale the experimental values for $\delta_x(\theta)$. In figure 3.24 in green are shown the experimental data without this correction and in orange the one with the correction applied. By making measurements such as the one shown in figure 3.24 at different wavelengths (this can be done by slightly turning the grating

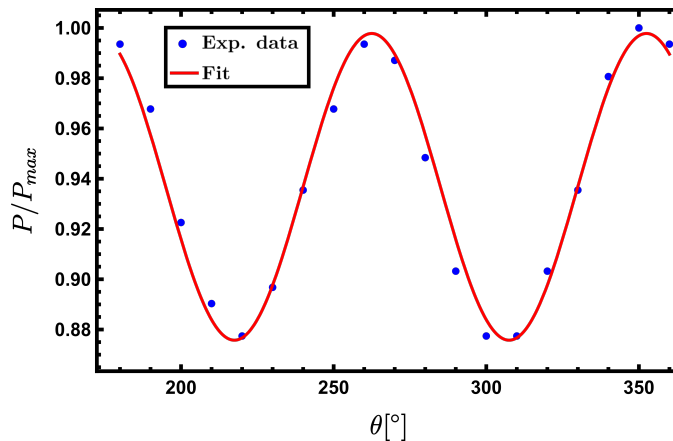


Figure 3.25: Normalized power of the blue laser reflected from the dichroic mirror as a function of the incident light's polarization direction expressed through the angle of the last half waveplate.

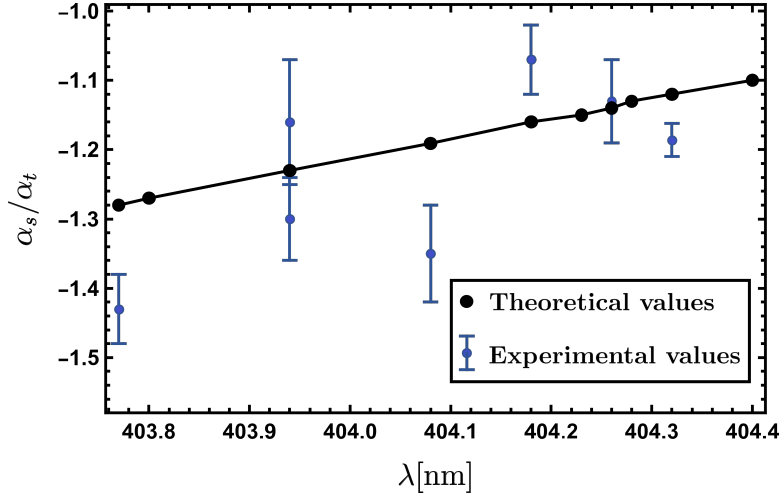


Figure 3.26: Results for α_s/α_t as a function of the laser wavelength. In black it's shown the theoretical prediction, and in blue the experimental results.

creating the extended cavity for the laser) it's possible to study the trend of α_s/α_t as a function of the laser wavelength. The results for this are shown in figure 3.26, along with the theoretical prediction for α_s/α_t made by using the expressions 1.136 and 1.137 and dysprosium transitions' data taken from [58]. Of course, only having access to the ratio α_s/α_t is not enough to give an estimate of the attainable potential depths. To get this one needs to know the absolute values of both α_s and α_t .

To get this information we make another type of measurement, fixing the value of the angle θ to have the maximum displacement of the cloud (this fixes the value of the polarizability to $\alpha_{max} = \alpha_s - \alpha_t/2$ since in our case α_s and α_t have opposite sign) and what we change is instead the value of the power P of the laser. To get a meaningful value for α in this way one needs the complete expression that relates δ_x with P . By combining equation 3.3 with 3.4 and with 3.5 one gets:

$$\delta_x = \mathcal{I} \frac{2\alpha\delta t\tau_{t.o.f.}}{\pi\sqrt{eM\epsilon_0}cw_x^2w_z} P \quad (3.7)$$

where \mathcal{I} is defined to be

$$\mathcal{I} = e^{1/2} \int d\mathbf{r} n(\mathbf{r}) \left(1 - \frac{2x}{w_x}\right) \exp\left[-\frac{1}{2}\left(1 - \frac{2x}{w_x}\right)^2\right] \quad (3.8)$$

And if we use the approximation $n(\mathbf{r}) = \delta(\mathbf{r})$, that is the mathematical expression of saying that all the atoms feel the maximum force possible, we get $\mathcal{I} = 1$, and if we instead want to take into consideration the fact that the atomic cloud has a finite size, we can either use as $n(\mathbf{r})$ the Thomas-Fermi expression for the density of a trapped BEC or use for $n(\mathbf{r})$ the result of a simulation. In either case the value of the integral drops from the value of 1 to about 0.93, this has the direct consequence of increasing by 7% the result for the polarizability. Equation 3.7 shows really well that the displacement is

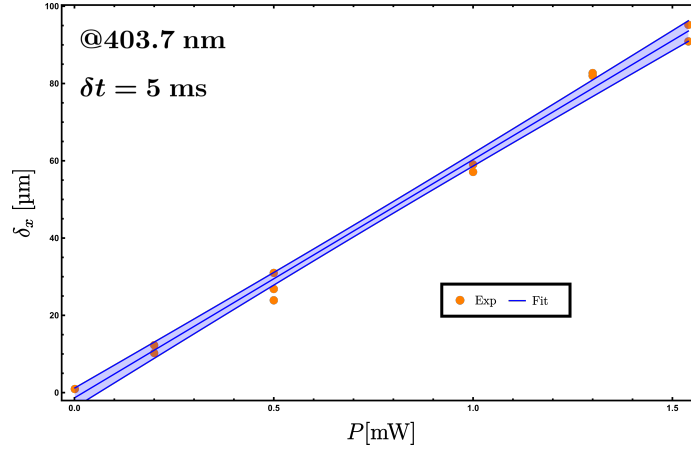


Figure 3.27: Experimental results for the displacement of the atomic cloud as a function of the laser power.

predicted to scale linearly with the laser power, and in the slope of this line one can find the polarizability. In figure 3.27 is shown a result of one of the measurements made for δ_x vs P . By making a linear fit on this experimental data, and by comparing the slope of this fit with the one predicted in 3.7, it's possible to get a measurement of the full value of the polarizability, that in this case is $\alpha_s - \alpha_t/2$. By then using the results shown in figure 3.26 for the ratio between α_s and α_t , it's possible to determine the value of both α_s and α_t . Our experimental results for α_s and α_t are shown in figure 3.28, where they are compared with their theoretical prediction. As can be seen from the picture, there is a factor of about three of discrepancy between the experimental results and the theoretical predictions.

If equation 3.7 is correct, than this discrepancy can only come from the following sources: An error in the theoretical formulas used to give an estimate of α_s^{theory} and α_t^{theory} , or some systematic error made in the experimental measurement of the quantities that appear in equation 3.7. The first hypothesis is the least likely one. This is because the formulas 1.136 and 1.137 were checked by comparing the results they give for the polarizabilities with the ones obtained in [59, 62], where they give a good agreement with those experimental results. The theoretical predictions for α_s, α_t depend on the experimentally measured values for the dysprosium' transition wavelengths and intensities. These quantities were taken from the NIST database and their experimental error is extremely low (about 10% or lower for the Einstein's coefficients [63] and around 0.001 nm of error on transition's wavelengths [64]), so it's also not likely that we are inputting in the formula some blue transitions that are not accurate enough. Another possibility that could skew the theoretical expression for the polarizabilities could be the presence of a weak transition that is not tabulated and is around our working wavelength. This is not likely to be the case since it would require the polarizabilities to scale differently from the theoretical predictions. In particular, a new line would change the ratio between α_s and α_t for some wavelengths, and this is not seen from the results showed in figure 3.26. If the error is not coming from the theoretical values $\alpha_s^{theory}, \alpha_t^{theory}$ than it stands to reason that it is probably coming from a systematic error

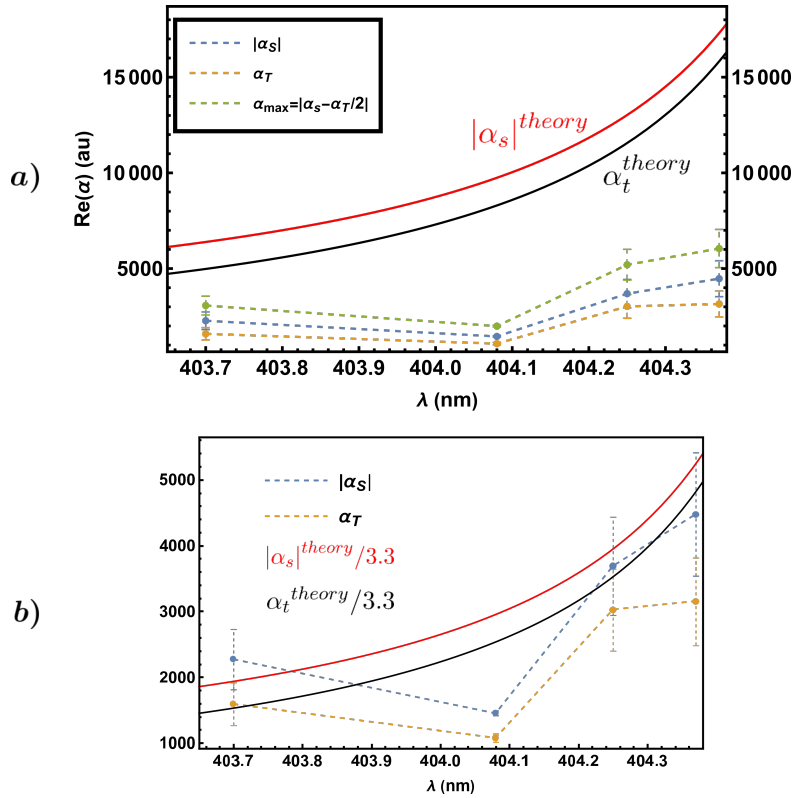


Figure 3.28: (a) Experimental results for the scalar and tensor components of the polarizability as a function of the laser wavelength, compared to the theoretical predictions. (b) Theoretical predictions scaled by a factor of $1/3.3$ to make them sit on top of the experimental data for comparison. The polarizabilities are expressed in atomic units.

inside equation 3.7. This possibility is also strengthened by the fact that the measurements for the ratio α_s/α_t shown in figure 3.26 are in better agreement with the theory than the absolute ones. This error could likely stem from the measurement of the power P of the laser in the atomic's plane and from the measurement of the waist. Regarding P , this quantity can be measured only before the vacuum chamber through the use of a power meter, that is calibrated with an accuracy of about 10%. The value of P is then reduced in equation 3.7 by a factor of $\varepsilon = 0.9$ to account for the light's reflection of the glass window of the vacuum chamber. A systematic error can be attributed to ε , but to account for the discrepancy with the experimental values of α we would need to have $\varepsilon \approx 0.3$, which means that the glass window only transmits 30% of the laser power, and this is extremely unlikely. What is likely to cause problems inside equation 3.3 is the measurement of the beam waist in the atomic plane. In fact, since the waist appears in the equation raised to the third power, the displacement is seen to be extremely sensitive on the value of the waist. Therefore, if we were measuring waists that are just 1.5 times smaller than the real ones, the discrepancy from theory and experiment would be explained. This is the most likely cause for the disagreement between theory and experiment. The source of this systematic error could be the fact that we are making a calibration using a 421 nm

beam, that is the one used for the imaging, while our beam is working at 404 nm. This discrepancy could lead to different focal lengths for the lenses in the imaging setup showed in figure 3.18, since at such low wavelengths the index of refraction of glass-like materials can change very fast. This would lead to a systematic error on the calibration of the imaging system described in section 3.5.

3.4 Injection locking of a diode laser

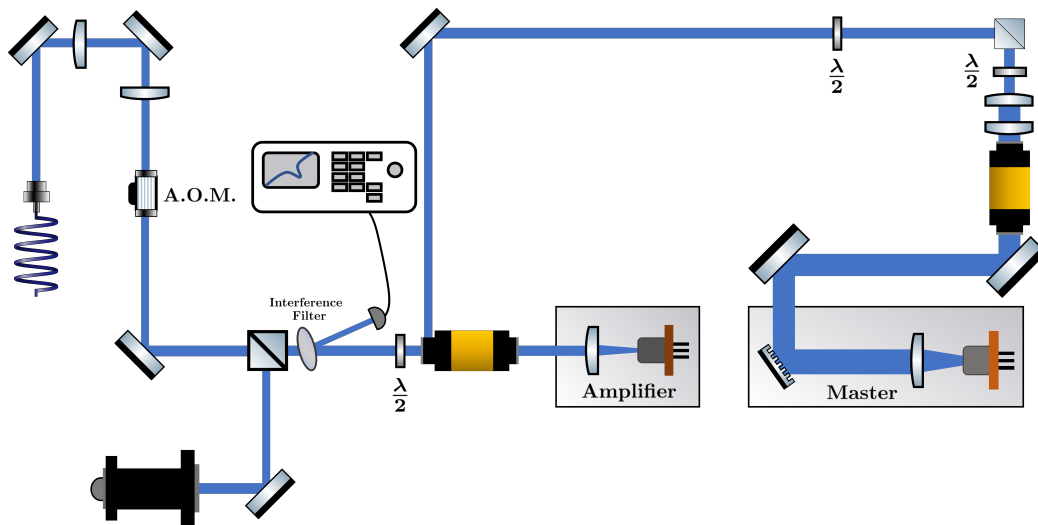


Figure 3.29: Sketch of the experimental setup used for the injection locking of our diode laser.

In this section I report the experimental realization of an injection lock configuration realized to create a powerful single mode laser. The scheme implemented is based on [65]. In figure 3.29 it's shown a sketch of the optical setup for the injection lock. The master and the amplifier lasers are produced by two different *NICHIA NDV4313* diodes. The master works in single mode thanks to the grating placed in front of it whereas the amplifier laser in and of itself is multimode but can be forced to work in single mode when it's injected by the master.

This injection is made by having the master laser coming through the amplifier's active medium. In the figure, this happens by making the second beam splitter of the optical isolator of the amplifier reflect the master's light. Because of the working principle of optical isolators, this reflected light will be transmitted from the first beam splitter and is coupled inside the amplifier's diode, whereas the amplifier's beam can pass through the optical isolator unaltered. After the amplifier's optical isolator we place an interference filter to reduce the power on the wavelengths that are too close to the 404.7 nm absorption line of dysprosium. The reflection signal from the filter is monitored through a photodiode and shows a sudden drop when the amplifier gets injection locked. This signal could be employed in the future to make a PID control scheme for the injection current on the

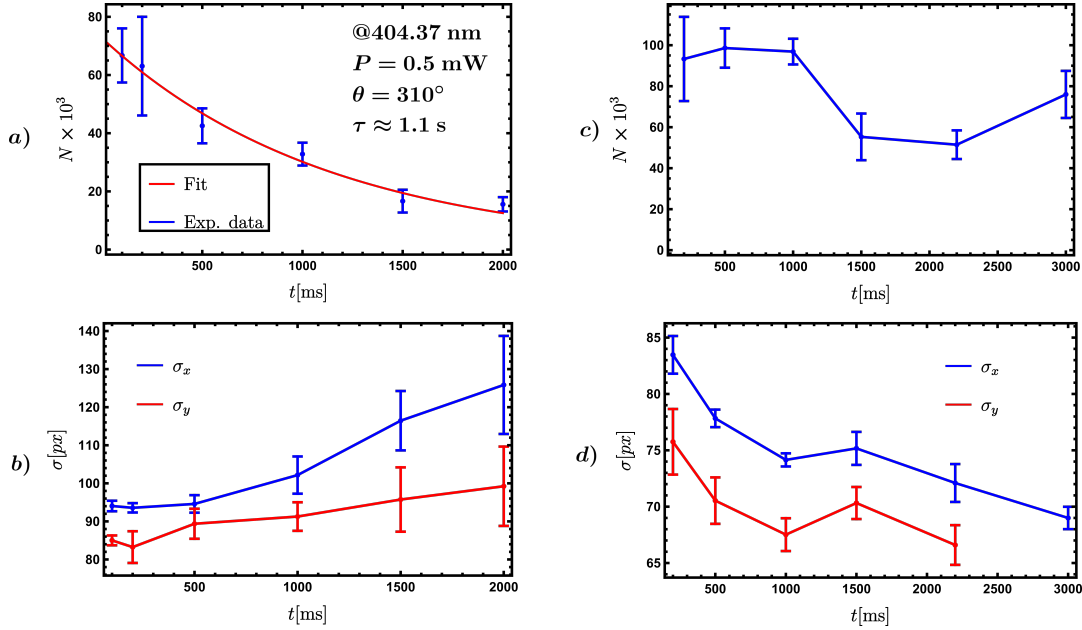


Figure 3.30: (a) Lifetime of the trapped thermal cloud as a function of the interaction time with the injection locked amplifier beam. (b) Size of the cloud as a function of the interaction time. A clear heating can be observed. (c) Lifetime of the trapped thermal cloud as a function of time. No interaction with the blue laser is present. (d) Size of the thermal cloud without interactions with the blue laser.

amplifier. After the filter the optical path divides in 2 branches thanks to a PBS, one of these branches goes to the Fabry-Pérot cavity. We use this cavity to monitor the single modedness of the amplifier laser, in a similar way to what we did in the other setups. If we see the single mode signal in the cavity transmission we can infer that the amplifier laser has been successfully injected by the master. The other branch of the optical setup first goes through an acousto optical modulator (A.O.M.) that we use to make short pulses of blue light (more than a factor of 10 shorter than the one we can produce with a fast shutter), and then the light gets coupled inside a single mode fiber, that has the output end in the same place shown in figure 3.18. Thanks to this we can use this setup, in the same way as we did with the one with just the master laser, to make measurements of the BEC's lifetime and polarizability. In figure 3.30 is reported the lifetime and the size of the thermal cloud as a function of the interaction time with the injection locked amplifier laser, compared to the ones without blue beam on. From the figure we can see a lifetime of the BEC of about 1.1 s, which is definitely enough to make measurements of the polarizability also with the injection locked laser. The scheme of the measurement is the same shown in figure 3.19. We make both measurements of the ratio between α_s and α_t by changing the orientation of the waveplate shown in figure 3.18, and also absolute measurements of the polarizability by measuring the displacement δ_x against the pulse time δt and by relating α with δt through the formula 3.7. In both cases the time of flight for the BEC is still $\tau_{t.o.f.} = 25$ ms. In figure 3.31 is shown the result for the measurement

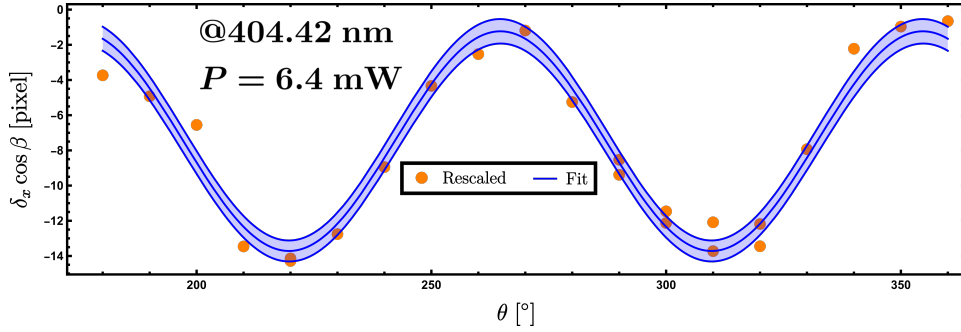


Figure 3.31: Displacement of the atomic center of mass $\delta_x \cos \beta$ along the horizontal direction of the imaging camera, as a function of the polarization angle θ expressed through the angle read on the half waveplate.

varying the angle made by the electric field polarization and the BEC magnetization. This measurement gives an estimate for the ratio between the scalar and tensor component for the polarizability equal to $\alpha_s/\alpha_t = -1.12 \pm 0.12$ that is in agreement with the theory for which, when $\lambda = 404.42$, we have $(\alpha_s/\alpha_t)_{theory} = -1.09$. In figure 3.32 it's instead shown the result for the displacement δ_x as a function of the interaction time with the blue laser δt . This time can be changed through the a.o.m. shown in figure 3.29 and this permits us to make much shorter pulses. Taking the slope of the line shown in the figure we get a value for the polarizability that is consistent with what we got with just the master laser.

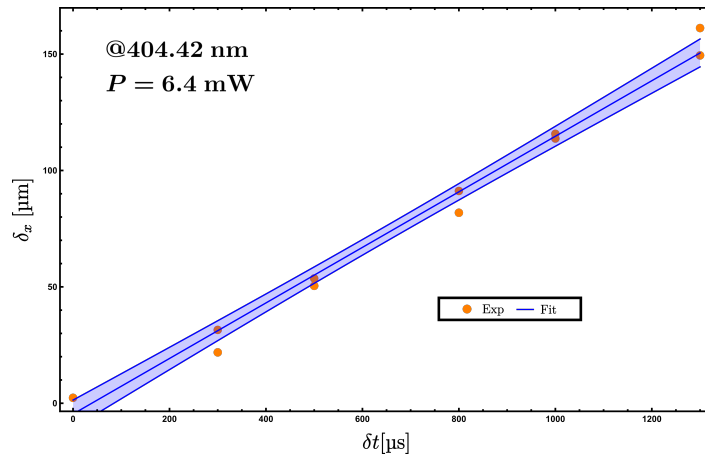


Figure 3.32: δ_x as a function of the interaction time δt with the blue laser. δt can be changed through the use of an A.O.M.

3.5 Calibration of the imaging magnification

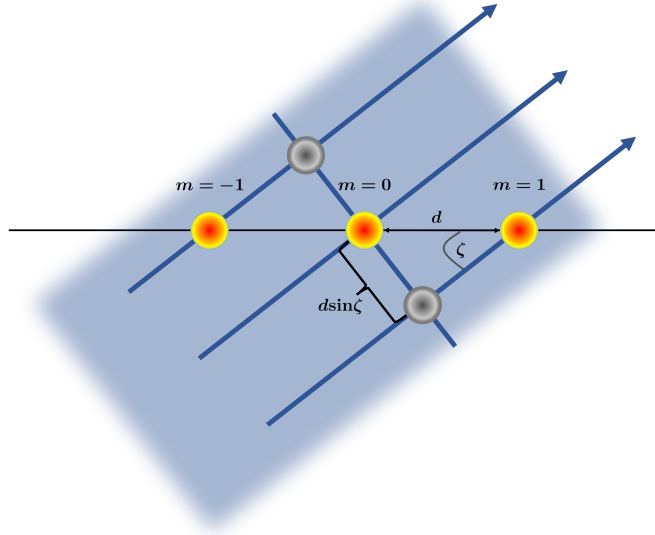


Figure 3.33: Sketch of the imaging beam used to define ζ . Since the imaging beam crosses the lattice at the angle ζ , the distances measured through this imaging will be less than the real ones by a factor of $\sin \zeta$.

The magnification of an optical system represents the ratio of lengths after and before the system. In formulas, if we define as L_i the length scale before the optical system and L_f the length scale after the system, the magnification \mathcal{M} of the optical system is defined by

$$\mathcal{M} = \frac{L_f}{L_i} . \quad (3.9)$$

The calibration of the magnification for both the “Vertical” and “Horizontal” imagings is done with the Raman-Nath (RN) scheme. Both these imaging are done with resonant light at 421 nm and, in particular, the setup of the horizontal one is the same that is shown in figure 3.18, where the horizontal imaging beam goes through the PBS and gets transmitted towards the science chamber. Thanks to this, through the calibration of the magnification for this imaging its also possible to obtain the magnification for the laser working at 404 nm.

In the RN scheme, a fast lattice pulse of non-resonant light hits the BEC. By calling with $\mathbf{k} = \hat{k}2\pi/\Lambda$ the wave vector of the laser used to make the lattice, this pulse brings some atoms from the $|\mathbf{p} = 0\rangle$ state to the $|\mathbf{p} = \pm 2\hbar\mathbf{k}\rangle$ states, and these states can be then coupled to higher momenta states, and this process lasts as long as the pulse is on. If, after the pulse, we let the BEC expand in time of flight, these diffraction peaks will fly at different distances given their different momentum.

In fact, one can calculate the distance \mathbf{r}_m traveled by an atom that was in the $\mathbf{p} = 2m\hbar\mathbf{k}$

state in a very simple way:

$$\mathbf{r}_m = \frac{2m\hbar\mathbf{k}}{M}\tau \quad (3.10)$$

where M represents the Dy's mass and τ is the time of flight.

This result implies that the distance between two adjacent peaks will be given by

$$d \equiv \|\mathbf{r}_{m+1} - \mathbf{r}_m\| = \frac{4\pi\hbar}{\Lambda M}\tau \quad (3.11)$$

and is independent of m .

By making an imaging after the expansion time has elapsed, its possible to measure the distance between the peaks in the imaging camera. Let's call this distance \tilde{d} . \tilde{d} will be related to the distance between the peaks in the atomic plane by the relation:

$$\tilde{d} = \mathcal{M}d \sin \zeta \quad (3.12)$$

where ζ is represented in figure 3.33 and is defined as the angle made by the lattice and the imaging beam. Combining equation 3.11 and 3.12 we get the following expression for the magnification of the imaging system

$$\mathcal{M} = \frac{\tilde{d}}{\sin \zeta} \frac{M\Lambda}{4\pi\hbar\tau} \quad (3.13)$$

and on the right hand side we are left with measurable quantities.

In figure 3.34 is shown the experimental result for one of the Raman Nath measurement. By making a fit on the intensity distribution of the form:

$$f_m(x; \tilde{d}, A_m, \sigma_m, n, \text{off}) = \sum_{m=-n}^n A_m \exp\left(-\frac{(x - m\tilde{d})^2}{2\sigma_m^2}\right) + \text{off} \quad (3.14)$$

where the sum runs on all the detected diffraction peaks, it is possible to extract \tilde{d} from the data. Of course, this \tilde{d} will be expressed in pixels of the camera but it's sufficient to multiply this number by the pixel size to get the correct value.

For the other parameters, since the lattice is created by the resonator placed in vacuum we have that $\Lambda = 1064$ nm whereas $\zeta = 52^\circ$ for the horizontal imaging.

The resulting magnification for the horizontal imaging is given by $\mathcal{M} = 0.761 \pm 0.006$. Thanks to this calibration is possible to obtain the spatial dimensions of the 404 nm beam in the atomic plane by just making an imaging of its radial profile with the camera shown in figure 3.18.

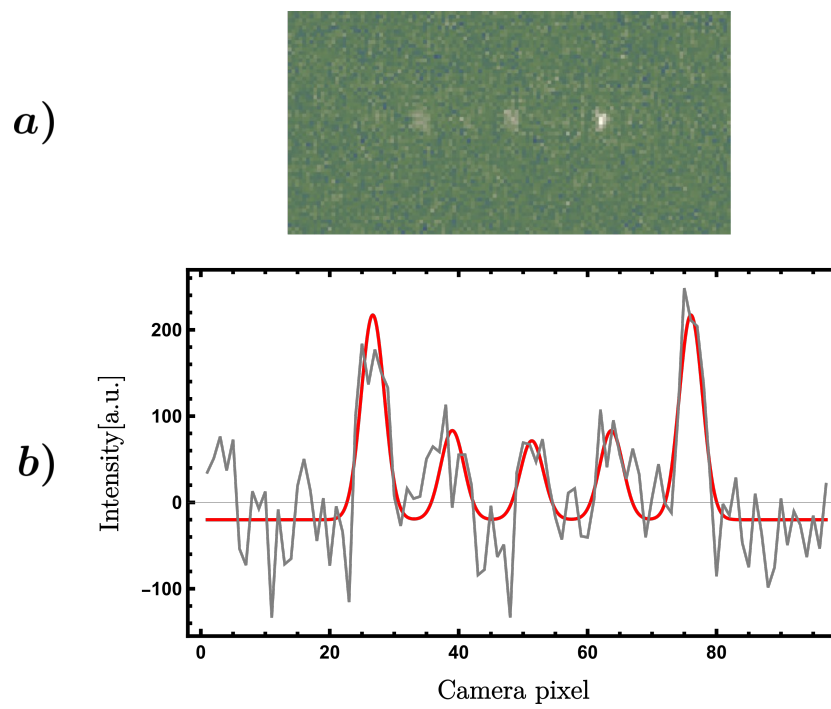


Figure 3.34: (a) Experimental shot for the Raman-Nath calibration. (b) Intensity distribution along the peaks and relative fit.

Conclusions

In this thesis I reported the work I did towards the realization of an annular potential where in the near future we will trap a dysprosium BEC. This potential will completely change the symmetry of our system and will allow us to address extremely interesting phenomena such as persistent currents, solitons, vortices and the non classical rotational properties of the supersolid.

My work has been concentrated initially on the realization of an optical setup where I could study and characterize the digital micromirror device that we will employ to realize the annular potential. I also realized a feedback program in Mathematica that works like a PI controller. This feedback program is able to remove the gaussian profile of the laser from the ring and make it homogeneous. By simulating the ground state both for the superfluid and the supersolid inside the experimentally achieved ring, it was possible to show that the potentials we are able to realize with the DMD are good enough to see the formation of the supersolid and the delocalization of the superfluid.

In the main part of my work I devoted my efforts into the realization of a laser source capable of outputting blue light at 404 nm. We want to use this laser to make our repulsive potential with the DMD and working at such low wavelength will be important for our experiment because it gives a better expected optical resolution for our potential, the diffraction limit for the resolution at this particular wavelength being 1.5 μm . Having an high enough resolution is extremely important in our case since we want to work with rings that have a radius of about 5 μm and a thickness around 2 μm . This thickness will then be on the order of the system's resolution. The blue laser I studied is a *Nichia NDV4313* diode laser that, out of the box, is multimode and thus has a broad spectrum of emission. Through measurements of this spectrum we noticed that some of the laser emission crossed with a dysprosium's strong absorption transition. This makes the atom's light scattering rate extremely high and because of this a lot of experimental effort was also put into reducing the broadness of the laser spectrum. This was achieved through an optical setup where a two stage light dispersion was employed, both stages realized through a diffraction grating. This optical configuration removes the problem of the broadness of the spectrum and we made sure of this by measuring the lifetime of our BEC as a function of the interaction time with the blue laser, both with and without the diffraction gratings. A definite improvement of the lifetime was seen in the second configuration, showing how we were really able to filter out the laser spectrum. However, this new setup brought forth the problem of laser power. In fact, the optical setup is extremely efficient in tightening the laser spectrum but at the cost of a big emission power loss. This loss could mean that when we will try to place the atoms under the ring trap, they will escape it because

the trap is too shallow. However, the trapping potential does not only depend on the laser power, but also on the atom's polarizability that, since we are working extremely close to resonance, should be really high. The loss in laser power could then be amply compensated by this polarizability. Since the polarizability of dysprosium at 404 μm is still not a tabulated quantity, we did a measurement of it ourselves. What we found is shown in figure 3.28, where our experimental findings are compared to our theoretical predictions for both the scalar and tensorial part of the polarizability. The theory stands above the experimental values by circa a factor of 3 over the whole range of wavelength that we investigated. This factor of three could come into play when we will try to trap the atoms inside the ring. This is because, if we use a waist for the blue beam that is around 30 μm and a laser power on the atomic plane of about 0.5 mW, then if the theoretical predictions are correct and the polarizability is around 10^4 au, the achievable potential depths will be around 500 nK. This is definitely more than the chemical potential of our system and enough to trap the atoms. However, if the experimentally determined values for the polarizability are actually correct, then the polarizability will be around 3×10^3 and the trapping depth becomes a factor of three less we might not be able to trap the atoms. Right now this disagreement between the experimental and theoretical values for the polarizabilities seems to come from a systematic error on the beam's waist measurement in the atomic plane that could come from an error on the calibration of the imaging's magnification. Future checks will be concentrated on this.

A low value of the polarizability can be compensated by increasing the laser power. To do this we also realized a master-amplifier configuration to work with a single mode laser but with higher power. We also employed this new setup to make measurements of the polarizability and found similar results to the one we found with just the master laser. Regarding the measurement of the polarizability, in the future when the DMD will be on the atoms we will be able to employ it to realize a trapping potential for the atoms made with our repulsive blue light. This will allow us to make measurements of the polarizability in the standard way employed for attractive potentials, that is, to measure dipole oscillations inside the trap. In this way we will be able to compare the result with the one we already got and see if they match.

The next steps we will make towards the trapping of our degenerate gas in the ring potential will be dynamical simulations to find the right potential to phase imprint angular momentum both to the superfluid and the supersolid, the experimental realization of a light sheet potential to trap the atoms in the vertical direction and sustain them against gravity and a new scheme for the imaging to implement the DMD on our system.

Bibliography

- [1] Mike H Anderson, Jason R Ensher, Michael R Matthews, Carl E Wieman, and Eric A Cornell. Observation of Bose-Einstein condensation in a dilute atomic vapor. *Science*, 269(5221):198–201, 1995.
- [2] Kendall B Davis, M-O Mewes, Michael R Andrews, Nicolaas J van Druten, Dallin S Durfee, DM Kurn, and Wolfgang Ketterle. Bose-Einstein condensation in a gas of sodium atoms. *Physical Review Letters*, 75(22):3969, 1995.
- [3] R Onofrio, C Raman, JM Vogels, JR Abo-Shaeer, AP Chikkatur, and W Ketterle. Observation of superfluid flow in a Bose-Einstein condensed gas. *Physical Review Letters*, 85(11):2228, 2000.
- [4] Kirk W Madison, Frédéric Chevy, Wendel Wohlleben, and Jean Dalibard. Vortex formation in a stirred Bose-Einstein condensate. *Physical Review Letters*, 84(5):806, 2000.
- [5] Martin W Zwierlein, Jamil R Abo-Shaeer, Andre Schirotzek, Christian H Schunck, and Wolfgang Ketterle. Vortices and superfluidity in a strongly interacting Fermi gas. *Nature*, 435(7045):1047–1051, 2005.
- [6] John F Allen and AD Misener. Flow of liquid helium II. *Nature*, 141(3558):75–75, 1938.
- [7] Pyotr Kapitza. Viscosity of liquid helium below the λ -point. *Nature*, 141(3558):74–74, 1938.
- [8] Eugene P Gross. Unified theory of interacting bosons. *Physical Review*, 106(1):161, 1957.
- [9] Anthony J Leggett. Can a solid be” superfluid”? *Physical Review Letters*, 25(22):1543, 1970.
- [10] AF Andreev and IM Lifshits. Quantum theory of defects in crystals. *Zhur Eksper Teoret Fiziki*, 56(6):2057–2068, 1969.
- [11] GV Chester. Speculations on Bose-Einstein condensation and quantum crystals. *Physical Review A*, 2(1):256, 1970.

-
- [12] Eunseong Kim and Moses Hung-Wai Chan. Probable observation of a supersolid helium phase. *Nature*, 427(6971):225–227, 2004.
- [13] Eunseong Kim and Moses HW Chan. Observation of superflow in solid helium. *Science*, 305(5692):1941–1944, 2004.
- [14] Sebastien Balibar. The enigma of supersolidity. *Nature*, 464(7286):176–182, 2010.
- [15] Duk Y Kim and Moses HW Chan. Absence of supersolidity in solid helium in porous vycor glass. *Physical Review Letters*, 109(15):155301, 2012.
- [16] Julian Léonard, Andrea Morales, Philip Zupancic, Tilman Esslinger, and Tobias Donner. Supersolid formation in a quantum gas breaking a continuous translational symmetry. *Nature*, 543(7643):87–90, 2017.
- [17] Lev Landau. Theory of the superfluidity of helium II. *Physical Review*, 60(4):356, 1941.
- [18] Luca Tanzi, Eleonora Lucioni, Francesca Famà, Jacopo Catani, Andrea Fioretti, Carlo Gabbanini, Russell N Bisset, Luis Santos, and Giovanni Modugno. Observation of a dipolar quantum gas with metastable supersolid properties. *Physical Review Letters*, 122(13):130405, 2019.
- [19] L Chomaz, D Petter, P Ilzhöfer, G Natale, A Trautmann, C Politi, G Durastante, RMW Van Bijnen, A Patscheider, M Sohmen, et al. Long-lived and transient supersolid behaviors in dipolar quantum gases. *Physical Review X*, 9(2):021012, 2019.
- [20] Fabian Böttcher, Jan-Niklas Schmidt, Matthias Wenzel, Jens Hertkorn, Mingyang Guo, Tim Langen, and Tilman Pfau. Transient supersolid properties in an array of dipolar quantum droplets. *Physical Review X*, 9(1):011051, 2019.
- [21] L Tanzi, SM Rocuzzo, E Lucioni, F Famà, A Fioretti, C Gabbanini, G Modugno, A Recati, and S Stringari. Supersolid symmetry breaking from compressional oscillations in a dipolar quantum gas. *Nature*, 574(7778):382–385, 2019.
- [22] L Tanzi, JG Maloberti, G Biagioni, A Fioretti, C Gabbanini, and G Modugno. Evidence of superfluidity in a dipolar supersolid from nonclassical rotational inertia. *Science*, 371(6534):1162–1165, 2021.
- [23] AS Arnold, CS Garvie, and E Riis. Large magnetic storage ring for Bose-Einstein condensates. *Physical Review A*, 73(4):041606, 2006.
- [24] S Gupta, KW Murch, KL Moore, TP Purdy, and DM Stamper-Kurn. Bose-Einstein condensation in a circular waveguide. *Physical Review Letters*, 95(14):143201, 2005.
- [25] Changhyun Ryu, MF Andersen, Pierre Clade, Vasant Natarajan, Kristian Helmerson, and William D Phillips. Observation of persistent flow of a Bose-Einstein condensate in a toroidal trap. *Physical Review Letters*, 99(26):260401, 2007.

- [26] Mathieu de Goër de Herve, Yanliang Guo, Camilla De Rossi, Avinash Kumar, Thomas Badr, Romain Dubessy, Laurent Longchambon, and Hélène Perrin. A versatile ring trap for quantum gases. *Journal of Physics B: Atomic, Molecular and Optical Physics*, 54(12):125302, 2021.
- [27] A Ramanathan, KC Wright, Sérgio Ricardo Muniz, Martin Zelan, WT Hill III, CJ Lobb, Kristian Helmerson, WD Phillips, and GK Campbell. Superflow in a toroidal Bose-Einstein condensate: an atom circuit with a tunable weak link. *Physical Review Letters*, 106(13):130401, 2011.
- [28] Kevin C Wright, RB Blakestad, Christopher J Lobb, William D Phillips, and Gretchen K Campbell. Driving phase slips in a superfluid atom circuit with a rotating weak link. *Physical Review Letters*, 110(2):025302, 2013.
- [29] Stuart Moulder, Scott Beattie, Robert P Smith, Naaman Tammuz, and Zoran Hadzibabic. Quantized supercurrent decay in an annular Bose-Einstein condensate. *Physical Review A*, 86(1):013629, 2012.
- [30] Scott Beattie, Stuart Moulder, Richard J Fletcher, and Zoran Hadzibabic. Persistent currents in spinor condensates. *Physical Review Letters*, 110(2):025301, 2013.
- [31] Yanping Cai, Daniel G Allman, Parth Sabharwal, and Kevin C Wright. Persistent currents in rings of ultracold fermionic atoms. *Physical Review Letters*, 128(15):150401, 2022.
- [32] Kevin Henderson, Changhyun Ryu, Calum MacCormick, and MG Boshier. Experimental demonstration of painting arbitrary and dynamic potentials for Bose-Einstein condensates. *New Journal of Physics*, 11(4):043030, 2009.
- [33] C Ryu, KC Henderson, and MG Boshier. Creation of matter wave besel beams and observation of quantized circulation in a Bose-Einstein condensate. *New Journal of Physics*, 16(1):013046, 2014.
- [34] G Del Pace, K Khani, A Muzi Falconi, M Fedrizzi, N Grani, D Hernandez Rajkov, M Inguscio, F Scazza, WJ Kwon, and G Roati. Imprinting persistent currents in tunable fermionic rings. *Physical Review X*, 12(4):041037, 2022.
- [35] Laura Corman, Lauriane Chomaz, Tom Bienaimé, Rémi Desbuquois, Christof Weitenberg, Sylvain Nascimbene, Jean Dalibard, and Jérôme Beugnon. Quench-induced supercurrents in an annular Bose gas. *Physical Review Letters*, 113(13):135302, 2014.
- [36] Avinash Kumar, Romain Dubessy, Thomas Badr, Camilla De Rossi, Mathieu de Goër de Herve, Laurent Longchambon, and Hélène Perrin. Producing superfluid circulation states using phase imprinting. *Physical Review A*, 97(4):043615, 2018.
- [37] Kali E Wilson, E Carlo Samson, Zachary L Newman, and Brian P Anderson. Generation of high-winding-number superfluid circulation in Bose-Einstein condensates. *Physical Review A*, 106(3):033319, 2022.

-
- [38] Thierry Lahaye, C Menotti, L Santos, M Lewenstein, and T Pfau. The physics of dipolar bosonic quantum gases. *Reports on Progress in Physics*, 72(12):126401, 2009.
- [39] Lev Pitaevskii and Sandro Stringari. *Bose-Einstein condensation and superfluidity*, volume 164. Oxford University Press, 2016.
- [40] Falk Wächtler and L Santos. Quantum filaments in dipolar Bose-Einstein condensates. *Physical Review A*, 93(6):061603, 2016.
- [41] Hitensinh Vaghela, Vikas J Lakhera, and Biswanath Sarkar. Forced flow cryogenic cooling in fusion devices: A review. *Heliyon*, 7(1):e06053, 2021.
- [42] Fritz London. The λ -phenomenon of liquid helium and the Bose-Einstein degeneracy. *Nature*, 141(3571):643–644, 1938.
- [43] DG Henshaw and ADB Woods. Modes of atomic motions in liquid helium by inelastic scattering of neutrons. *Physical Review*, 121(5):1266, 1961.
- [44] M Nilsson Tengstrand, David Bohlm, Rashi Sachdeva, Jakob Bengtsson, and SM Reimann. Persistent currents in toroidal dipolar supersolids. *Physical Review A*, 103(1):013313, 2021.
- [45] G Biagioni. Evidence of superfluidity in a dipolar supersolid. *Il nuovo cimento C*, 44(4-5):1–4, 2021.
- [46] James Roger Prior Angel and PGH Sandars. The hyperfine structure Stark effect i. Theory. *Proceedings of the Royal Society of London. Series A. Mathematical and Physical Sciences*, 305(1480):125–138, 1968.
- [47] Dmitriĭ Aleksandrovich Varshalovich, Anatolij Nikolaevič Moskalev, and Valerii Kel'manovich Khersonskii. *Quantum theory of angular momentum*. World Scientific, 1988.
- [48] Rudolf Grimm, Matthias Weidemüller, and Yurii B Ovchinnikov. Optical dipole traps for neutral atoms. In *Advances in atomic, molecular, and optical physics*, volume 42, pages 95–170. Elsevier, 2000.
- [49] Hui Li, Jean-Francois Wyart, Olivier Dulieu, Sylvain Nascimbene, and Maxence Lepers. Optical trapping of ultracold dysprosium atoms: transition probabilities, dynamic dipole polarizabilities and van der Waals c_6 coefficients. *Journal of Physics B: Atomic, Molecular and Optical Physics*, 50(1):014005, 2016.
- [50] Anthony E Siegman. *Lasers*. University science books, 1986.
- [51] Patricia Amara, D Hsu, and John E Straub. Global energy minimum searches using an approximate solution of the imaginary time Schrödinger equation. *The Journal of Physical Chemistry*, 97(25):6715–6721, 1993.

- [52] 2016 Documentation DLP6500 0.65 1080p MVSP Type A DMD. Texas Instruments. <https://www.ti.com/lit/ds/symlink/dlp6500flq.pdf?ts=1670626588572>, 2022.
- [53] Bahaa EA Saleh and Malvin Carl Teich. *Fundamentals of photonics*. John Wiley & Sons, 2019.
- [54] EA RW FLOYD. Adaptive algorithm for spatial gray scale. In *Proceedings of the ISDT*, 1985.
- [55] E Lucioni, L Tanzi, A Fregosi, J Catani, S Gozzini, M Inguscio, A Fioretti, C Gabbanini, and G Modugno. Dysprosium dipolar Bose-Einstein condensate with broad feshbach resonances. *Physical Review A*, 97(6):060701, 2018.
- [56] E Lucioni, G Masella, A Fregosi, C Gabbanini, S Gozzini, A Fioretti, L Del Bino, J Catani, G Modugno, and M Inguscio. A new setup for experiments with ultracold dysprosium atoms. *The European Physical Journal Special Topics*, 226:2775–2780, 2017.
- [57] Documentation Violet laser diode NDV4313. Nichia corporation. <https://www.alldatasheet.com/datasheet-pdf/pdf/240033/NICHIA/NDV4313.html>, 2022.
- [58] A. Kramida, Yu. Ralchenko, J. Reader, and NIST ASD Team. NIST Atomic Spectra Database (ver. 5.10), [Online]. Available: <https://physics.nist.gov/asd> [2023, April 13]. National Institute of Standards and Technology, Gaithersburg, MD., 2022.
- [59] C Ravensbergen, V Corre, E Soave, M Kreyer, S Tzanova, E Kirilov, and R Grimm. Accurate determination of the dynamical polarizability of dysprosium. *Physical Review Letters*, 120(22):223001, 2018.
- [60] Documentation SA200-3B Scanning Cavity. Thorlabs. <https://www.alldatasheet.com/datasheet-pdf/pdf/240033/NICHIA/NDV4313.html>, 2022.
- [61] Documentation Reflective Holographic Gratings. Thorlabs. https://www.thorlabs.us/newgrouppage9.cfm?objectgroup_id=25&pn=GH13-36U, 2022.
- [62] Marian Kreyer, Jeong Ho Han, Cornelis Ravensbergen, Vincent Corre, Elisa Soave, Emil Kirilov, and Rudolf Grimm. Measurement of the dynamic polarizability of Dy atoms near the 626-nm intercombination line. *Physical Review A*, 104(3):033106, 2021.
- [63] ME Wickliffe, James E Lawler, and Gillian Nave. Atomic transition probabilities for Dy I and Dy II. *Journal of Quantitative Spectroscopy and Radiative Transfer*, 66(4): 363–404, 2000.

- [64] Joseph Reader, Charles H Corliss, WL Wiese, and GA Martin. Wavelengths and transition probabilities for atoms and atomic ions: Part 1. Wavelengths, Part 2. Transition probabilities. *Wavelengths and transition probabilities for atoms and atomic ions: Part 1. Wavelengths*, 1980.
- [65] Ziting Chen, Bojeong Seo, Mingchen Huang, Mithilesh K Parit, Peng Chen, and Gyu-Boong Jo. Active control of a diode laser with injection locking. *arXiv preprint arXiv:2105.11285*, 2021.
- [66] AJ Leggett. On the superfluid fraction of an arbitrary many-body system at $T = 0$. *Journal of statistical physics*, 93:927–941, 1998.
- [67] Thomas Chalopin, Vasiliy Makhlov, Chayma Bouazza, Alexandre Evrard, Adam Barker, Maxence Lepers, Jean-François Wyart, Olivier Dulieu, Jean Dalibard, Raphael Lopes, et al. Anisotropic light shift and magic polarization of the intercombination line of dysprosium atoms in a far-detuned dipole trap. *Physical Review A*, 98(4): 040502, 2018.
- [68] Luigi Amico, Malcolm Boshier, Gerhard Birkl, Anna Minguzzi, Christian Miniatura, L-C Kwek, Davit Aghamalyan, Veronica Ahufinger, Dana Anderson, Natan Andrei, et al. Roadmap on Atomtronics: State of the art and perspective. *AVS Quantum Science*, 3(3):039201, 2021.
- [69] Luigi Amico, Dana Anderson, Malcolm Boshier, Jean-Philippe Brantut, Leong-Chuan Kwek, Anna Minguzzi, and Wolf von Klitzing. Colloquium: Atomtronic circuits: From many-body physics to quantum technologies. *Reviews of Modern Physics*, 94(4):041001, 2022.
- [70] Christopher J Pethick and Henrik Smith. *Bose–Einstein condensation in dilute gases*. Cambridge university press, 2008.
- [71] Massimo Inguscio and Leonardo Fallani. *Atomic physics: precise measurements and ultracold matter*. OUP Oxford, 2013.
- [72] Claude Cohen-Tannoudji et al. *Advances in atomic physics: an overview*. 2011.
- [73] Giulio Biagioni. *Evidence of superfluidity in a dipolar supersolid through non-classical rotational inertia*. Master Thesis. Università degli studi di Firenze, 2020.
- [74] Nicolò Antolini. *Towards strongly dipolar superfluids in two dimensions*. Master Thesis. Università degli studi di Firenze, 2020.
- [75] Giulia Del Pace. *Tailored optical potentials for experiments with atomic superfluids*. Master Thesis. Università degli studi di Firenze, 2018.
- [76] Elia Perego. *Generation of arbitrary optical potentials for atomic physics experiments using a digital micromirror device*. Master Thesis. Università degli studi di Firenze, 2015.

- [77] Giulia Del Pace. *Tunneling transport in strongly-interacting atomic Fermi gases*. Phd Thesis. Università degli studi di Firenze, 2021.

Ringraziamenti

Inizio col ringraziare il gruppo sperimentale che mi ha accolto durante questi mesi a Firenze e Pisa. Grazie a Carlo e Luca, che sono stati pazienti con me e mi hanno insegnato a gestire l'esperimento. Grazie a Giulio e Nicolò, sempre simpatici e preparati. Non potevo chiedere due dottorandi migliori con cui vivere questa esperienza. Grazie a Andrea, per avermi dato fiducia e coinvolto in numerose attività di divulgazione. Thank you Théo, for always encouraging me when I was staying late in the lab to work on my thesis and for showing me your passion for physics. Grazie a Giovanni. Tu e Marco siete stati i professori che mi hanno fatto appassionare alla fisica dei gas ultrafreddi. Grazie per avermi accolto in questo fantastico gruppo di ricerca e per avermi seguito con attenzione durante la tesi.

Grazie a tutti gli amici che hanno contribuito ad alleggerire lo stress durante questi anni. Grazie a Leonardo e Niccolò, amici di una vita con cui ho condiviso molto. Grazie al gruppo del polo: Jacopo, Lorenzo, Gabriele, Vezzi, Matilde, Costanza e Lino. Ci siamo fatti forza a vicenda durante tutto il periodo universitario.

Grazie alla mia famiglia. Grazie a mia mamma che ha sempre creduto in me e mi ha insegnato a prendere la vita con leggerezza e ridere di tutto. Grazie a mio babbo che mi ha trasmesso la passione con cui cura le piccole cose che gli stanno a cuore e l'importanza dell'amare il proprio lavoro. Grazie alle nonne: Margherita e Giovanna. Mi avete cresciuto e dato amore come ad un figlio e di questo ve ne sarò per sempre grato. Grazie a tutti i miei zii: Lorella, Francesca, Stefano, Alessandro, Paola, Silvia, Gianluca. Ciascuno di voi ha contribuito in modo suo alla mia formazione e mi ha lasciato più di quanto possiate immaginare. Grazie anche a tutti i miei cugini: Alessandro, Alessio, Erica, Sara, Rebecca, Chiara, Matteo. Con alcuni di voi siamo cresciuti insieme e abbiamo formato legami indissolubili. Le due cugine più grandi sono state grande fonte di ispirazione per la loro tenacia e determinazione. Spero di poter essere in futuro per Chiara e Matteo quello che voi due siete state per me.

Infine, grazie a Matilde. Nei momenti di difficoltà la tua spensieratezza e gioia di vivere sono stati per me importantissimi. In questi anni abbiamo consolidato un rapporto stupendo e se sono riuscito a raggiungere questo importante traguardo è anche merito tuo.